STM INVESTIGATIONS OF SELF-ASSEMBLED BISMUTH NANOSTRUCTURES AND ULTRA-FINE GOLD NANOPARTICLES

CHU XINJUN

NATIONAL UNIVERSITY OF SINGAPORE

2010

STM INVESTIGATIONS OF SELF-ASSEMBLED BISMUTH NANOSTRUCTURES AND ULTRA-FINE GOLD NANOPARTICLES

CHU XINJUN

(*M. Tech., Peking Univ. Tech.*)

A THESIS SUBMITTED

FOR THE DEGREE OF DOCTOR OF PHILOSOPHY

DEPARTMENT OF PHYSICS

NATIONAL UNIVERSITY OF SINGAPORE

(2010)

ACKNOWLEDGEMENTS

I would like to take this opportunity to acknowledge all the help, supports, discussions and encouragements I have received during my Ph. D project.

I sincerely thank my main supervisor, Associate Prof. Wang Xue-sen, for his invaluable guidance and generous support throughout my Ph. D study at NUS. Without Prof. Wang's wide knowledge, patient guidance, useful comments regarding the experiment results, considerate assistance and constant encouragement, this Ph. D project can not be finished. During these four years, I have benefited tremendously from Prof. Wang's wide understanding of physics, logical way of thinking, provident insights and education methods.

I am very grateful to my co-supervisor, Prof. Andrew Thye Shen Wee, for his generous support, invaluable discussion and comments. I am deeply impressed that despite his busy schedule, Prof. Wee always made time to join the discussion of our experiment results and give precious suggestions.

I am very grateful to Dr. Chen Wei, for the support on the LT-STM experiment. He often gave me great encouragement and considerate support personally. I also thank Dr. Gao Xingyu for the support on Synchrotron radiation experiment.

I would like to express my gratitude to Mr. Zhang Hongliang who introduced me to the surface science lab and taught me the experimental techniques involved in UHV-STM system. I also thank Dr. Sunil Singh Kushvaha, a good group colleague who has given me numerous advices on experimental details.

My sincere gratefulness is directed to my colleagues and postgraduates in our Lab, with whom, I have had the opportunity to work with, learn from, and be friends with. In particular, I thank Dr. Xie Xianning, Dr. Xu Hai, Dr. Huang Han, Dr. Chen Lan, Dr. Qi Dongchen, Mr. Chen Shi, Dr. Sun Jiatao, Ms. Huang Yuli, Mr. Wang Yuzhan, Mr. Yao Guanggeng, and Mr. Xu Wentao, Ms. Xie Lanfei. My sincere thanks to the entire staff of physics department who had offer me generous academic and administrative help.

I profoundly thank my parents, Ms. Lu Chuanying and Mr. Chu Jianxin, with deepest sense of gratitude. Their sacrifice in life, financial support, constant encouragements, and endless love bring me where I am today. Their selfless giving, understanding and sincere expectations always encouraged me thought out the whole project. I thank very much my lovely, thoughtful and smart wife Ms. Zhu Meihui who has been always supporting me and giving me strength to finish my thesis. I also thank my relatives who were also the source of endless inspiration and constant support during my Ph. D program.

Much appreciation also goes to my good friends coming from Shandong University who are now studying here. I am indebted to all my friends in China.

Due to limited space, I hereby express my deep appreciation to all the people that I do not mention who have contributed to the efforts that made it possible to complete this dissertation.

Last but not the least, I would like to thank National University of Singapore for providing financial support to my Ph. D research.

TABLE OF CONTSNTS

Summary

In-situ scanning tunneling microscopy (STM) has been utilized to investigate the growth of bismuth nanorods (single/multi- layer, straight/branched), ultra-thin Bi nanowires, Bi superstructures, and ultra-fine Au nanoparticles (NPs) on various substrates. When deposited on MoS_2(0001), before the height exceeds the critical thickness, Bi form Bi(110) nanobelts (nanoribbons). Straight Bi nanorods can be obtained at low Bi flux and deposition amount, while at high Bi flux, multi-layer branched nanostructures form. A structural transformation from Bi(110) to Bi(111) was observed when the Bi(110) film thickness exceeds 8-Bi(110) monolayer. Other measurements such as scanning electron microscopy (SEM) and low energy electron diffraction (LEED) were used to characterize the orientation distribution of Bi nanobelts. In addition, Bi nanostructures deposited on highly-oriented pyrolytic graphite (HOPG) were studied by low temperature scanning tunneling spectroscopy (LT-STS). Thickness dependent local density of states (LDOS) on Bi(110) layers with different thickness was observed, which may result from the structural relaxation and transformation from Black-P like Bi(110) to bulk-like one.

Using a molecular layer 3,4,5,10-perylene tetracarboxylic dianhydride (PTCDA) on MoS_2(0001) as a template, ultra-thin Bi nanowires can be synthesized. Bi first grow into NWs with single atomic layer thickness and aligned orientation and then develop into 4- or 6-layer Bi (110) NWs at larger deposition amounts. The NWs grow along three directions of the ordered molecular layer. Due to the side wall passivation

by PTCDA, the growth of width of NWs is greatly depressed and hence NWs with large length-to-width ratio (LWR) can be obtained.

Using LEED and STM, three structural phases were revealed when Bi deposited on Ru(0001), with Bi coverage ranged from sub-monolayer (ML) to a few ML. A loosely rectangular superlattice ($2 \times \sqrt{3}$) formed at the initial growth stage. After more Bi was deposited, a hexagonal ($\sqrt{7} \times \sqrt{7}$)R19.1° superlattice was observed. When Ru(0001) was saturated with this ($\sqrt{7} \times \sqrt{7}$)R19.1°-Bi, it acts as a buffer layer and the surface becomes rather inert. With additional Bi deposited, Bi(110) thin film is formed on this inert substrate.

Using PTCDA as a surfactant layer, size-tunable ultra-fine Au NPs can be synthesized on MoS_2. The PTCDA overlayer can greatly increase the nucleation density of Au NPs and prevent fine NPs from aggregating into larger particles. Molecular scale STM images show that Au atoms nucleate and grow into NPs underneath the PTCDA layer and lift the molecules to the top of the NPs. Moreover, by annealing the sample, PTCDA molecules can desorb from the MoS_2 surface first and then desorb from the top of Au NPs at a higher temperature. By controlling the deposition amount of Au, the size of Au NPs can be tuned. In addition, interaction of Au NPs with PTCDA was investigated *in-situ* by X-ray photoelectron spectroscopy (XPS), and charge transfer from Au NPs to PTCDA was observed, which indicates that these Au NPs may have new chemical properties.

List of Figures

List of Publications

1. S. S. K. X.-S. Wang, X.-J. Chu, H.-L Zhang, Z.-J. Yan, W.-D. Xiao, "Selective Self-Assembly of Semi-metal Straight and Branched Nanorods on Inert Substrates". **Oxford Handbook of Nanoscience and Nanotechnology.** Chap. 15, pp 572~597. (2010).
2. X.-J. Chu, S. S. Kushvaha, H.-L. Zhang, X.-S. Wang, "Deposition of Bismuth on MoS_2: Formation of Nanobelt and Ultrathin Film". (To be submitted)
3. X.-J. Chu, A. T. S. Wee, X.-S. Wang, "Size Tunable Au Nanoparticles on MoS_2". (To be submitted)
4. X.-J. Chu, W. Chen, A. T. S. Wee, X.-S. Wang, "Template Growth of Bismuth Nanowires with large Length to Width Ratio". (To be submitted)
5. X.-J. Chu, H. Huang, Y. Huang, W. Chen, A.T.S. Wee and X.-S. Wang, "STM and LEED Investigation of Structural Phases of Bi on Ru(0001) ". (To be submitted)
6. X.-J. Chu, J. Sun, L. Chen, Y. Feng, A. T. S. Wee, X.-S. Wang, "Thickness Dependent LDOS of Bi(110) 1-D Nanostructures". (In Preparation)
7. X.-J. Chu, A. T. S. Wee, X.-S. Wang, "LT-STS Investigation of Charge Transfer of Bi(110) Film on Epitaxial Graphene on Ru(0001) ". (In Preparation)

Chapter 1 Introduction

Since December 29, 1959 when Richard Feynman gave a talk named "There's Plenty of Room at the Bottom" at an American Physical Society meeting at Caltech, the concept of "nanotechnology" has been immersed into academic and industry worldwide greatly. Potential applications of nanotechnology were indicated in the US President Clinton's speech at California Institute of Technology on January 21, 2000: "… shrinking all the information housed at the Library of Congress into a device the size of a sugar cube … detecting cancerous tumors when they are only a few cells in size." [1] Nanotechnology and nanoscience got another jump-start in the early 1980s with two major developments: the birth of cluster science and the invention of the scanning tunneling microscope (STM). In the 21st century, nanotechnology has been showing significant potential to create many new materials and devices with wide-range applications, such as in medicine, electronics, energy production, environmental sensors and so on.

In nanoscience and nanotechnology, nanostructural materials refer to the ones with sizes ranging from 1 nm to 100 nm in at least one dimension, including clusters, nano-crystallites, nanotubes, nanorods, nanowires and ultra-thin films. Due to the electrons being confined in nano-scale dimension(s), nanomaterials are unique as compared with both individual atoms/molecules at a smaller scale and the macroscopic bulk materials. This has considerable practical interest because the relative importance in bulk materials may increase dramatically for the much smaller

structures.

The following sub-sections provide an overview of motivation and synopsis of this PHD project, and a general introduction of surfaces/interfaces, thin film growth and self-assembly in nanoscience.

1.1 Motivation and Synopsis

Bismuth (Bi) is a typical group-V element which has attracted much attention due to its unique electronic properties [2-9]. A fascinating aspect is the study of its surfaces on which their properties can be radically different from those of the bulk. This is particularly relevant for nano-technology. On one hand, investigating the nanostructures of Bi can extend the understanding of self-assembly behavior and help to improve the synthesis method. Moreover, new approaches for fabrication and synthesis of nanostructural one-dimensional (1-D) bismuth wire are strongly demanded in the development of functional nanodevices. In addition, Bi deposited on some rare metal substrate (such as Ru) can extend the understanding of hetero-epitaxial behavior of Bi and help to understand the surface interaction which may not occur for bulk materials. On the other hand, the study of the electronic structures of self-assembled Bi nanostructures by scanning tunneling spectroscopy (STS) can extend the understanding of the unique physical properties of Bi and may promote new applications in spintronics.

As for the gold (Au), a rather inert noble metal in bulk form, Au nanoparticles

(NPs) with ultra small size to obtain a chemical catalysis effect is strongly needed in the development of environmental technology. The investigation also can establish a new way to synthesize size-tunable Au NPs in ultra-high vacuum (UHV) condition which is contamination free. Moreover, these NPs may show potential in the applications in nonlinear optics, biosynthesis, sensors, and in special, catalysis of CO and H_2 oxidation, NO reduction and CO_2 hydrogenation [10].

Based on the above motivations, this thesis will address the following issues:

(a) In ***Chapter 3***, I present the results of our *in situ* STM study of the growth and morphologies of Bi nanobelts (nanoribbons) and thin films on MoS_2(0001) and STS study of electronic structures of Bi nanobelts on HOPG. Other measurements such as scanning electron microscopy (SEM) and low-energy electron diffraction (LEED) were also used to characterize these Bi nanostructures. Our STM images show that Bi(110) nanobelts formed at lower deposition amount before the islands thickness reaches 8 Bi(110)-monolayer (ML). A structural transformation from Bi(110) to Bi(111) was observed when the Bi(110) film thickness exceeds 8 ML. The growth mechanism and the morphology characteristics of Bi nanostructures on MoS_2(0001) will be discussed in detail. LT-STS reveals the electronic properties of the Bi(110) nano-ribbons altered from a semiconducting feature at the thickness of 2- and 4-ML to a metallic one on the thickness larger than 6-ML. A qualitative explanation for the alternations of STS curves is proposed.

(b) In ***Chapter 4***, I demonstrate a new method of growing Bi nanowires (NWs) using a molecular layer 3,4,5,10-perylene tetracarboxylic dianhydride (PTCDA) on MoS_2(0001) as a template. *In-situ* STM images show that Bi first grows into ultra-thin NWs with single atomic layer thickness and aligned orientation. With more Bi deposited, the ultra-thin NWs develop into NWs in Bi(110) orientation with 4- or 6-ML thickness. The NWs grow along three directions of the ordered molecular layer. Due to the side wall passivation by PTCDA, the growth of width of NWs is greatly depressed and hence NWs with large length to width ratio can be obtained. A detailed growth schematic diagram will be proposed.

(c) In ***Chapter 5***, I present three structural phases after Bi deposition on Ru(0001) with Bi coverage ranged from sub-ML to a few ML. A loosely rectangular superlattice was observed when small amount of Bi was deposited. With LEED, three equivalent domains which rotated 120° from one another were observed and the period of the superlattice can be assigned as $2 \times \sqrt{3}$ corresponding to Ru(0001). After more Bi was deposited, a more compact superlattice was observed. LEED pattern reveals that this is a hexagonal $(\sqrt{7} \times \sqrt{7})R19.1°$ superlattice corresponding to Ru(0001). STM images show that every unit cell includes 4 atoms. When Ru(0001) was saturated with this $(\sqrt{7} \times \sqrt{7})R19.1°$-Bi, it acts as a buffer layer and the surface becomes rather inert. With additional Bi deposited, Bi(110) thin film is formed on this inert substrate. Schematics of unit cells for these three kinds of Bi structures will be elucidated in detail.

(d) In ***Chapter 6***, I show the synthesis of size-tunable ultrafine Au nanoparticles (NPs) in UHV condition by using a PTCDA layer on MoS_2(0001). The pre-deposited PTCDA overlayer can greatly increase the nucleation density of Au NPs and prevent the NPs from aggregating into larger particles. Molecular scale images show that Au atoms nucleate and grow into NPs underneath the PTCDA layer and lift the molecules to the top of the NPs. By heating the sample to certain temperature, it was found that the molecules desorbed first from the MoS_2 substrate and then from the Au NPs at higher temperature. Before the substrate is saturated with large Au NPs, the size of NPs can be simply tuned by the Au deposition time. The morphology evolution of the NPs and possible growth model is elucidated.

1.2 Surface and Interfaces

A surface is the shell of a macroscopic object (the inside) in contact with its environment (the outside world). An interface is the boundary between two phases. In large objects with small surface area to volume ratio (*A/V*), the physical and chemical properties are primarily defined by the bulk (inside). However, in small objects with a large *A/V*-ratio, the properties are strongly influenced by the surface. On a crystal surface, atoms feel an environment quite different than that in the bulk.

Surfaces can be considered as a special type of defect since the crystal order is interrupted at the surface. Surface/interface has many common properties of defects, such as generating additional electronic states, inducing stress, scattering carriers, and

as fast channels of atomic migration. But surface/interface is a much more important entity than just as a type of defect. Many important processes, including crystal growth, reaction and etching occur at the surface/interface. Surface, interface and junction structures possess certain novel characteristics which are not available from the bulk crystal. Some chemical reactions take place on the surfaces of some materials much more easily than at other places, which make surface an important subject for catalysis study and applications [11].

Most of semiconductors are classified as the covalent-bond materials (some are weakly ionic-bonded). There is a high density of dangling bonds (which are basically unpaired electrons) on a bulk-terminated semiconductor surface. The electronic states associated with the dangling bonds have relatively high energy. Reduction of dangling bonds can significantly decrease surface energy, and it is the main driving force for surface reconstruction on semiconductor surfaces. For example, on Si(001) surface, the dangling bond density is reduced by 50% in the dimerization process [12].

A real surface also has various imperfections itself. It is impossible to cut a crystal along one atomic plane, so atomic steps on surface are inevitable. Atomic steps also cannot be perfectly straight, i.e., there are kinks along steps. On the terraces, vacancies and adatoms are frequently observed. Steps, kinks, vacancies and adatoms are essential that must be considered in modeling a real surface, as shown in Fig. 1.1 [13]. They are important also because of their critical roles in surface processes, such as in film growth and chemical reaction. In addition, existence of

impurities on surfaces is rather common, and it affects the surface properties in various ways. For compound or alloy materials, the stoichiometry at surfaces may be different than that in bulk.

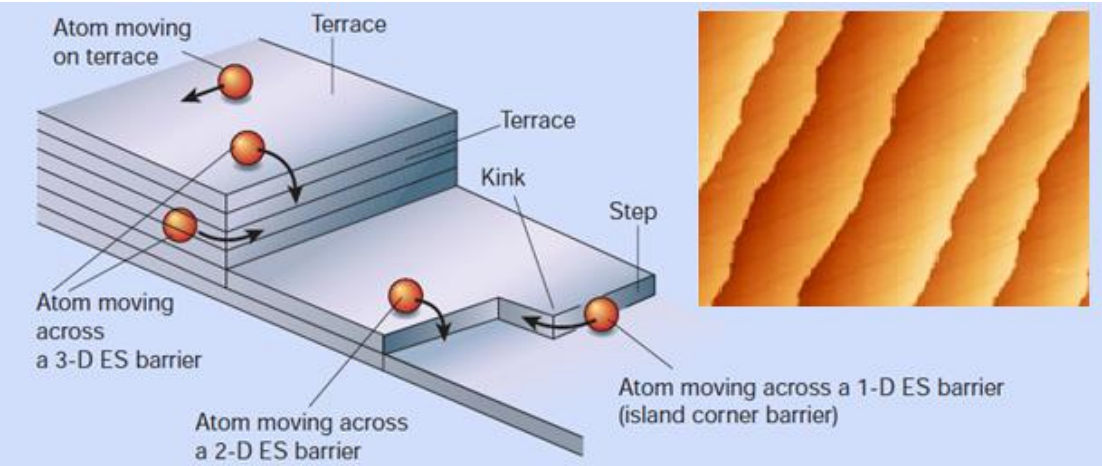

Fig. 1.1 The terrace-step-kink (TSK) model of a surface (reprinted from Ref. [13] by permission of the Nature Publishing Group). The surface consists of terraces separated by steps; a kink is a step on a step. The inset image shows the surface of a thin film of silicon (400 nm × 320 nm). Terraces separated by single-atom high steps with many kinks can be seen.

1.3 Overview of Thin Film Growth

The growth of nanostructures is a complex process including thermodynamic and kinetic factor. From the view of thermodynamics, the growth of nanostructures depends on the surface energy of deposited material, γ_A, the substrate surface energy, γ_B, and the interface energy, γ^*. Normally, the thin film growth can be divided into three modes: layer-by-layer growth (Frank-van der Merwe mode), layer-by-layer growth then islanding growth (Stranski-Krastanov mode) and islanding growth (3-D mode or Volmer-Weber mode) [14]. Fig. 1.2 (a), (b) and (c) illustrate the three growth modes, respectively. When $\gamma_A + \gamma^* < \gamma_B$, the nanostructure takes the layer-by-layer growth mode. When $\gamma_A + \gamma^* > \gamma_B$, the nanostructure favors 3-D islanding growth mode. When there is interface stress between the deposited material and the substrate, with the increasing thickness of the material, the interface energy γ^* may increase. After a critical thickness by layer-by-layer growth, further deposited material takes the islanding growth mode. Generally, the hetero-epitaxial growth of metal on semiconductor surface favors this growth mode, i.e. Stranski-Krastanov mode.

In the material growth process, however, due to the different depositing flux and diffusion speed (or growth temperature), the thin-film growth normally is not under thermodynamic equilibrium. Thus, one needs to consider the micro-kinetic conditions on the surface, including the adsorption, diffusing, desorption, coarsening, nucleation of atoms as well as the inter-layer migration of the atoms, shown in Fig. 1.3 (a) [15].

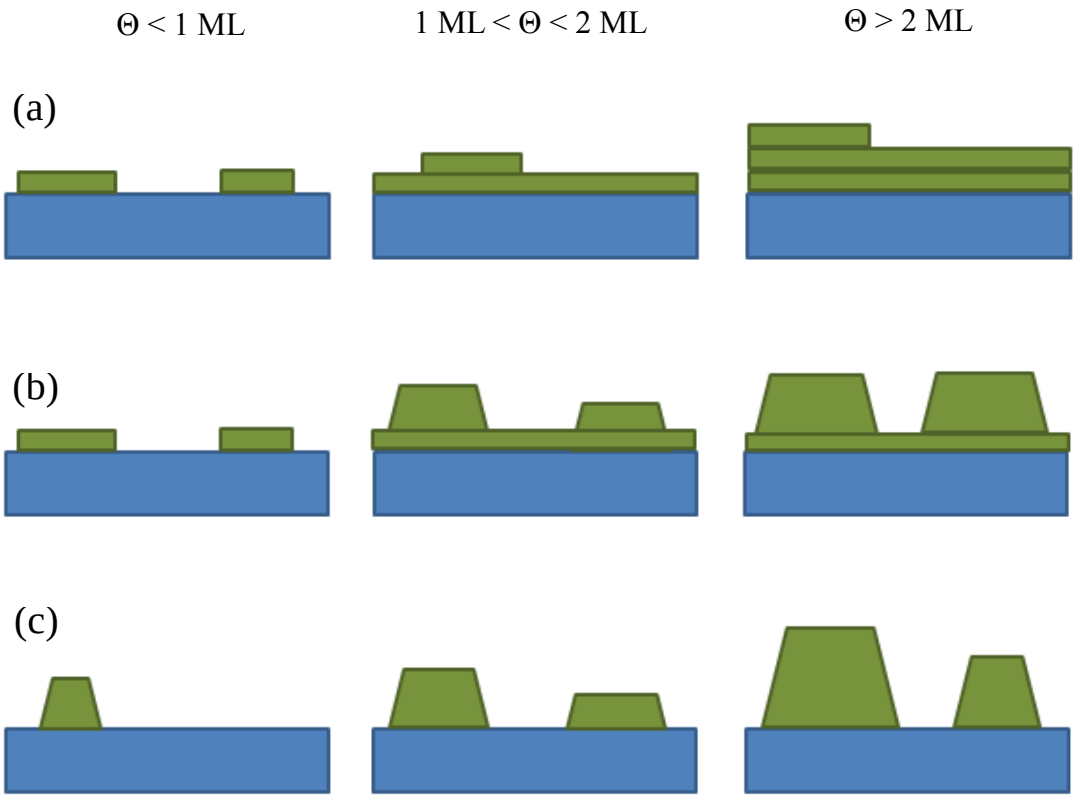

Fig. 1.2 Growth modes of nanostructures under thermodynamic equilibrium condition: (a) layer-by-layer growth (Frank-van der Merwe mode), (b) layer-by-layer growth then islanding growth (Stranski-Krastanov mode), and (c) islanding growth (3-D mode or Volmer-Weber mode). The coverage is represented by Θ.

The former factors can affect the lateral uniformity of the film, while the latter factor can lead to the 2-D or 3-D growth mode. If the material favors 2-D layer-by-layer growth mode, sufficient inter-layer atomic transport is necessary. An important concept in this process is Ehrlich-Schwoebel barrier (ES) as shown in Fig. 1.3 (b), which indicates the additional barrier for an adatom jumping down a step edge due to less neighbors than at a regular terrace site. If the ES barrier is large, it is hard for atoms to transport between layers. This will result to the 3-D growth. On the other hand, if the ES barrier is small, it is easy for atoms to perform the atomic inter-layer-transport. So, it will result to the 2-D growth. The three kinetic growth modes are shown in Fig. 1.3 (c). They are: step-flow growth, layer-by-layer growth, and multilayer growth.

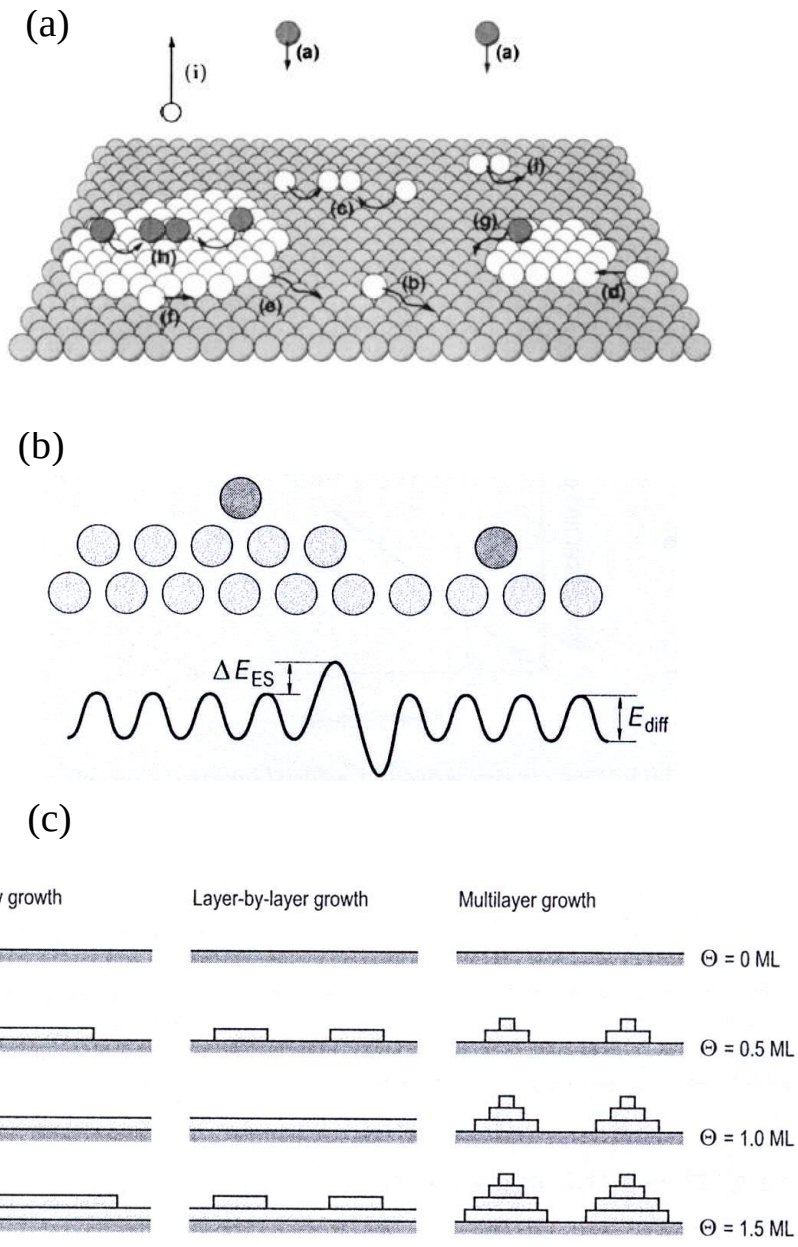

Fig. 1.3 (a) Typical atomic processes during epitaxial growth (reprinted from Ref. [15] by permission of the American Vacuum Society). For the process details (a)~(i), please refer to Ref. [15]. (b) Schematic drawing of ES barrier. (c) Three kinds of kinetic growth mode.

1.4 Self-Assembly

There are a variety of approaches to fabricate nanostructured materials in controlled ways, such as lithography, molecular beam epitaxy (MBE), self-assembly. Recently, self-assembly as a bottom-up method has attracted significant attention for its advantages of yielding nanostructures down to atomic scale and the potential for inexpensive mass fabrication [16]. Taking advantage of some energetic, kinetic and geometric effects in the material growth processes, self-assemble nanostructures can be formed themselves without external direction or management. The building blocks are not only atoms and molecules, but span a quite wide range of nano- and mesoscopic structures, with different chemical compositions, functionality and shapes. These nanoscale building blocks can in turn be synthesized through conventional chemical routes or by other self-assembly strategies. Since many nanostructures are formed simultaneously across the specimen in parallel, self- assemble processes are much favored in industrial nanofabrication.

In a self-assembly process, the weak interactions, e.g. Van der Waals, π-π, and hydrogen bonds, play an important role in materials synthesis. Although typically these weak interactions are less energetic by a factor 10 with respect to the more "traditional" covalent, ionic or metallic bonds, they are considered key to the inter-building-block structures and hence the morphology of self-assemble nanostructures. In addition, the key issues for the applications of self-assembly are the effective controls of size, shape and positioning (ordering) of the nanostructures fabricated.

Such controls can be achieved to certain degrees by properly selecting process condition and taking advantage of some intrinsic material properties.

One greatly investigated self-assembly method is to take advantage of the Stranski-Krastanov growth mode to fabricate semiconductor quantum dots (QD). It works well for heteroepitaxy with a certain amount of lattice mismatch, such as Ge on Si (4% mismatch) [17] and InAs on GaAs (7% mismatch). By taking advantage of kinetic instability, people can develop nanostructural patterns with pre-existing components or templates. A vicinal surface, i.e., a surface tilted away from a low-index plane by a few degrees, is a natural template for nano-structural assembly. Because the step edges are normally the preferential sites for nucleation and growth, self-organized 1-D nano-wires (NWs) can be formed along the steps within a relatively large area. A good example is the self-assembled Pb chains on Si(557) surface, investigated by Tegenkamp *et al.*[18].

Using surfaces reconstruction superlattices to act as templates, ordered nanostructures (e.g., QDs and NWs) can be fabricated. This nano-fabrication scheme has been demonstrated successfully in growing self-organized Co islands on Au(111) [19], arrays of identical metal clusters on Si(111) [20-22], arrays of metal nanowires on Si(001) [23], arrays of identical Al clusters formed on Si(111)-7×7 surface [22], and Ga nanowires formed on Si(100)-2×*n* [24].

Moreover, molecular self-assembly on surfaces or surface-supported nanotemplates via selective and directional covalent or non-covalent interactions offers a promising bottom-up approach to fabricating molecular nanostructure arrays

with desired functionalities over macroscopic areas. By steering the formation of ordered supermolecular assemblies with good structural stability, people can design and construct a wide range of 2D molecular nanostructures such as molecular supergratings and porous networks [25, 26].

In addition, there are many chemical self-assembly processes for fabricating a variety of nanomaterials and nanopatterns. For example, taking advantage of high affinity of thiols to the surface of noble metals, self-assembled monolayers (SAMs) of thiolates can be formed on noble metals. The SAMs not only are a type of nanostructures themselves in forms of nanopatterns, but also can act as surfactants for other nanostructures, especially for the fabrication of metal/molecules/metal devices. A good example is using thiolterthiophene molecules inserted into an alkylthiol matrix, forming a bundle at the location of the more conductive thiolthiophene molecules [27].

Reference

[1] J. Zhang, Z. L. Wang, J. Liu, S. Chen, and G. Y. Liu, "Self-Assembled Nanostructures" in Nanostructure Science and Technology, D. J. Lockwood, Ed. New York: Kluwer Academic/Plenum Publishers, 2003, pp. 1.

[2] Y.F. Xu, H.J. Zhang, Y.H. Lu, B. Song, Q. Chen, H.Y. Li, S.N. Bao, and P. He, Surf. Sci. **600**, 2002 (2006).

[3] C. R. Ast and H. Höchst, Phys. Rev. Lett. **87**, 177602 (2001).

[4] T. Hirahara, T. Nagao, I. Matsuda, G. Bihlmayer, E. V. Chulkov, Y. M. Koroteev, P. M. Echenique, M. Saito, and S. Hasegawa, Phys. Rev. Lett. **97**, 146803 (2006).

[5] C. A. Hoffman, J. R. Meyer, F. J. Bartoli, A. Divenere, X. J. Yi, C. L. Hou, H. C. Wang, J. B. Ketterson, and G. K. Wong, Phys. Rev. B **48**, 11431 (1993).

[6] Z. B. Zhang, X. Z. Sun, M. S. Dresselhaus, J. Y. Ying, and J. Heremans, Phys. Rev. B **61**, 4850 (2000).

[7] T. E. Huber, A. Nikolaeva, D. Gitsu, L. Konopko, C. A. Foss, and M. J. Graf, Appl. Phys. Lett. **84**, 1326 (2004).

[8] S. L. Cho, Y. Kim, A. J. Freeman, G. K. L. Wong, J. B. Ketterson, L. J. Olafsen, I. Vurgaftman, J. R. Meyer, and C. A. Hoffman, Appl. Phys. Lett. **79**, 3651 (2001).

[9] Y. M. Lin, X. Z. Sun, and M. S. Dresselhaus, Phys. Rev. B **62**, 4610 (2000).

[10] M.-C. Daniel and D. Astruc, Chem. Rev. **104**, 293 (2004).

[11] R. Blume, M. Hävecker, S. Zafeiratos, D. Teschner, E. Kleimenov, A. Knop-Gericke, R. Schlögl, A. Barinov, P. Dudin and M. Kiskinova, J. of Catalysis **239**,

354 (2006).

[12] Z. Zhang, F. Wu and M.G. Lagally, Annu. Rev. Mater. Sci. **27**, 525 (1997).

[13] M.G. Lagally and Z. Zhang, Nature **417**, 907 (2002).

[14] J. A. Venables, G. D. T. Spiller, and M. Hanbücken, Rep. Prog. Phys. **47**, (1984) 399.

[15] C. Ratsch and J. A. Venables, J. Vac. Sci. Technol. A **21**, S96 (2003).

[16] M. Brust and C. Kiely, Colloids and Surfaces A: Physicochemical and Engineering Aspects **202**, 175 (2002).

[17] R.S. Williams, G. Medeiros-Ribeiro, T.I. Kamins, and D.A.A. Ohlberg, J. Phys. Chem. B **102**, 9605 (1998).

[18] C. Tegenkamp, T. Ohta, J. L. McChesney, H. Dil, E. Rotenberg, H. Pfnür, and K. Horn, Phys. Rev. Lett. **100**, 076802 (2008).

[19] O. Fruchart, M. Klaua, J. Barthel, and J. Kirschner, Phys. Rev. Lett. **83**, 2769 (1999).

[20] M.Y. Lai, Y.L. Wang, Phys. Rev. B **64**, 241404 (2002).

[21] J.-L. Li *et al.*, Phys. Rev. Lett. **88**, 06610 (2002).

[22] J.-F. Jia, X. Liu,1 J.-Z. Wang, J.-L. Li, X. S. Wang, Q.-K. Xue, Z.-Q. Li, Z. Zhang, and S. B. Zhang, Phys. Rev. B **66**, 165412 (2002).

[23] J.-L. Li, X.-J. Liang, J.-F. Jia, X. Liu, J.-Z. Wang, E.-G. Wang, and Q.-K. Xue, Appl. Phys. Lett. **79**, 2826 (2001).

[24] J.-Z. Wang, J.-F. Jia, X. Liu, W.-D. Chen, Q.-K. Xue, Phys. Rev. B **65**, 235303 (2002).

[25] Y. Huang, W. Chen, H. Li, J. Ma, J. Pflaum, and A. T. S. Wee, Small **6**, 70 (2010).

[26] J. A. Theobald, N. S. Oxtoby, M. A. Phillips, N. R. Champness, and P. H. Beton, Nature **424**, 1029 (2003)

[27] D.Vuillaume, and S. Lenfant, Microelectronic Engineering **70**, 539 (2003).

Chapter 2 Experimental Facilities and Procedures

This chapter gives an overview of the main surface analysis techniques used in the projects of this thesis, including the basic theory and operation procedures. The substrate preparation, material growth methods and conditions are also included.

2.1 Surface Analysis Techniques

There are many surface analysis techniques, including scanning probing microscopy (SPM), LEED, Auger electron spectroscopy (AES), photoemission spectroscopy (PES), etc. In this section, only the techniques used in our experiments are introduced. They are: STM/STS, LEED, AES, and PES.

2.1.1 STM and STS

2.1.1.1 One-dimensional Tunneling Theory

In classical physics, an electron cannot exist where the potential energy V is larger than the total electron energy E, i.e., those regions are forbidden to the electron. However, quantum mechanics gives a quite different description, in which the wave function of the electron in the classical "forbidden region" may be non-zero. This means that an impinging electron has some probability to pass through a potential barrier, which is also called tunneling.

For a rectangular barrier of height $V_0 > E$ and width a shown in Fig. 2.1, define:

$$k_1 = \sqrt{2mE}/\hbar, \quad \text{and} \quad k_2 = \sqrt{2m(V_0 - E)}/\hbar \tag{2.1}$$

where m is mass of electron and $\hbar$ is the reduced Planck constant. As shown in Fig. 2.1, $A\exp(ik_1x)$ is the wave function of impinging electron. After encounter with the potential barrier, the particle will either be reflected (represented by $B\exp(-ik_1x)$) or tunnel through the barrier (represented by $C\exp(ik_2x)$). The probability of tunneling is [1]:

$$T = \left|\frac{C}{A}\right|^2 = \frac{4k_1^2k_2^2}{(k_1^2 + k_2^2)^2 \sinh^2(k_2a) + 4k_1^2k_2^2} \tag{2.2}$$

When the barrier is quite high and thick, so that $k_2a >> 1$, Eq. (2.2) can be simplified as [1]:

$$T \approx \frac{16k_1^2k_2^2}{(k_1^2 + k_2^2)^2}\exp(-2k_2a) = \frac{16E(V_0 - E)}{V_0^2}\exp\left[-\frac{2a}{\hbar}\sqrt{2m(V_0 - E)}\right] \tag{2.3}$$

In the case of STM, if we consider the sample-tip distance as Z, the wave function of the tunneling electron on the tip or surface can be written as:

$$\Psi \propto \exp(-k_2Z) \tag{2.4}$$

Eq. (2.4) shows that the wave function of the electron decay exponentially into the vacuum region from the tip or sample surface.

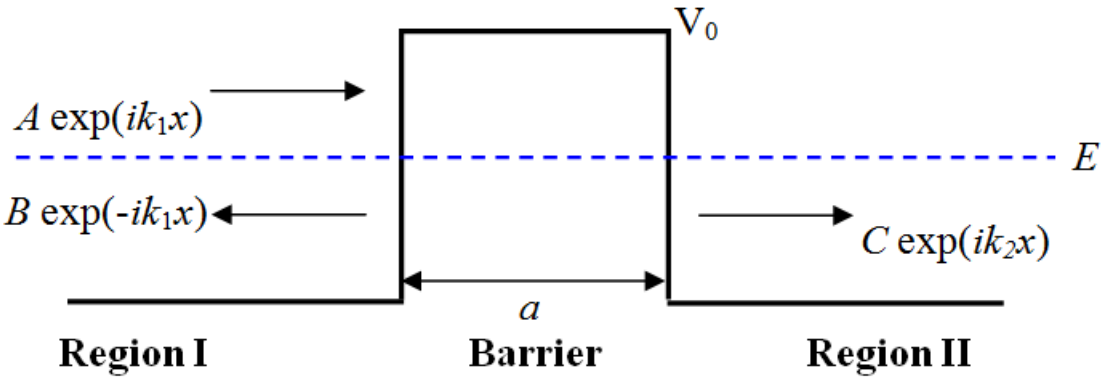

Fig. 2.1 A schematic drawing of an electron being reflected by or tunneling through a barrier. $A\exp(ik_1x)$ is the wave function of impinging electron. The reflection and tunneling part is represented by $B\exp(-ik_1x)$ and $C\exp(ik_2x)$, respectively.

2.1.1.2 Basic Working Principles of STM

As shown in Fig. 2.2, a STM is basically comprised of an atomic sharp metallic tip mounted on a piezoelectric tube scanner with electrodes, voltage control circuit, feedback control circuit, signal amplifier, data processing and display terminal and a sample. In a STM, the tip and sample are two electrodes. If the separation between the tip and sample is small enough, there will be a tunneling current between the two electrodes.

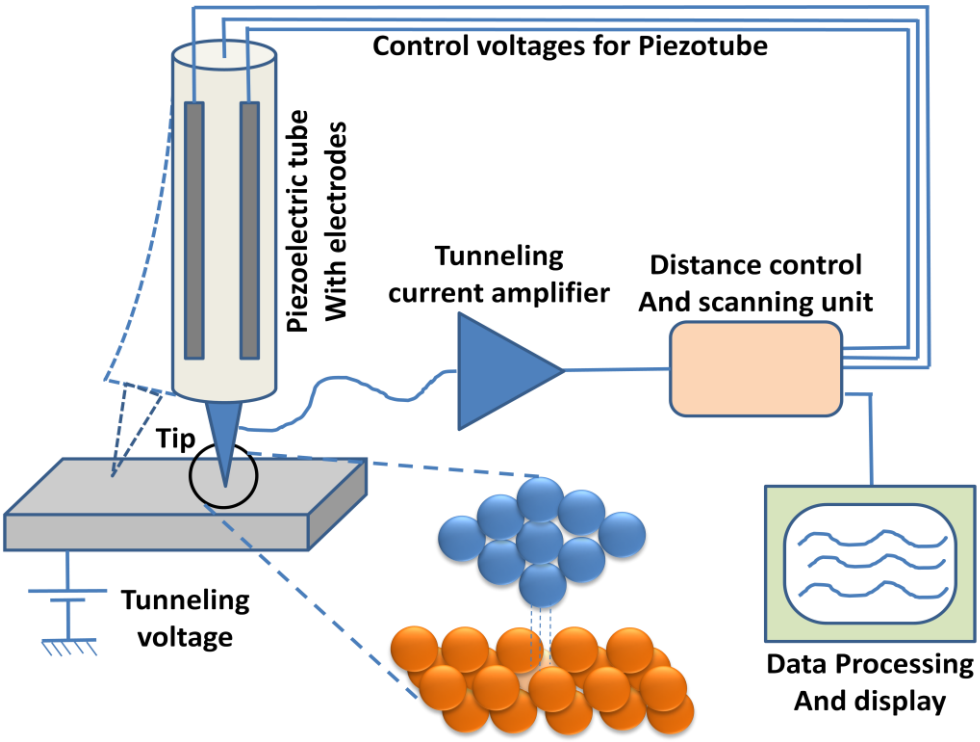

Fig. 2.2 A schematic drawing of a STM system (Wikipedia), including an atomic sharp metallic tip mounted on a piezoelectric tube with electrodes, voltage control circuit, feedback control circuit, signal amplifier, data processing and display terminal and a sample.

By some quantum mechanic calculations, one can get the tunneling current as [1]:

$$I \propto e^{-2k_2 Z} \tag{2.5}$$

For STM,

$$k_2 = \frac{\sqrt{2m\varphi}}{\hbar}$$

quantifies the decay of the wave inside vacuum barrier (φ is the work function of sample). From Eq. (2.5), one can see that the tunneling current is very sensitive to the sample-tip distance *Z*. If the distance decreases by 0.1 nm, the current will increase by a factor of ~10. So STM has a very high resolution at the direction perpendicular to the sample surface.

Figure 2.3 shows the energy diagrams of a system comprising of a tip and a sample in vacuum [1, 2]. The density of states (DOS) of the sample are shown as well. When the tip and sample are in a neutral floating state, their vacuum energy levels are aligned. The Fermi levels of the tip and sample lie below the vacuum level with a distance of φ_r and φ_s, which are the work functions of the tip and sample, respectively. If the tip and sample are close enough, and with a bias either on the tip or sample, there will be tunneling current from tip to the sample or from sample to the tip.

If the sample is positive biased and the tip is grounded, the Fermi level of the tip will be shifted upward and electrons will tunnel from the occupied states of the tip to the unoccupied states (above Fermi level) of the sample, as shown in Fig. 2.3 (a). So the STM image will show the empty state of the sample. On the other hand, if the sample is negative biased, the electrons will tunnel from the occupied states of the

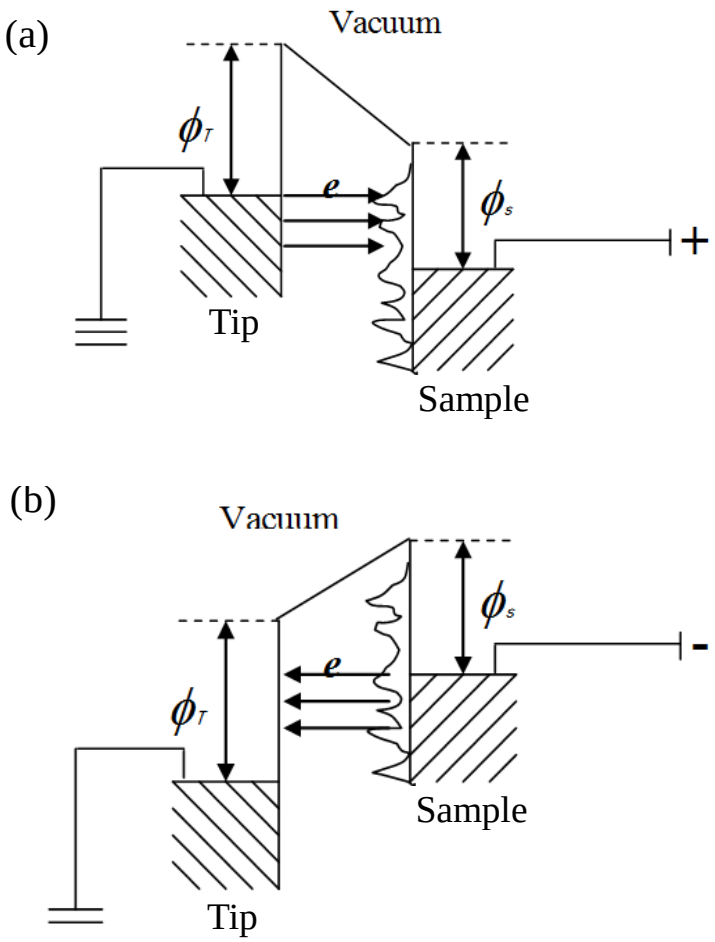

Fig. 2.3 Energy level diagram for (a) positive sample biased system; and (b) negative sample biased system.

sample to the unoccupied states of the tip (Fig. 2.3 (b)).

STM normally has two working modes: constant current mode and constant height mode. For the constant current mode, the feedback system keeps the current at a pre-set value (setpoint). If the current exceeds the setpoint, the distance (*Z*) between tip and sample will increase, resulting in a decrease in the tunneling current. If the current falls below the setpoint, the feedback system will reduce *Z*. This mode is frequently used because in most cases the surface will not be flat and this mode is most likely to keep the tip from crashing (striking the surface).

In the constant height mode, the servo feedback for the z piezoelectric crystal is turned off and the tip is scanned with no deflection along the z-axis. The constant height mode can be useful when scanning over an area which is small and flat in a high speed.

2.1.1.3 Basic Principles of STS

Besides the surface morphology information, STM also can measure the surface DOS of a sample. This section will give a brief overview of quantum explanation of the relation between STS and surface-DOS [3, 4].

Based on the first-order perturbation theory of the tunneling current [3]:

$$I(S,V) = \frac{2\pi e}{\hbar} \sum_{t,s} \left| M_{t,s} \right|^2 \delta(E_t - eV - E_s)\left[f(E_t - eV) - f(E_s) \right] \qquad (2.6)$$

where *S* represents the separation between the tip and sample, *V* is the sample bias voltage with respect to the tip, f_s and f_t is the Fermi-distribution function of sample

and tip. $M_{t,s}$ is the tunneling metric element between the wave functions of tip (Φ_t) and sample (Φ_s). E_t and E_s are the energies of tip and sample states corresponding to the wave function Φ_t and Φ_s.

Using Bardeen's method [3]:

$$M_{t,s} = -\frac{\hbar^2}{2m}\int(\psi_t^+ \nabla\psi_s - \psi_s \nabla\psi_t^+)dA \tag{2.7}$$

and WKB approximation, the tunneling current density can be written as:

$$J(S,V) \cong \frac{2\pi e}{\hbar}(\frac{\hbar^2}{2m})^2 \int_0^{eV} T(S,V,E)\rho_s(E)\rho_t(E-eV)dE \tag{2.8}$$

where *T(S, V, E)* is the tunneling probability:

$$T(S,V,E) \cong \exp\left\{ -2S\left[\frac{2m}{\hbar^2}(\phi + \frac{eV}{2} - E)\right]^{1/2} \right\} \tag{2.9}$$

So the derivative of Eq. (2.6) can be written as:

$$\frac{dI(S,V)}{dV} \cong A\Big[eT(S,V,E)\rho_S(E)\rho_t(E-eV)\Big|_{E=eV} + \int_0^{eV} T(S,V,E)\rho_S(E)\frac{d\rho_t(E-eV)}{dV}dE + \int_0^{eV}\frac{dT(S,V,E)}{dV}\rho_S(E)\rho_t(E-eV)dE\ \Big] \tag{2.10}$$

Assuming the DOS of tip is constant and the tunneling probability is constant under small voltage change, one can get:

$$dI/dV \propto \rho_s(eV) \tag{2.11}$$

where ρ_s is the surface DOS of the sample.

2.1.1.4 Preparation of STM Tips

In order to get a high-resolution STM image, an atomic sharp and stable tip is necessary. Normally, we use tungsten (W) or Pt/Ir wire to prepare the tip. A W-tip is usually prepared by electrochemical etching and Pt/Ir tip is prepared by mechanical cutting or polishing.

Fig. 2.4 shows the method for preparing a W-tip. As sketched in Fig. 2.4 (a), a W-wire (diameter at 0.25~0.50 mm) is dipped in a 4 mol/L NaOH solution. Two plastic tubes covering the W-wire are to protect the covered area and only the place of naked W-wire in the solution will be etched, as indicated by a red arrow. We use a circular Pt-wire as another electrode to ensure the top profile of the tip is in good conical shape. When a DC voltage (8-10V) is applied, the electrochemical etching process will carry on.

In the etching process, the current between the two electrodes is monitored by a commercial Omicron tip-preparation controller. The initial current is less than 200 mA, and with the etched part becoming thinner and thinner, the current will decrease to around 50 mA. Finally, when the joint part of W-wire (red arrow in Fig. 2.4 (a)) can not support the gravity of the lower part, it breaks and the current vanishes. We choose the lower part as the STM tip. The whole etching process normally lasts for ~20 min.

Fig. 2.4 (b) shows a scanning electron microscope (SEM) image of a W-tip made in our lab. Although under SEM, the top of the tip is very sharp, normally the tip still

(a)

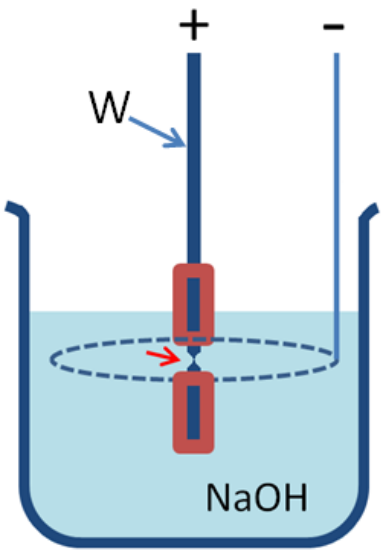

(b)

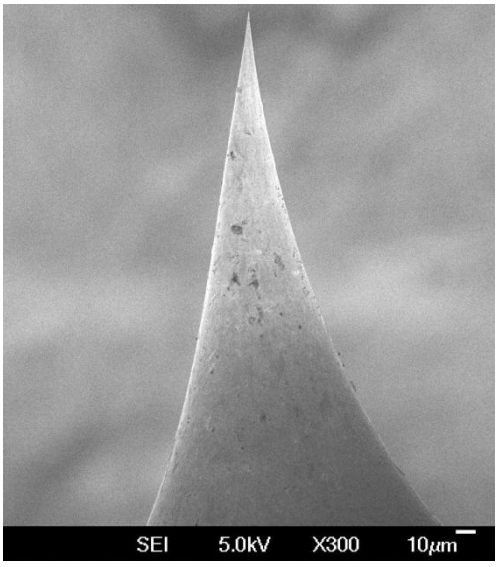

Fig. 2.4 (a) Schematic drawing of the electrochemical process for etching a W-tip; and (b) SEM image of a very sharp W-tip.

can not be used directly in the STM measurement. There is a thin oxide layer on top of the tip and the topmost profile of the tip is irregular. So we use electron bombardment in the vacuum chamber to remove the oxide layer and let the atoms on the topmost part rearrange to an atomic sharp profile. The electrons are produced by heating a W-filament. The tip is positive biased at around 400 V and placed close to the filament. With this tip-optimizing process, the W-tip can have good resolution and stability.

The Pt-Ir tips we use are commercial polished ones.

2.1.2 LEED

Electron beam can be used as a diffraction probe to analyze the surface crystallization properties. Because of the particle-wave duality, electrons can be treated as a wave, with the wavelength at:

$$\lambda = \frac{h}{\sqrt{2mE}} = \frac{12.25}{\sqrt{E\ (\text{in eV})}}\ \text{Å} \qquad (2.12)$$

where E is the kinetic energy of electrons.

Since the atomic spacing in solid is typically a few Å, normally electron energy smaller than 200 eV is used for LEED. The interaction of electrons with solid is much stronger than that of soft X-ray, so the elastic mean free path of electrons is quite short. This makes the electron beam a surface sensitive probe to investigate the surface.

In the LEED experiment, a well-defined low energy beam of electrons is incident

normally on the sample, as shown in the schematic drawing of a LEED device in Fig. 2.5 (a). The diffracted electrons can be observed by a fluorescent screen after energy filtering grids, which selects only the electrons with the same kinetic energy as the primary electrons. Fig. 2.5 (b) and (c) show the real space diffraction situation for a 2D cross-section and 3D side view, respectively. For both case, the path difference is indicated by red dotted lines. The lattice period is "*a*" for 2D and "*d*" for 3D. The scattered electron beam should meet the following conditions to be constructive interfered:

$$\text{2D:} \quad a \sin\theta = n\lambda \tag{2.13}$$

$$\text{3D:} \quad 2d \sin\theta = n\lambda \tag{2.14}$$

Fig. 2.5 (d) shows an example of LEED pattern of √3×√3-Ag on Si(111). To interpret the LEED pattern, one should use the relation equation of real space lattice and reciprocal lattice. The basic vectors in 3D reciprocal lattices are:

$$\mathbf{a_1^*} = 2\pi \frac{\mathbf{a}_2 \times \mathbf{a}_3}{\mathbf{a}_1 \cdot (\mathbf{a}_2 \times \mathbf{a}_3)} \qquad \mathbf{a_2^*} = 2\pi \frac{\mathbf{a}_3 \times \mathbf{a}_1}{\mathbf{a}_1 \cdot (\mathbf{a}_2 \times \mathbf{a}_3)} \qquad \mathbf{a_3^*} = 2\pi \frac{\mathbf{a}_1 \times \mathbf{a}_2}{\mathbf{a}_1 \cdot (\mathbf{a}_2 \times \mathbf{a}_3)} \tag{2.15}$$

Normally, we only analyze the LEED pattern in 2D case, so Eq. (2.15) can be simplified as:

$$\mathbf{a_1^*} = 2\pi \frac{\mathbf{a}_2 \times \mathbf{n}}{\mathbf{a}_1 \cdot (\mathbf{a}_2 \times \mathbf{n})} \qquad \mathbf{a_2^*} = 2\pi \frac{\mathbf{n} \times \mathbf{a}_1}{\mathbf{a}_1 \cdot (\mathbf{a}_2 \times \mathbf{n})} \tag{2.16}$$

where ***n*** is the unit normal vector of the 2D plane.

The detailed analyzing method and result will be discussed in the chapter of Bi/Ru(0001) experiment.

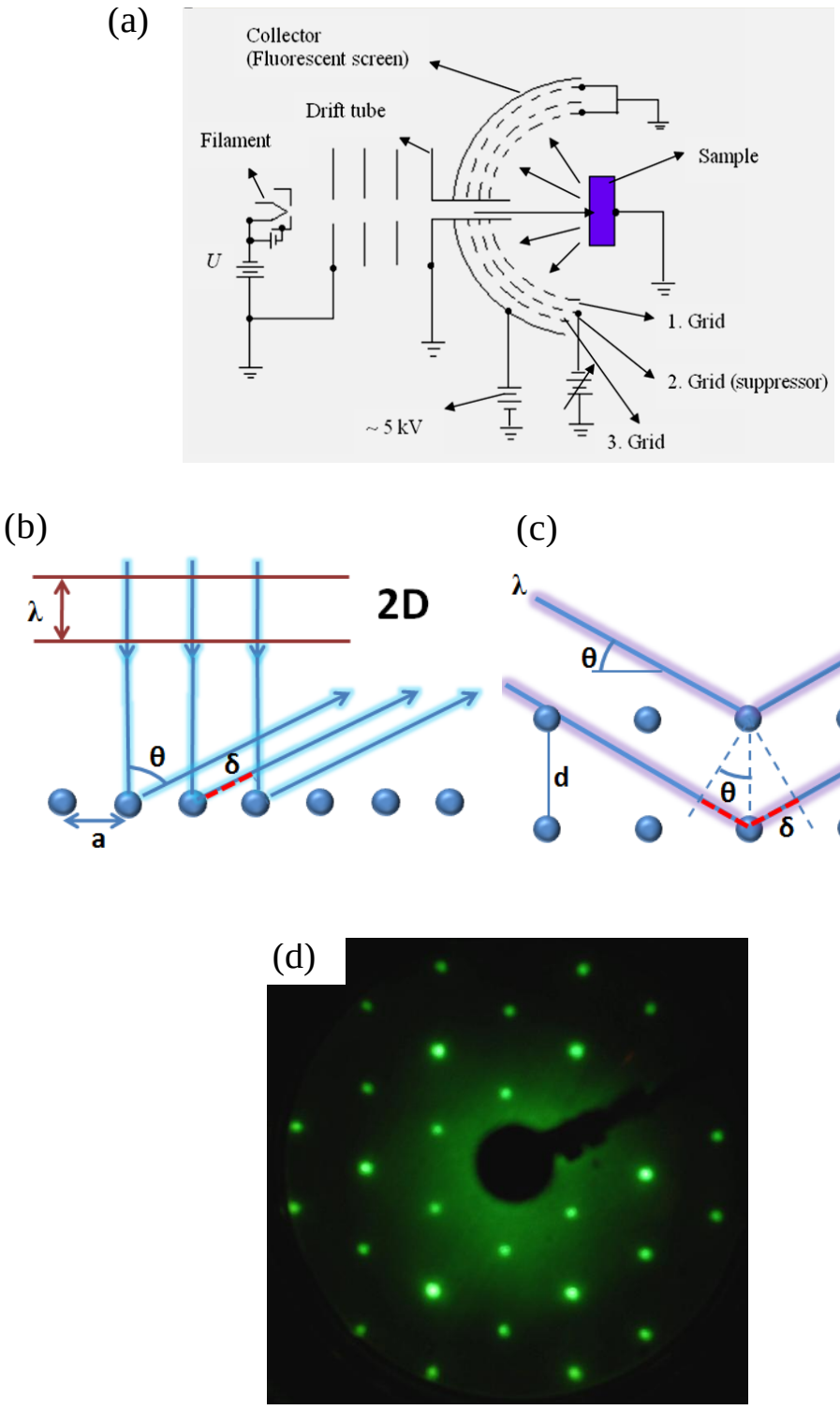

Fig. 2.5 (a) Schematic drawing of the LEED device; diffraction situation of a (b) 2D and (c) 3D case; and (d) photo of a LEED (66.3 eV) pattern of √3×√3-Ag on Si(111).

2.1.3 AES

AES is a specific technique utilizing the emission of electrons in the Auger process and is one of the most commonly employed surface analytical techniques for determining the composition of the surface layers of a sample. Fig. 2.6 (a) illustrates the process of how an Auger electron is generated. One electron was removed from a core-level by high energized electrons, and then an electron in a higher level would drop down to fill the core hole. The energy released was absorbed by another electron which would exit the shell. This exited electron is called Auger electron.

To detect the Auger electron, three important analyzer are normally used: retarding field analyzer (RFA), cylindrical mirror analyzer (CMA) and concentric hemisperical analyzer (CHA). In our experiment, RFA is used because it is the simplest type of analyzer in which a LEED system is used as energy analyzer. Fig. 2.6 (b) shows the typical configuration of a RFA. In the simplest form, a negative voltage, U_r is applied on the repeller grids with respect to the sample, so that the emitted electrons with an energy $<eU_r$ cannot pass through the grid, i.e. the system functions as a high-pass filter. This potential is then varied and the collector current is measured at the screen. In practice, modifications of this arrangement are often used.

The collected Auger electrons are plotted as a function of energy against the broad secondary electron background spectrum. Since the intensity of the Auger peaks may be small compared to the background, AES is often run in a derivative mode which serves to highlight the peaks by modulating the electron collection

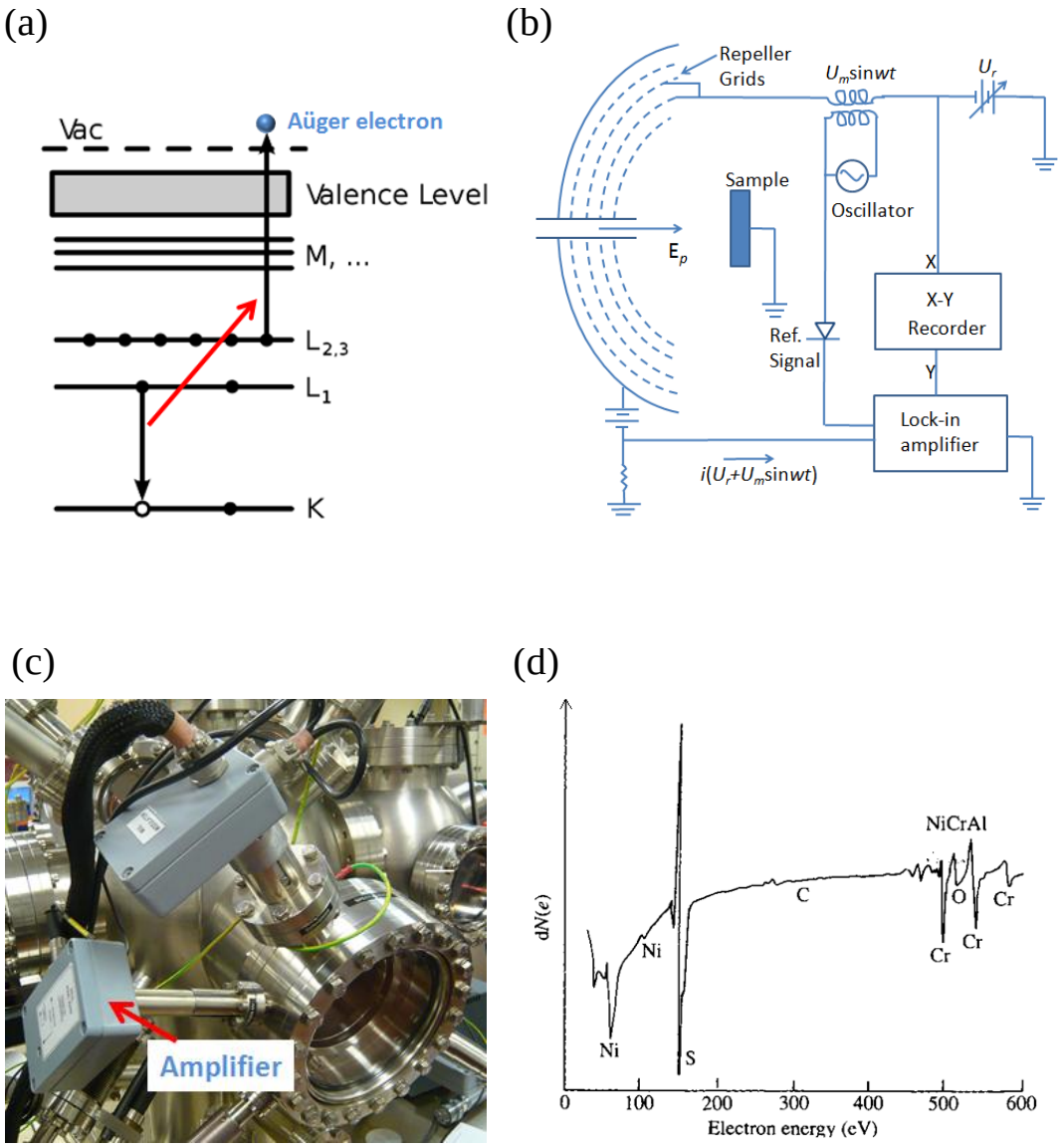

Fig. 2.6 (a) Schematic drawing of the process of generating an Aüger electron; (b) The equipment configuration of a typical AES device; (c) A photo of the Omicron AES equipment mounted in our UHV chamber; and (d) An example of AES data curve.

energy via a small applied AC voltage. Fig. 2.6 (c) shows a photo of AES equipment with signal cable and pre-amplifier unit. Fig. 2.6 (d) shows an example of AES data curve including several elemental peaks. Since the Auger electrons have different and fixed kinetic energies from different elemental atoms, AES is an elemental sensitive measurement. Moreover, because electrons have short mean free path in a solid, the escape depth of electrons is therefore localized to within a few Å of the target surface, giving AES an extreme sensitivity to surface species.

2.1.4 PES (XPS/UPS)

PES utilizes photo-ionization and energy- dispersive analysis of the emitted photoelectrons to study the composition and electronic state of the surface region of a sample. According to the source of exciting radiation, the PES can be subdivided into:

a) X-ray Photoelectron Spectroscopy (XPS), using soft x-ray (200-2000 eV) radiation to examine core-levels.

b) Ultraviolet Photoelectron Spectroscopy (UPS), using UV (10-50 eV) radiation to examine valence levels.

XPS is another commonly used technique to analyze elemental composition, which is also known as ESCA, an abbreviation for Electron Spectroscopy for Chemical Analysis. By shining a well-defined X-ray beam onto a material, the photons can excite electrons bound at core levels of atoms, and if the photon energy $h\nu$ is sufficient, the excited electrons can escape from the sample to the vacuum. Fig.

2.7 (a) shows the typical process of generating an X-ray excited photoelectron. By measuring the kinetic energy and the number of electrons that escape from the sample, one can obtain the spectrum. Fig. 2.7 (b) shows a schematic drawing of the configuration of a XPS system. XPS can be performed using either a commercially built XPS system or a synchrotron-based light source combined with a custom designed electron analyzer.

Without other energy loss event, the kinetic energy of photoelectrons is:

$$E_{kin} = h\nu - E_B \tag{2.17}$$

where E_B is the binding energy, which is related to the energy which a electron escapes from the core to the vaccum. Moreover, because of the short elastic mean free path of electrons in solid, the probing depth of XPS is within a few nm, so it is quite suitable to nanostructures at or near the surface of a solid. Comparing to AES, XPS involved only one electron process. The peaks of XPS are normally simple and sharp.

Using UV light ($h\nu$=5–100 eV) to excite photoelectrons, the electronic states of the valance band can be probed in UV photoelectron spectroscopy. From an analysis of the kinetic energy and angular distribution of the photoelectrons, information of DOS, Fermi level shift, work function and chemical states can be extracted with surface sensitivity. UPS spectra also have strong angular dependence for the excited electron, which can give information about band structure in the $\boldsymbol{k}$ space.

(a)

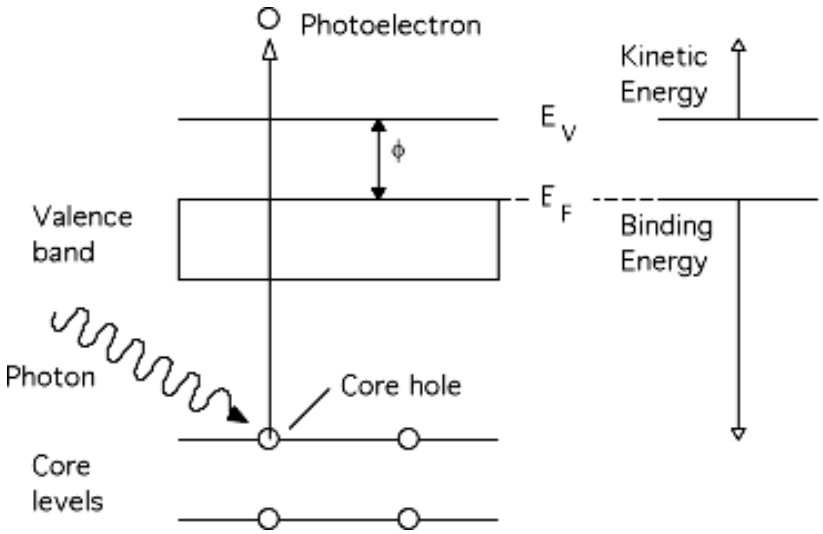

(b)

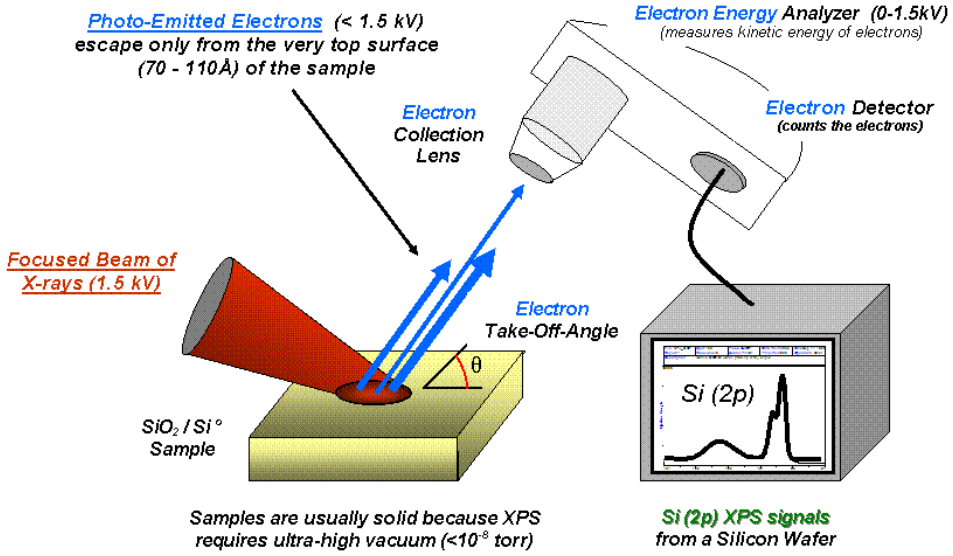

Fig. 2.7 Schematic drawing of (a) process of generating a photoelectron by X-ray photon; and (b) basic configuration of XPS system.

2.2 Substrates and Preparation Methods

2.2.1 Inert and Ruthenium Substrates

There are two kinds of inert substrates which are widely used: HOPG and molybdenum disulfide (MoS_2). HOPG consists of many atomic layers of carbon sheet (graphene) highly oriented among each other, stacking in the [0001] direction. A photograph of a HOPG substrate (1cm×1cm) is shown in Fig. 2.8 (a). From the viewpoint of crystallography, graphite belongs to lamellar materials, and consists of identical staked planes with a inter-plane distance of 3.41 Å (Fig. 2.8 (b)). The graphitic sheets are not necessarily azimuthally aligned with each other, so HOPG is a polar-oriented polycrystalline material. The schematic atomic structure in a (0001) graphene layer and an atomic resolution STM image are shown in Fig. 2.8 (c) and (d), respectively. It has a hexagonal (HEX) order with a period of 2.46 Å. The trigonal bonding in each graphene sheet involves overlap of carbon sp^2 hybrid orbitals in the plane, whereas the overlap of carbon p_z orbitals produces delocalized rings of π electrons lying above and below each benzene ring, which makes graphite an electrical conductor. The graphene layers are bonded to each other by weak van der Waals forces, so that they can easily slide over one another and be cleaved by using scotch tapes. It was tested that HOPG does not outgas at the temperatures up to 600 ℃ and remains stable up to 2000 ℃ in inert environment. These properties make HOPG the excellent substrate for growing near free-standing nanostructures and for STM measurement.

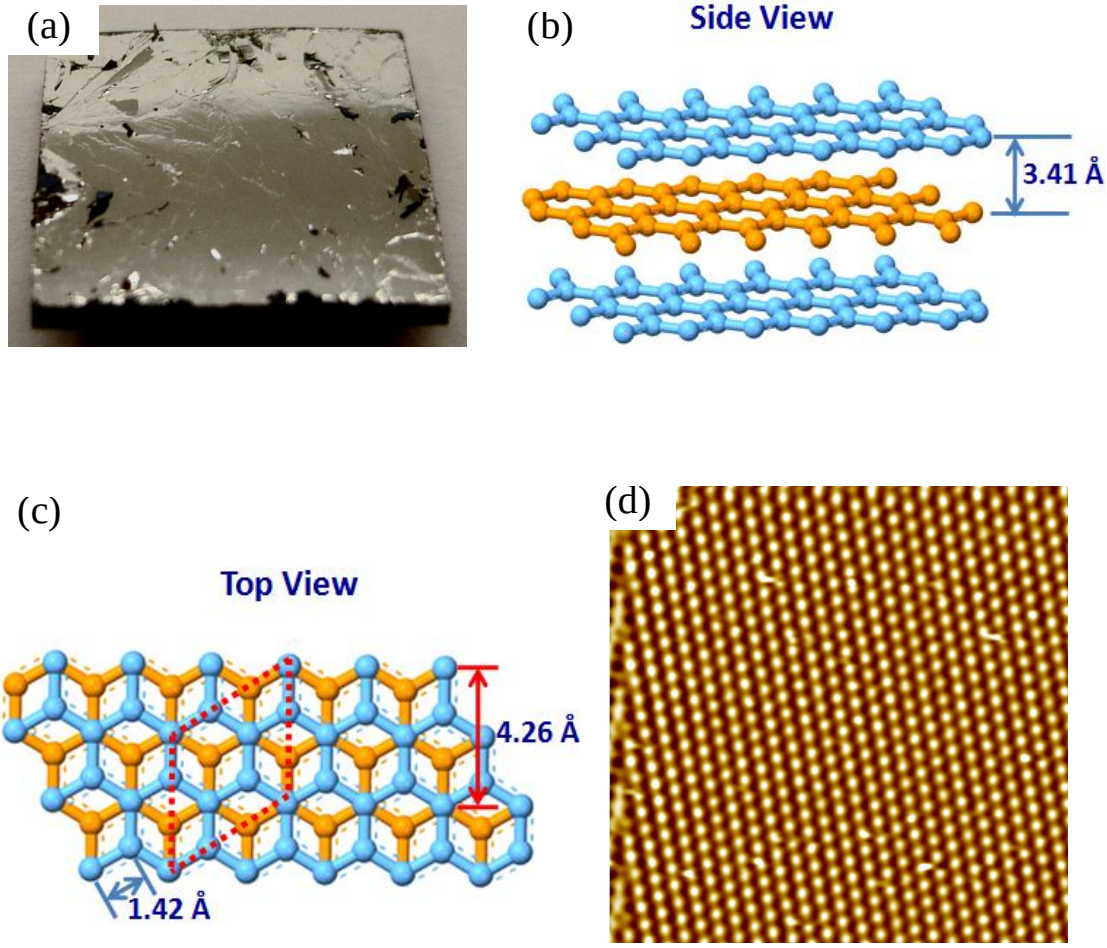

Fig. 2.8 (a) Photograph of a HOPG substrate (1cm×1cm); (b) Side view of HOPG atomic layers with inter-plane distance of 3.41 Å; (c) Top view of graphitic atomic layers with honeycomb like HEX structure; (d) Atomic-resolution STM image of clean HOPG surface (5nm×5nm).

Like HOPG, MoS_2 is a layer-structured semiconductor (shown in Fig. 2.9 (a)), consisting of (0001)-oriented S-Mo-S sandwich layers as shown schematically in Fig. 2.9 (b). Each Mo center is trigonal prismatic, being bound to six sulfide ligands, each of which is pyramidal. The Mo atoms form a hexagonal array in the layer plane with a period of 3.16 Å. The two layers of S atoms with the same periodicity are located 1.59 Å above and below the Mo layer, as shown in Fig. 2.9 (c). Fig. 2.9 (d) shows a typical atomic-resolution STM image of a clean MoS_2 surface. Similar with HOPG, the S-Mo-S sandwich layers are weakly bound (van der Waals force) to one another, so it is easy to be cleaved using scotch tapes. The spacing between the neighboring sandwich layers is 6.15 Å. The MoS_2 samples used in our experiment is natural mineral in the *2H* polytype, which has an ABAB… repetitive stacking sequence.

The surface energy of HOPG and MoS_2(0001) is approximately 0.16-0.20 J/m^2 and 0.26 J/m^2 respectively. Although these values are only slightly different with each other, there may be noticeable differences in the morphology of nanostructures grown on HOPG and MoS_2. In addition, graphite is semimetallic whereas MoS_2 is semiconducting. Different interfacial electronic states may be induced when materials are deposited on them.

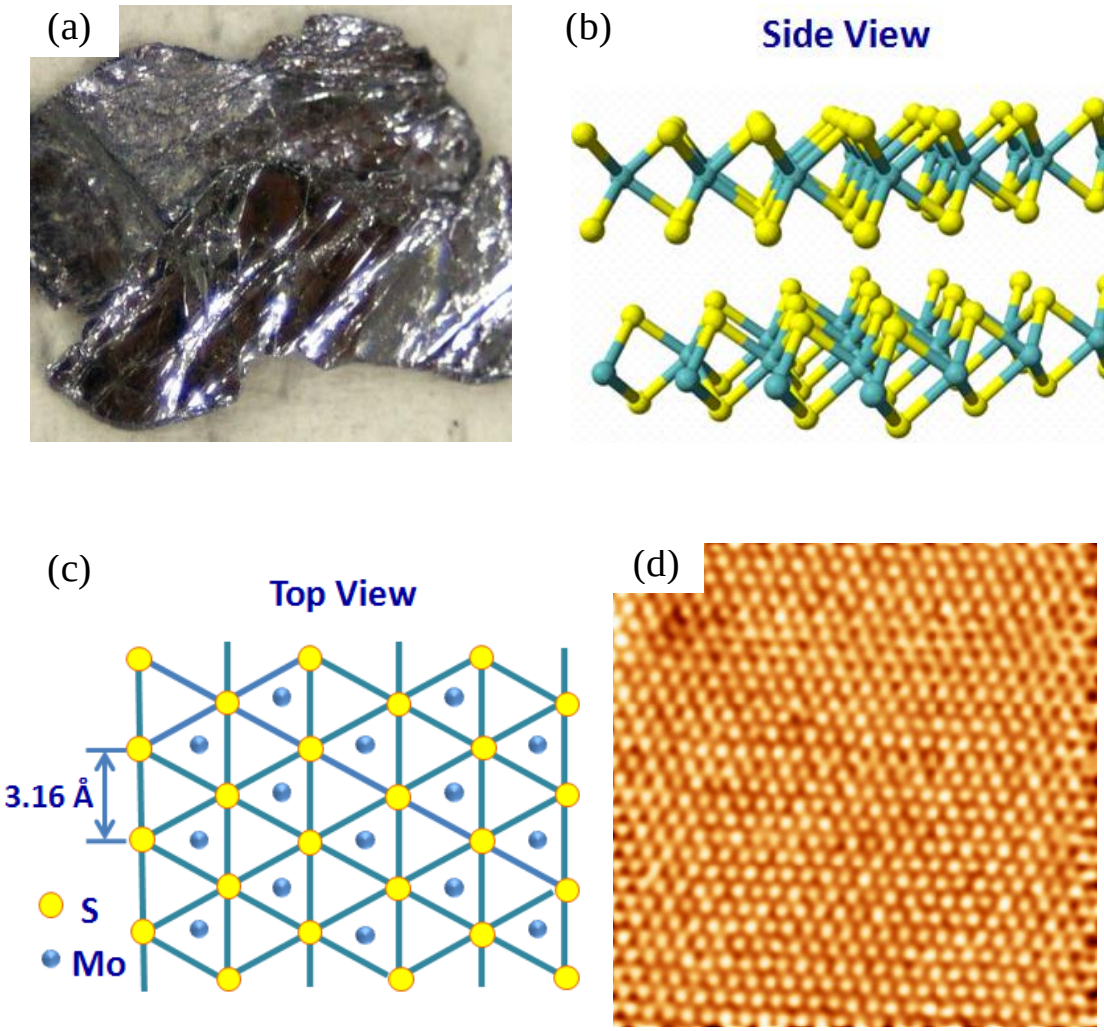

Fig. 2.9 (a) A photograph of a MoS_2 substrate in a irregular shape; (b) Side view of MoS_2 atomic layers structures; (c) Top view of MoS_2 atomic layers with HEX structure; (d) Atomic-resolution STM image of clean MoS_2 surface (5nm×5nm).

Ruthenium is a rare transition metal of the platinum group in the periodic table. It is found associated with platinum ores and usually used as a catalyst in some platinum alloys. In SPM experiments, Ru single crystal substrate is normally well polished at the (0001) surface. A photo of our Ru(0001) sample is shown in Fig. 2.10 (a). The atomic resolution STM image of clean Ru(0001) surface is shown in Fig. 2.10 (b) with the lattice constant of 2.71 Å. Ruthenium is a good catalyst for reactions with H_2 and CO and for reactions involving organic synthesis [6, 7]. Numerous studies have been devoted to determine the structures formed by hydrogen on Ru, particularly on its closed-packed hexagonal face [8]. Recently, finding of epitaxial graphene (EG) layers on Ru(0001) makes Ru a promising substrate to fabricate large area EG. Comparing to the graphene layers made by micromechanical cleavage, chemical exfoliation and thermal decomposition of SiC, EG layers on Ru(0001) have many advantages: such as high crystalline quality, good long-range order and large area [9]. In addition, epitaxial growth of metals (e. g. Au, Ag) [10] and organic materials [11] on Ru(0001) have attracted much interest in the last few decades due to their potential applications.

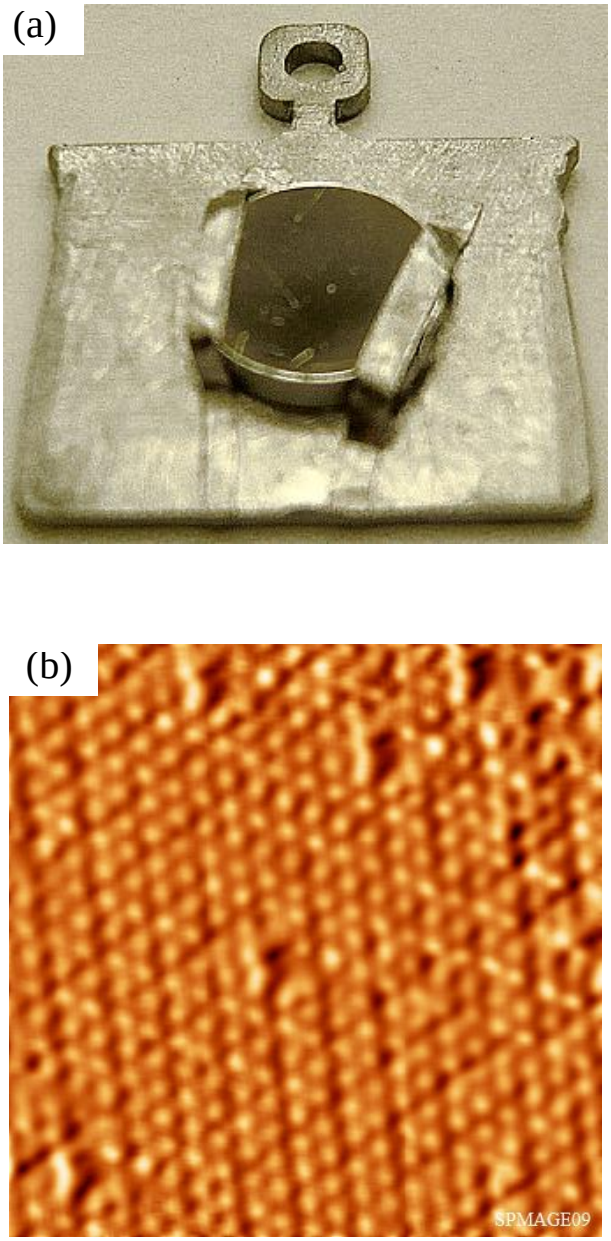

Fig. 2.10 (a) Photo of a Ru(0001) substrate with diameter of 10mm and thickness of 2 mm, mounted on an Omicron STM sample holder; (b) Atomic resolution STM image (6nm×6nm) of clean Ru(0001) surface with HEX lattice.

2.2.2 Preparation of Clean Substrate Surfaces

Due to the layered structures of HOPG and MoS_2, they are easily cleaved by using a scotch tape. During cleaving process, one should stick the scotch tape onto the substrate surface and tear off the tape. It is necessary to avoid sticking the glue on the tape onto the Ta-pin and holder to prevent contaminations. When using a tweezer to push the tape onto the sample surface, one should avoid using large force. After cleaving, to avoid contamination, inert substrates need to be transferred into the UHV chamber as soon as possible. In the UHV chamber, we use filament heating to degas the sample surface to remove the water and other contaminations. The degassing temperature is: for HOPG, at ~600 ℃; for MoS_2, at ~400 ℃. Normally the degassing process takes ~8 hours.

For Ru(0001) substrate, we heat the sample at 1200 ℃ using electron-beam bombardment for ~2 mins several times to remove the surface contaminations.

2.2.3 Experimental Methods of Preparing Nanostructures

In the experiment, we use tantalum-boat (Ta-boat) to evaporate most flake- or granular source, such as Bi, Sb, Mn, Ge, CdSe and CdS. Ta-boat is easy to be installed and stable with low cost. Fig. 2.11 (a) shows an empty Ta-boat mounted in the UHV chamber. For wired material, such as Au, Ag, Fe, Cu and In, we use

tungsten-filament (W-filament) to evaporate them. A short portion (normally 2~3 mm in length and 0.1~0.3 mm in diameter) of a material wire is twisted onto a degassed W-filament and mount into the UHV chamber. When the filament is heated to a certain temperature, the metal wire melts and coats on the filament to be a stable metal source. Fig. 2.11 (b) shows an empty W-filament source.

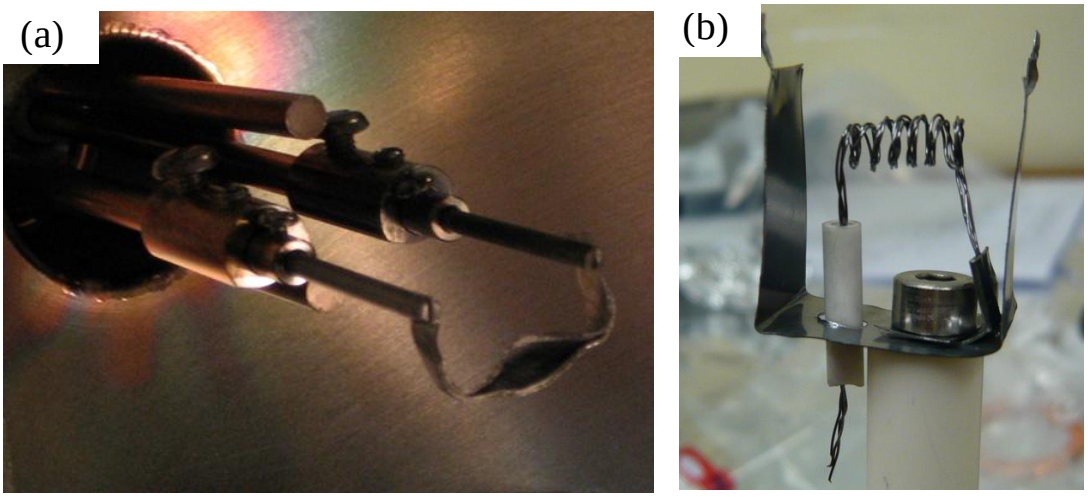

Fig. 2.11 (a) An empty Ta-boat mounted in the UHV chamber. (b) A degassed empty W-filament for metal deposition.

2. 3 Multi-component UHV-STM Chamber Setup

In this work, most of in-situ experiments were carried out in a commercial Omicron multi-chamber UHV system with a RT-STM. The base pressure is ~5×10^{-11} mbar, where the vacuum is maintained by combination of ion pump, titanium sublimation pump (TSP), turbo-molecular pump (TMP) and mechanical pump. The pressure was measured by using ion gauge. The schematic drawing of the UHV system setup is shown in Fig. 2.12 (a). The system consists of an analysis chamber, preparation chamber and load-lock chamber separated by gate valves. The analysis chamber is equipped with a RT-STM, four grid optics for LEED and AES. Both chambers contain X-Y-Z-manipulator which is used for sample transfer, degassing, cleaning and for deposition purpose. The motion of the manipulator is linear and rotational with four degrees of freedom. The sample holders in both manipulators have two different heating methods, i.e., (1) resistive filament heating, for sample temperature up to 1000 K; (2) electron beam (E-beam) bombardment heating, for sample temperature up to 1600 K. The load-lock chamber for introduction of the sample and tip is equipped with a small TMP. The sample transfer from the load lock chamber to preparation chamber is performed by two magnetic transfer arms, as shown in Fig. 2.12 (a). Fig. 2.12 (b) shows the photo of the UHV-STM system.

Besides RT-STM, LT STM/STS was also used to characterize some RT-grown Bi nanostructures on Ru and HOPG. Fig. 2.13 shows the schematic layout diagram of the Unisoku 1500 STM.

(a)

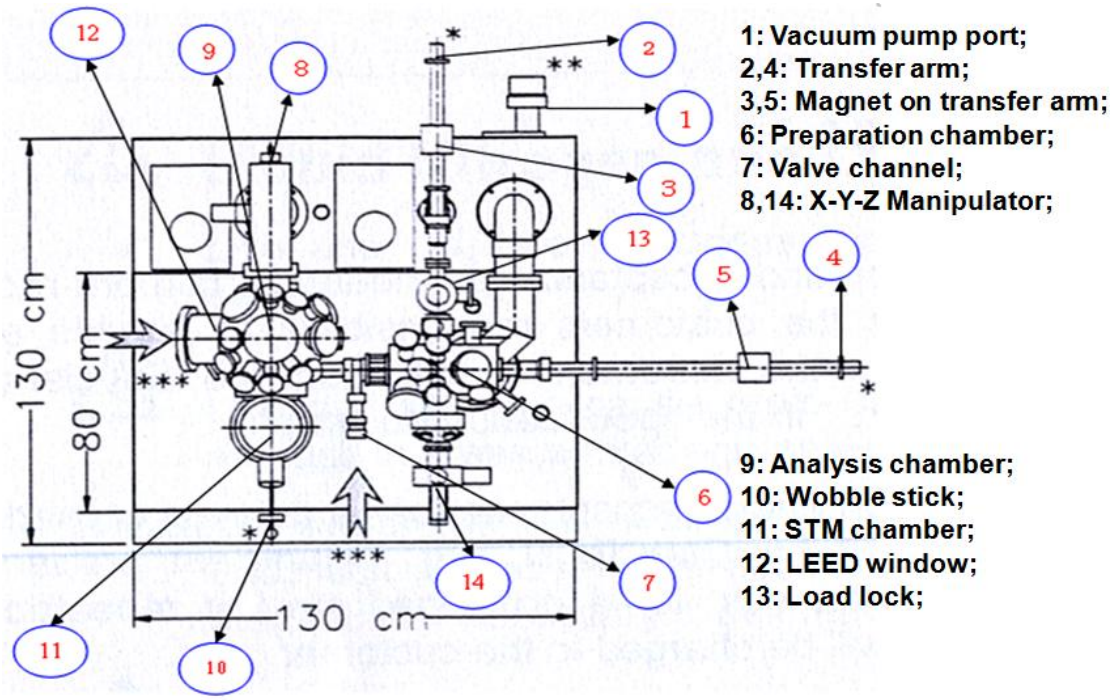

(b)

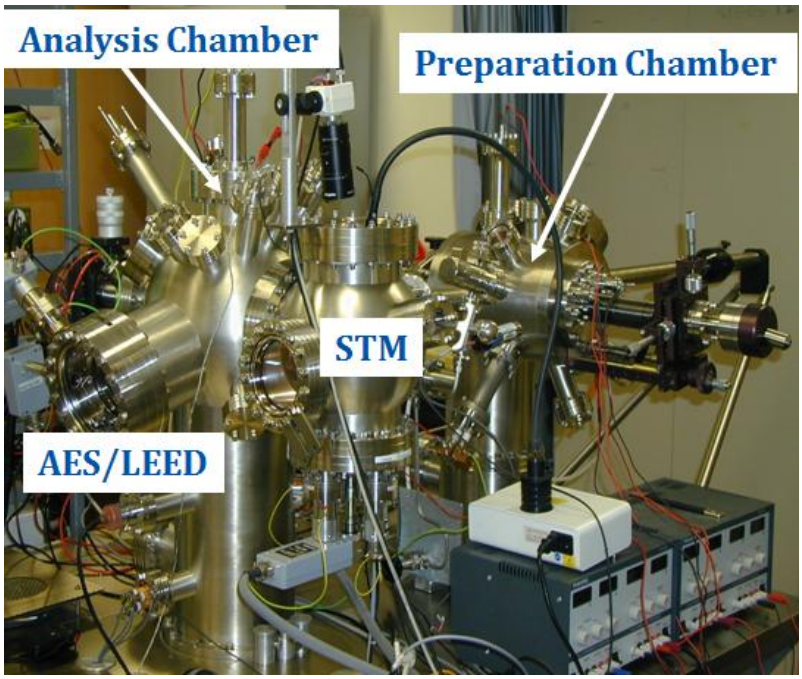

Fig. 2.12 (a) Schematic drawing of the UHV RT-STM system setup. (b) Photo of the Omicron UHV-STM compact system.

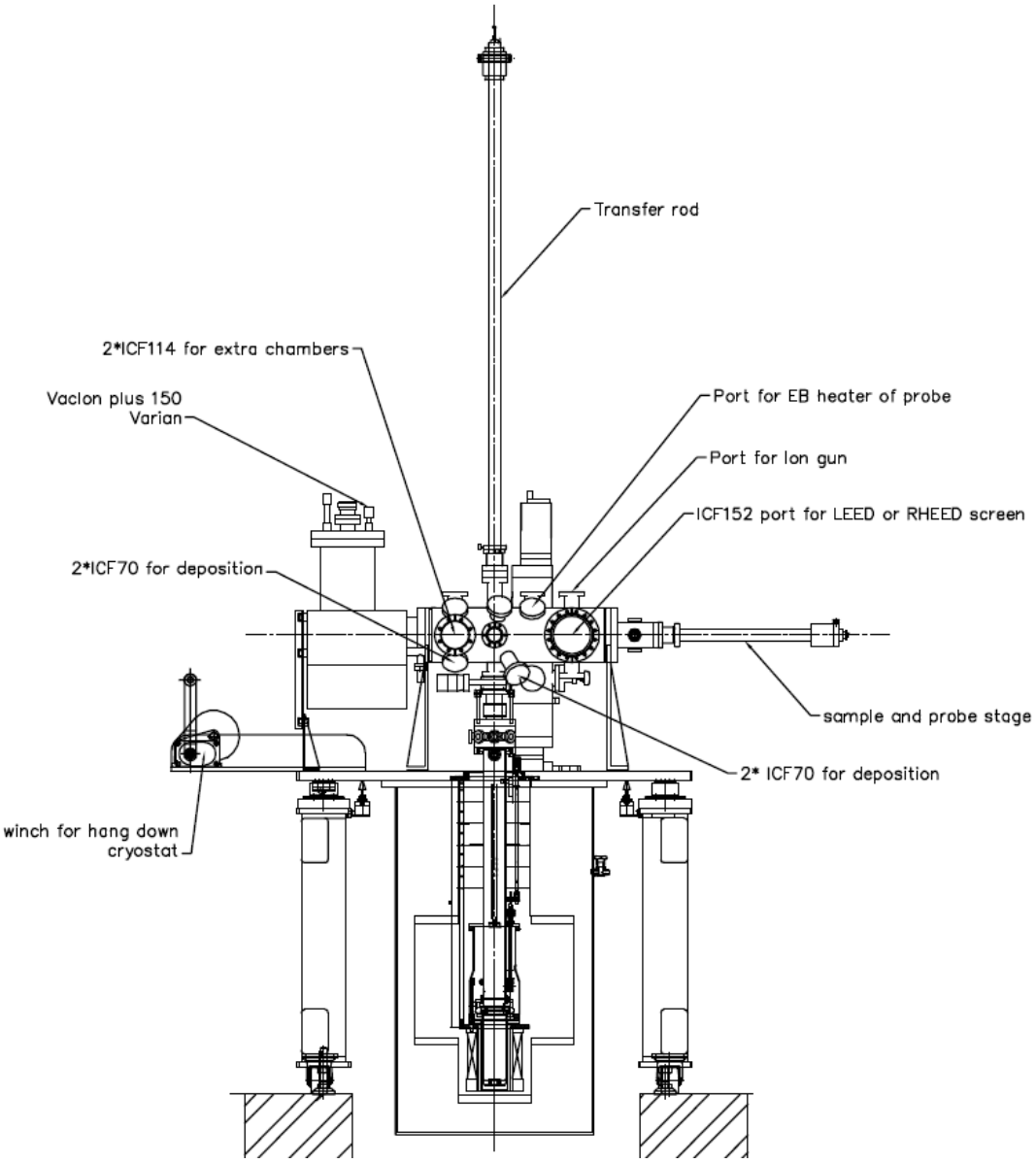

Fig. 2.13 The schematic layout diagram of the Unisoku 1500 STM.

Reference

[1] R. Wiesendanger, H.-J. Guntherodt, et al., Scanning tunneling microscopy I: general principles and applications to clean and adsorbate-covered surfaces, Berlin ; New York: Springer , c1992.

[2] R. Wiesendanger, H.-J. Guntherodt, et al., Scanning tunneling microscopy III: theory of STM and related scanning probe methods, Berlin; New York: Springer, c1996.

[3] A. Selloni, P. Carnevali, E. Tosatti, and C. D. Chen, Phys. Rev. B **31**, 2602 (1985).

[4] V. A. Ukraintsev, Phys. Rev. B **53**, 11176 (1996).

[5] J. A. Stroscio, D. T. Pierce, A. Davies, R. J. Celotta, and M. Weinert, Phys. Rev. Lett. **75**, 2960 (1995).

[6] Y. J. Bei, S. D. Zhang, J. C. He, J. C. Wu, Y. Yang, Platinum Metals Rev. **49**, 91 (2005).

[7] S.-I. Murahashi, H. Takaya, T. Naota, Pure Appl. Chem. **74**, 19 (2002).

[8] H. Shi, K. Jacobi, Surf. Sci. **313**, 289 (1994).

[9] Y. Pan, H. Zhang, D. Shi, J. Sun, S. Du, F. Liu, and H.-J. Gao Adv. Mater. **21**, 2777 (2009).

[10] W. L. Ling, J. C. Hamilton, K. Thürmer, G.E. Thayer, J. de la Figuera, R.Q. Hwang, C.B. Carter, N.C. Bartelt and K.F. McCarty, Surf. Sci. **600**, 1735 (2006).

[11] Y. F. Xu, H. J. Zhang, Y. H. Lu, B. Song, Q. Chen, H. Y. Li, S. N. Bao, and P. He, Surf. Sci. **600**, 2002 (2006).

Chapter 3 Growth of Bismuth Nanostructures on MoS_2(0001) and STS Study of Bismuth on HOPG

3.1 Introduction

Bismuth is a prototypical group-V semimetal which has attracted much attention because of its unique properties due to the tiny overlap between valence and conduction bands. Its Fermi energy is only about 25 meV [1], and the electronic de Broglie wavelength is about 30 nm [2]. The nano-structures of Bi have been extensively studied toward the development of devices based on quantum size effect [3-5], extremely large magnetoresistance [6], and a probable semimetal to semiconductor transition [7]. Recently, quantum spin Hall effect has been predicted for Bi [8], indicating its potential in spintronics applications.

In ambient conditions, Bi crystallizes in the rhombohedral A7 structure (or α phase), which can be derived by a slight distortion of a cubic lattice, as shown in Fig. 3.1 (a). The covalent bond angle β is 95.5 °. One distorted fcc representation of α-Bi is illustrated in Fig. 3.1 (b), with the ABC stacking of covalent-bonded (111) bi-layers (BL) spaced at 3.95 Å. Each Bi atom forms covalent bonds with three nearest neighbors within the bilayer (top view) [9]. Unlike on Bi(111) surface, there are dangling bonds on bulk-terminated Bi(110) surface as shown in Fig. 3.1 (c) with a rectangular surface unit cell (top view) [10]. The dangling bonds can be removed by

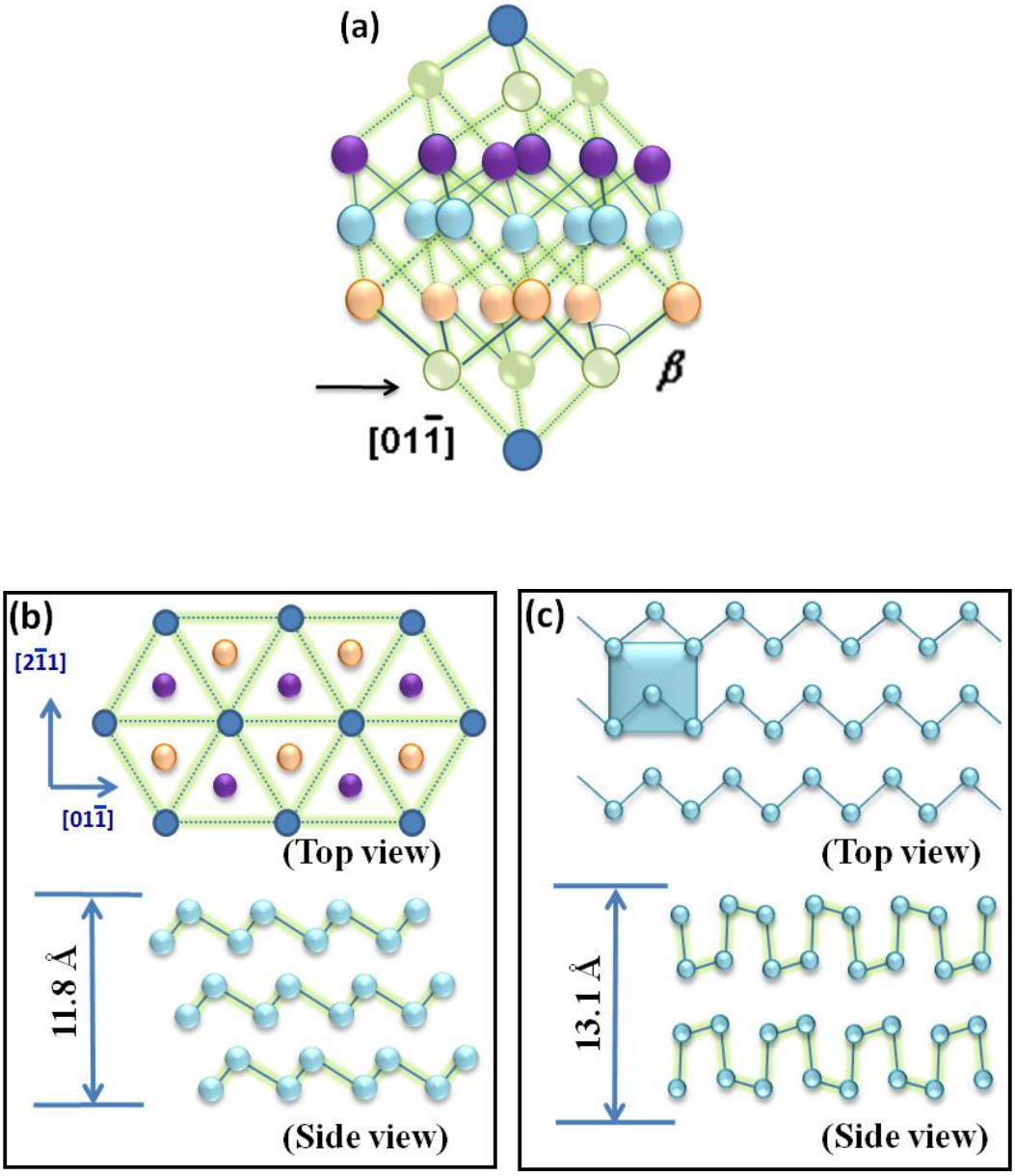

Fig. 3.1 Schematics of rhombohedral lattice for bulk Bi crystals in (a) a pseudo-cubic cell; top and side views of (b) Bi(111) and (c) Bi(110) plane. The thickness of 3-BL Bi(111) and 4-ML Bi(110) are indicated in the side-view (b) and (c), respectively.

pairing up (110) monolayer (ML) into puckered BL [11]. The side-view of puckered Bi(110) is also shown in Fig. 3.1 (c). The nominal thickness of one Bi(110) BL in bulk Bi is 6.55 Å.

Bi deposition on a variety of substrates has been investigated over decades, with both island and continuous film morphologies observed [6, 11-18]. In particular, Bi deposition on highly oriented pyrolytic graphite (HOPG), which is a well-known inert substrate, has been extensively studied by Brown *et al* [15, 18, 19]. Nanoscale rods, dendrites and stars have been observed on HOPG indicating an island growth mode due to a weak bonding between the deposited atoms and substrate. MoS_2(0001), with a hexagonal symmetry and a surface lattice constant of 3.16 Å, is another widely-used inert substrate for studying the self-assembly behavior of various materials such as Au, Pd, and organic molecules [20, 21]. When bonding between an adsorbate and substrate is week, island aggregation usually takes place in the early stages of film growth, forming nearly free-standing structures [15]. The surface energy of MoS_2(0001) is approximately 0.26 J/m^2. Although this value is only slightly higher than that of HOPG, it can lead to noticeable differences in growth morphology.

In this chapter, I present the results of our *in situ* STM study of the growth and morphologies of Bi nanobelts (nanoribbons) and thin films on MoS_2(0001). Our STM images show that Bi(110) nanobelts (nanoribbons) formed at low deposition amount before the islands thickness reaches 8 Bi(110)-ML. A structural transformation from Bi(110) to Bi(111) was observed when the Bi(110) film thickness exceeds this critical thickness. Other measurements such as scanning electron microscopy (SEM) and

LEED were also used to characterize these Bi nanostructures. In addition, Bi nanostructures deposited on HOPG are studied by LT-STS. Thickness dependent local DOS (LDOS) on Bi(110) layers with different thickness was observed, which may result from the structural relaxation and transformation from Black-P like Bi(110) to bulk-like one.

The following sub-sections show the experimental method, formation of nanobelts/nanoribbons, ultra-thin Bi(110) film and single-crystal Bi(111)-film in detail. The growth mechanism and structural properties of Bi nanostructures on MoS_2(0001) are discussed as well.

3.2 Experimental Method

The experiments were mainly carried out in an ultrahigh vacuum (UHV) system (base pressure 5×10^{-11} Torr) equipped with a room-temperature (RT) STM, Auger electron spectroscopy (AES) and LEED [22]. Clean MoS_2 substrates were prepared by cleaving in air and then quickly transferred into the UHV system, followed by an overnight degassing at 400 ℃. High purity (99.999%) Bi was evaporated from a Ta boat and deposited on clean MoS_2 surfaces at RT. Before the deposition, Bi source was degassed at appropriate temperatures for a few hours in order to remove contamination. The flux was calibrated using AES and STM. One substrate was deposited with Bi at a flux of 0.33 Å/min and imaged at RT. The other substrate was deposited with Bi flux of 0.12 Å/min and imaged by a low-temperature (LT) STM at

77 K. STM images were carefully calibrated and the scanner drift was corrected [10]. The SEM image was taken *ex situ* with a JEOL JSM-6700F field emission SEM at 5 kV. In addition, the LDOS of Bi nanostructures on HOPG was investigated *in situ* using a Unisoku LT-STM at 77 K. Bi was evaporated on clean HOPG at RT with a flux of 0.33 Å/min. All STM images on HOPG were taken at 77 K. The dI/dV spectrum was acquired using a lock in amplifier with the bias voltage modulated at a frequency of 600 Hz and a peak-to-peak amplitude of 30 mV.

3.3 Results and Discussions

3.3.1 Formation of Nanobelts at Low Flux

Fig. 3.2 (a), (b) and (d) show the STM images (taken at 77 K) of Bi nanobelts on MoS_2 surface formed under a deposition flux of 0.12 Å/min. Initially, with 0.66 Å Bi deposited, the nanobelts coverage is low, leaving about 85% of the substrate surface uncovered. The width of the nanobelts is in a narrow distribution range around 10.9 nm and the average length is 95 nm. After 1.3 Å Bi deposition, the density of the nanobelts increases by about one time while the average width increases little. A few nanobelts have irregular shape which can be seen in Fig. 3.2 (b). The height profile of

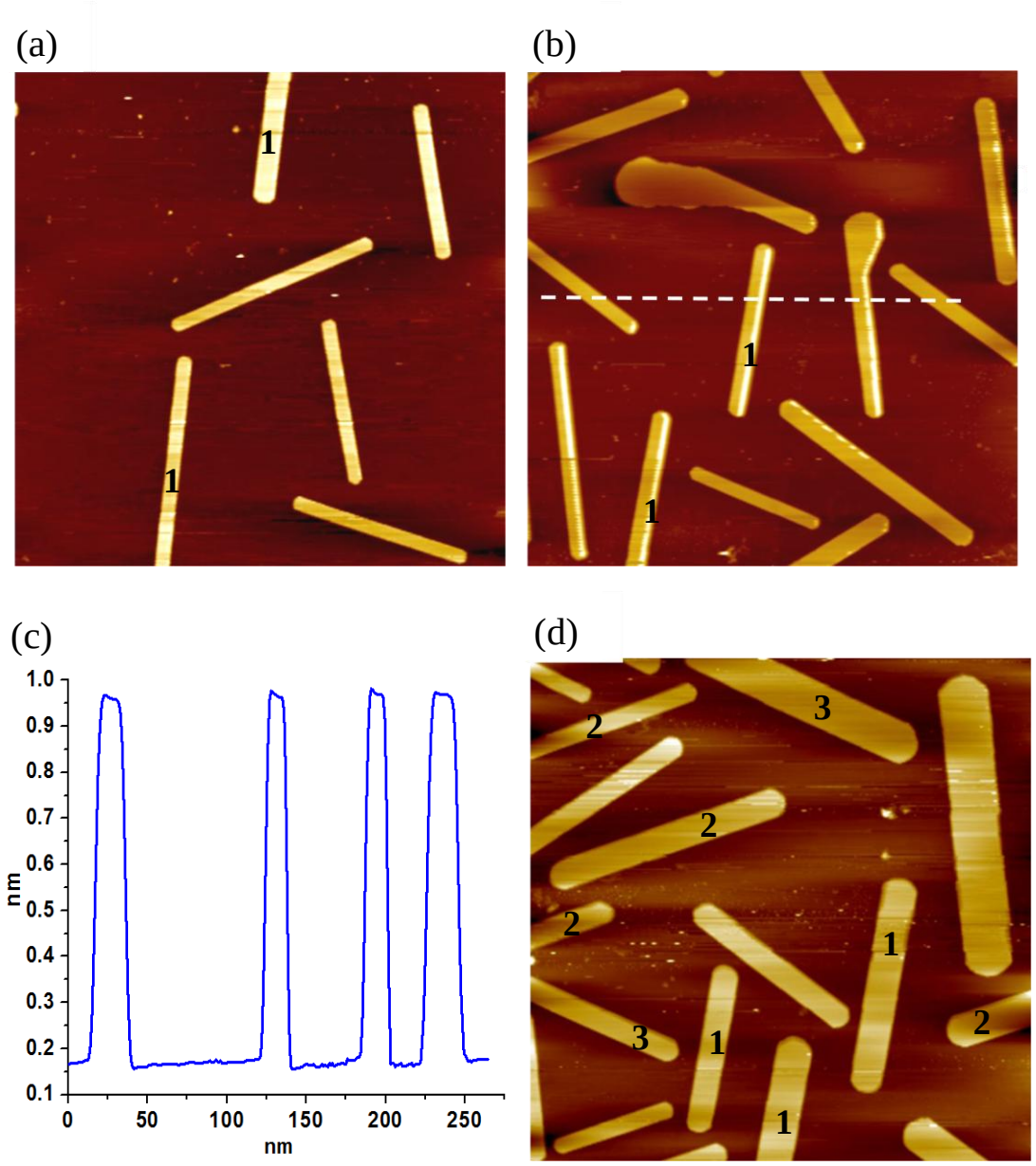

Fig. 3.2 Bismuth nanobelts on MoS_2(0001) at low deposition amount: (a) 0.66 Å, (b) 1.3 Å, (d) 2 Å. Bi flux was 0.12 Å/min. Images sizes of (a), (b) and (d) are 300 nm × 300 nm and all images were taken at 77 K. (c) Height profile corresponding to the white dotted line in (b).

the nanobelts shown in Fig. 3.2 (c) is taken along the dotted line in Fig. 3.2 (b). The height of these nanobelts is 7.9±0.2 Å which is 1.3 Å larger than 6.6 Å, the 1-BL thickness of Bi(110) [11], probably due to a weaker bonding between the puckered Bi(110) nanobelts and the inert substrate than that between the un-puckered layers in bulk Bi. At a Bi deposition amount of 2 Å, some much bigger nanobelts are observed with a width exceeding 35 nm and length more than 170 nm, as the one shown in the upper-right corner of Fig. 3.2 (d). The average width and length increased from 13.5 nm and 115 nm at 1.3-Å deposition to 18 nm and 140 nm, respectively, at 2-Å deposition. As shown in Fig. 3.2 (a) (b) and (d), some of the nanobelts are parallel with each other, such as those labeled with "1". Due to the symmetry of MoS_2(0001), Bi nanobelts also grow in parallel along the equivalent directions as those labeled "2" and "3" shown in Fig. 3.2 (d). But some nanobelts do not grow along any of these three equivalent directions. The growth direction of the nanobelts will be analyzed further later.

With a 3-Å Bi deposition, the nanobelt width increases significantly while the length increase is not much. The number density of nanobelts becomes quite low, apparently due to coalescence of the nanobelts. Some nanobelts join together and form irregular shape as shown at the bottom of Fig. 3.3 (a). Fig. 3.3 (b) and (c) show the formation of sub-wetting layer after 5.3 Å and 6 Å Bi deposition, respectively. At all deposition amounts shown in Fig. 3.2 and Fig. 3.3, the height of nanobelts and irregular-shape islands remains at 7.9 Å, indicating a preferred thickness in this

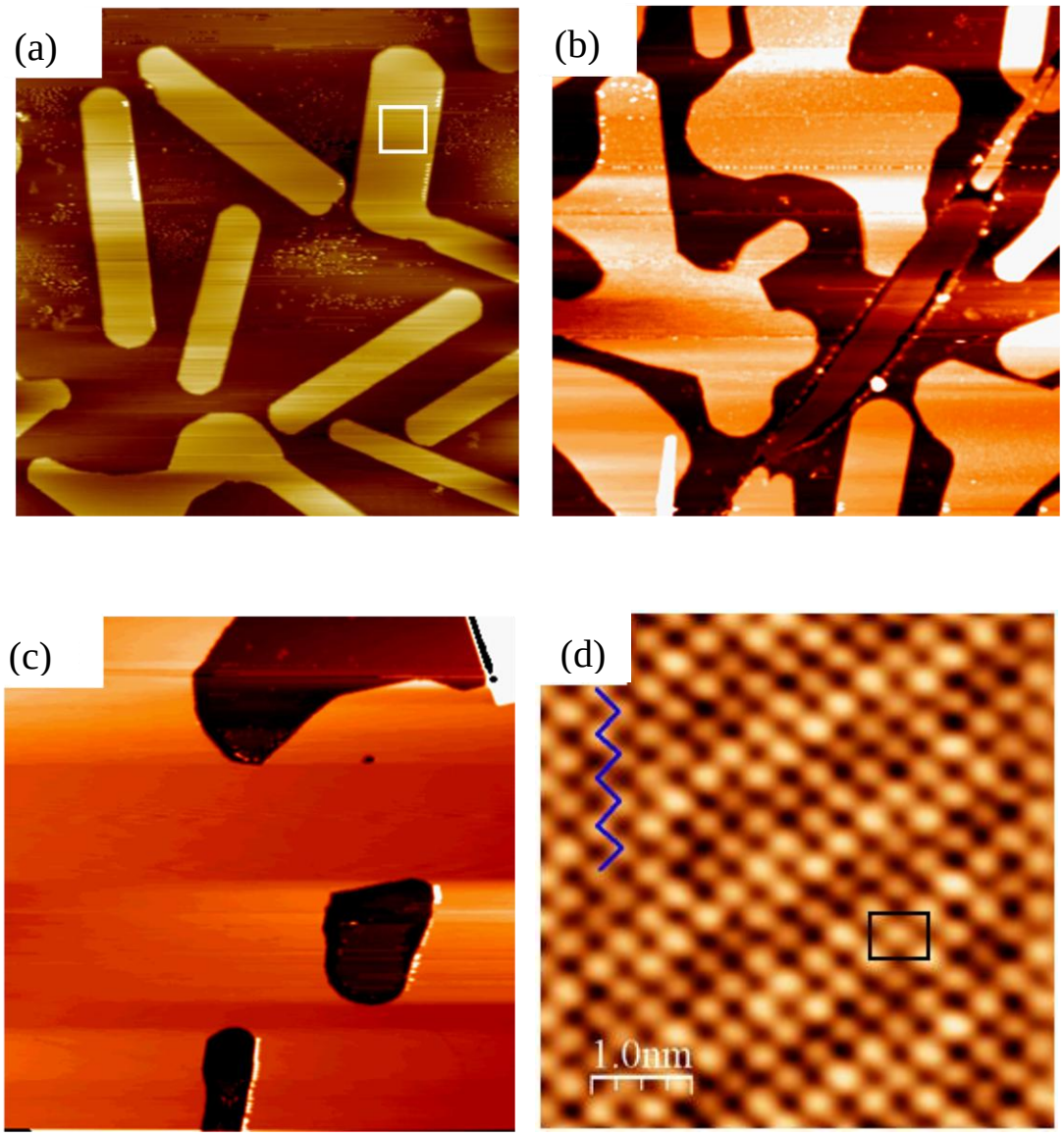

Fig. 3.3 Bismuth nanobelts and sub-wetting layer on MoS_2(0001) at increasing deposition: (a) 3 Å, (b) 5.3 Å and (c) 6 Å. Bi flux was 0.12 Å/min. Images sizes of (a), (b) and (c) are 300 nm × 300 nm and all images were taken at 77 K. (d) Atomic structures of the nanobelt imaged at the square of (a) with the sample biased at -0.1 V.

growth. The atomic structure of the nanobelts was checked at every deposition stage to make sure the surface is Bi(110). Fig. 3.3 (d) shows one imaged in the square area in Fig. 3.3 (a). The atomic resolution image shows that the surface of the nanobelts is a pseudocubic Bi(110) plane and the rectangle in Fig. 3.3 (d) is one unit cell (4.89 Å × 4.51 Å) with the middle atom clearly imaged. The zigzag chain is along the growth direction of the nanobelt. Based on our previous work of Sb nanowires on HOPG [22], we propose that the significant distortion of Bi(110) lattice is due to the anisotropic surface tension of thin Bi(110) nanoribbons along and transverse to the growth direction (zigzag chain). The compression of the lattice (4.51 Å) along the Bi nanoribbons is due to the un-released Laplace pressure [22]. Since the nanoribbons length is far larger than the cross section of edge size, the longitudinal compressive stress is much larger than that of the transverse. Therefore, it is easier for the lattice to expand (4.89 Å) in the transverse direction, leaving the lattice highly compressed along the growth direction. Furthermore, the lattice distortion can also help to explain the LEED pattern of these nanobelts which will be discussed in detail in the later part.

The average width and length of the nanobelts as a function of deposition amount before most of them were coalesced are plotted in Fig. 3.4 (a). Fig. 3.4 (b) displays the length-to-width (L/W) ratio of the nanobelts at four deposition stages shown in Fig. 3.2 (a), (b), (d) and Fig. 3.3 (a). The plot indicates that, with a flux of 0.12 Å/min, the nanobelt L/W ratio peaks at a deposition amount near 1.7 Å, beyond which the width growth and coalescence of nanobelts become dominant.

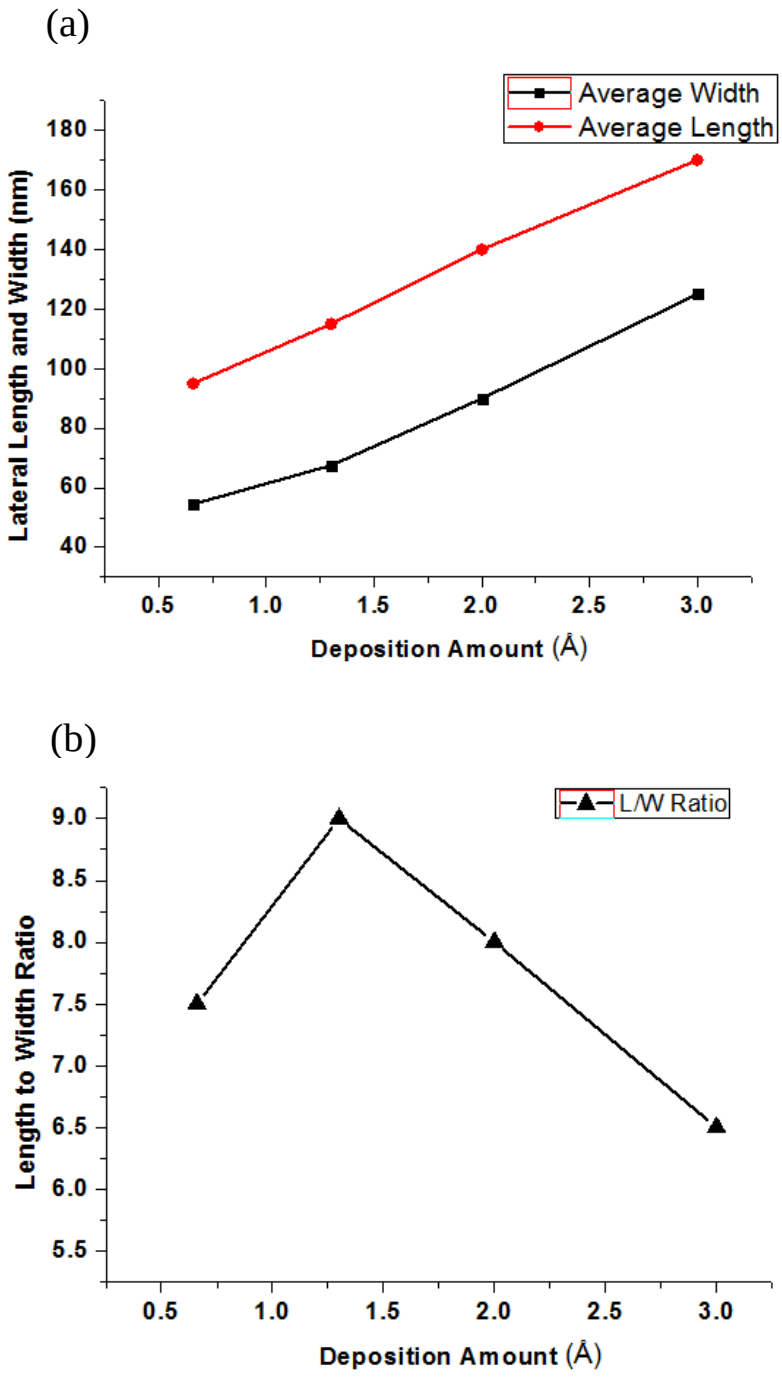

Fig. 3.4 (a) Average width (expanded by 5×) and length, and (b) length-to-width (L/W) ratio at initial deposition stages shown in Fig. 3.2 and Fig. 3.3.

3.3.2 Formation of Nanoribbons at High Flux

Increasing deposition flux to 0.33 Å/min, compared to the nanobelts in Fig. 3.2, Bi forms ribbon-like islands with much smaller L/W ratio as shown in Fig. 3.5 (a) and (b) taken at RT. At 2-Å deposition (Fig. 3.5 (a)), much wider nanoribbons and round-shape islands (L/W close to 1) are observed. Fig. 3.5 (b) shows the sample after 3.3-Å Bi is deposited, the Bi nanoribbons intersect and form irregular islands, while the height remains constant at 8.6±0.2 Å, which is close to the value measured at 77 K. Besides measurement error, the slight difference may reflect a weaker bonding between Bi islands and the substrate at RT than at 77 K. With more Bi deposited, the second-layer Bi belts start to form on top of the first-layer ones before it fully cover the substrate, as shown in Fig. 3.5 (c) and (d) for 4-Å and 6-Å Bi deposition, respectively. The thickness is marked for some islands in Fig. 3.5 (d) in terms of BL of Bi(110). A STM line profile is shown in Fig. 3.5 (e), indicating the thickness is 8.6±0.2 Å for the first-level and 6.8±0.2 Å for the second-level nanobelts. The height increase of 1 BL rather than 1 ML (3.3 Å) indicates the BL stability of the nanobelts which is the same as in the case of Bi deposited on Si(111) surface [11]. Fig. 3.5 (f) displays an image of the sample with 10 Å Bi deposited, and the thickness increase remains in unit of BL of Bi(110).

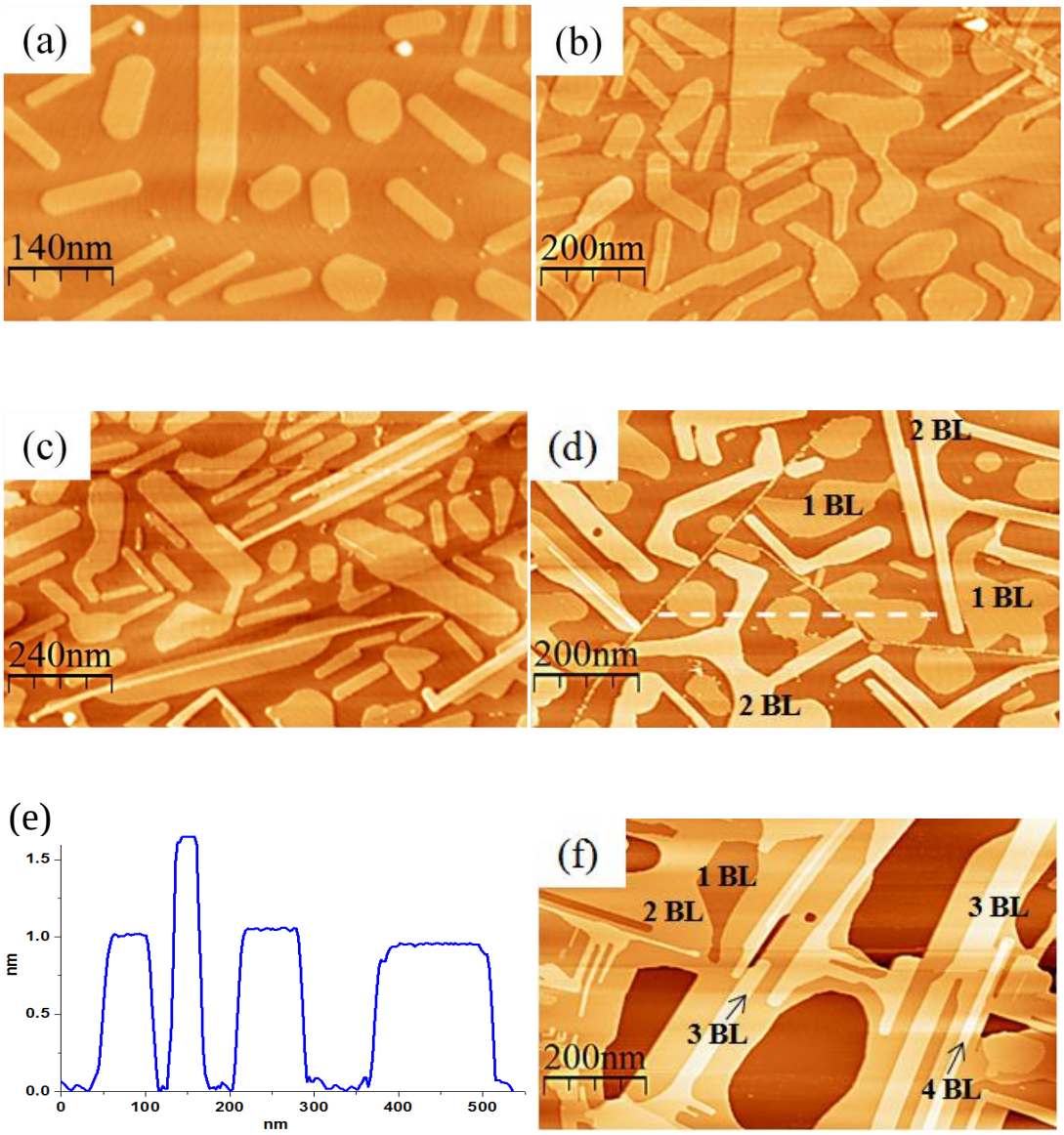

Fig. 3.5 Bi nanoribbons on MoS_2(0001) at deposition of (a) 2 Å, (b) 3.3 Å, (c) 4 Å, (d) 6 Å, and (f) 10 Å. (e) Line profile corresponding to the white dotted line in (d) shows the formation of second layer. (f) Multi-layer Bi nanoribbons with marked thickness. Bi flux was 0.33 Å/min and all the STM images were taken at RT.

3.3.3 Orientation Distribution of Nanobelts

Figure 3.6 (a) shows a SEM image of Bi nanobelts after a Bi deposition amount of 2 Å. We define the zero-degree (0°) angle along the horizontal axis and measure the angle of nanobelts counter-clockwise. After measuring over 500 nanobelts, the orientation distribution of the nanobelts was plotted in Fig. 5(b). Six peaks are paired near 1°, 61° and 121° (indicated by the dash lines), which are assigned as three equivalent axes on MoS_2(0001) substrate. Each basic axis is accompanied by two peaks deviating about 13° from the dash lines. Similar situation was also reported by Patrin *et al.* [13] when they deposited Sb and Bi on GaAs(110), the axes of nanobelts were found tilted by ±7° and ±10°, respectively, from $[1\bar{1}0]$ on the substrate. In our case, the tilting angles are not fixed because of the weak bonding between Bi nanobelts and the inert substrate.

Figure 3.6 (c) shows the LEED pattern (reverse color, electron energy 37 eV) of the sample shown in Fig. 3.6 (a). In addition to the six intense spots corresponding to the MoS_2(0001) substrate, we observe broad spots as the arcs of two rings R_1 and R_2. The number of broad spots is 12 on both rings (marked by red dots for R_2 in Fig. 3.6 (c)). These spots can be grouped into 3 equivalent (nearly) square-type reciprocal lattices rotated by 60° from one another, with the [10] and [01] spots at ring R_2, and the [11] spots at R_1. Notice that the radius of R_2 is slightly less than $1/\sqrt{2}$ times of the radius of R_1, which might be a distortion caused by a non-ideal sample position.

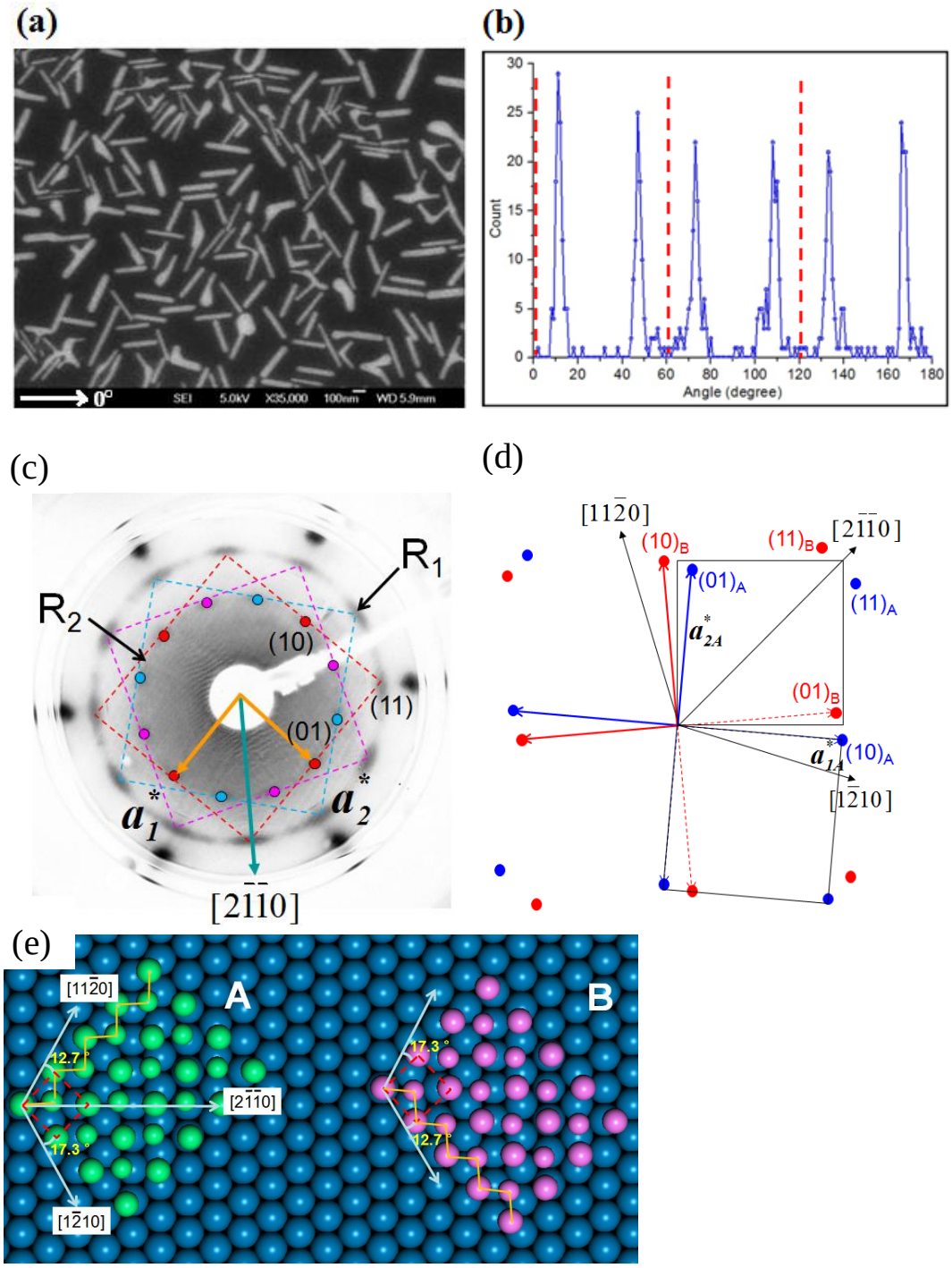

Fig. 3.6 (a) SEM image of Bi nanobelts on MoS_2 with 2 Å Bi deposited (0.12 Å/min). (b) Statistical data of angle distribution of the nanobelts shown in (a). (c) LEED pattern (37 eV) of the sample shown in (a) in reversed color. (d) Alignment model with decomposed two sets of unit cell for one set of arcs in R_1 and R_2. (e) Schematic staking configuration of Bi atoms on MoS_2 shown in the alignment model in (d).

Calibrated with the MoS_2(0001) diffraction spots, from the size of R_1 (which is more reliable than from R_2), we found the real-space primitive diagonal vector length of the square lattice to be 6.60 Å. Considering the nominal unit cell of primitive vectors a_1 = 4.51 Å and a_2 = 4.89 Å on Bi(110), the unit cell diagonal vector length is 6.65 Å. This number agrees well with the measured value.

The above LEED result and its interpretation appear inconsistent with the SEM data plotted in Fig. 3.6 (b) which shows 6 equivalent growth directions of Bi nanobelts, whereas the LEED pattern shows only 3 equivalent growth directions. But the LEED spots from the nanobelts have significant angular and radial broadenings. Considering the compressed unit cell of primitive vectors on Bi(110), and the LEED spots spreading in Fig. 3.6 (c) and the orientation distribution peaks in Fig. 3.6 (b), we propose a lattice orientation relationship between Bi nanobelts and MoS_2(0001) substrate as shown in Fig. 3.6 (d). The top and bottom surfaces of the nanobelts are Bi(110) with a compressed rectangular unit cell size of ~ 4.51 Å × 4.89 Å with the nanobelts growing along $\mathbf{a_1}$, and the diagonal of the cell is aligned with $[2\bar{1}\bar{1}0]$ of MoS_2(0001). In such an alignment, the primitive vectors $\mathbf{a_1}$ and $\mathbf{a_2}$ of Bi(110) are 12.7° and 17.3°, respectively, from other two equivalent $\langle 2\bar{1}\bar{1}0\rangle$ axes of MoS_2(0001). This agrees fairly well with the measured orientation distribution data in Fig. 3.6 (b), which shows that growth directions of Bi nanobelts (i.e., $\mathbf{a_1}$) are ~ 13° off from high-symmetry axes (i.e. $\langle 2\bar{1}\bar{1}0\rangle$) of MoS_2(0001).

Now, let us use this alignment model to explain the LEED pattern in Fig. 3.6 (c). When a Bi nanobelt (called nanobelt A) grows in the direction with the diagonal of its

Bi(110) unit cell aligned with $[2\bar{1}\bar{1}0]$ should generate the set of LEED spots in blue color plotted in Fig. 3.6 (d). The primitive vector $\mathbf{a_{1A}}$ and hence the reciprocal vector $\mathbf{a^*_{1A}}$, which terminates at the $(10)_A$ spot, are at 12.7° from $[1\bar{2}10]$ on $MoS_2(0001)$, whereas the other reciprocal vector $\mathbf{a^*_{2A}}$, which terminates at the $(01)_A$ spot, is at 17.3° from the $[11\bar{2}0]$ axis. The $(11)_A$ spot should be at 4.6° from the $[2\bar{1}\bar{1}0]$ axis. Meanwhile, another Bi nanobelt (called nanobelt B) with the diagonal of its Bi(110) unit cell aligned with $[2\bar{1}\bar{1}0]$ but with the reciprocal vector $\mathbf{a^*_{1B}}$, which terminates at the $(10)_B$ spot, at 12.7° from $[11\bar{2}0]$ of $MoS_2(0001)$ should generate the set of LEED spots in red color plotted in Fig. 5(d). Now, the $(11)_B$ spot is also at 4.6° from the $[2\bar{1}\bar{1}0]$ axis but at the opposite side of the $(11)_A$. Hence, the (11) spots from nanobelt A and B will appear a 9.2° and 4.6° splitting on the direction parallel and perpendicular to the primitive diagonal vector, respectively. Indeed, most spots at ring R_1 in Fig. 3.6 (c) have arc angle of ~ 5° - 9°. Fig. 3.6 (e) shows the two alignment models stacking on the $MoS_2(0001)$ lattice with corresponding vectors and unit cell marked. The zigzag atomic chain is also marked with dashed lines indicating the growth directions of the nanobelts. Since the Bi nanobelts are weakly bonded with the substrate surface, there is a small quantity of nanobelts tilted from the proposed two sets of vectors, giving a broadening to each statistical peak and angular broadening to LEED arcs. Therefore, the LEED pattern is consistent with the statistical data from SEM images as well as our growth alignment model.

3.3.4 Structural Transformation and Formation of Bi(111) Film

With more Bi deposition, new Bi structure appeared as shown in Fig. 3.7 (a) where some triangle-shape islands formed at the bottom-right part of the image. Fig. 3.7 (b) is the line profile along the dash line in Fig. 3.7 (a). Two kinds of steps, Bi(110) BL-step and Bi(111) BL-step (nominal height 3.95 Å, the minimum step height on Bi(111)), are marked on the profile. From the island shape and step heights, we can tell that the Bi island at the upper-left in Fig. 3.7 (a) is (110)-terminated and the bottom-right one has a (111) surface. According to Nagao *et al.*[11] and Yaginuma *et al.* [23], Bi undergoes a structural transformation from Bi(110) to Bi(111) at different critical thickness on various substrates. In our case, the critical thickness is 4 BL of Bi(110). Nagao *et al.* [11] showed that there is an intersection point of cohesion energies of Bi(110)- and Bi(111)-oriented films at a critical thickness. Once the film thickness exceeds the critical value, the lower-energy Bi(111) orientation will dominate. On Si(111), a critical thickness of 4 ML (or 2 BL) of Bi(110) was observed [11]. The larger critical thickness observed on MoS_2(0001) in this work than on Si(111) can be explained in terms of interface effect. The Bi(111) film on Si(111)-7×7 is commensurate while Bi(110) is not, so the interface factor favors Bi(111) film formation. In contrast, on MoS_2(0001), the Bi films of both orientations are in a nearly free-standing state. In fact, our critical thickness agrees quite well with the computational results of Nagao *et al.* [11] based on a comparable surface/interface

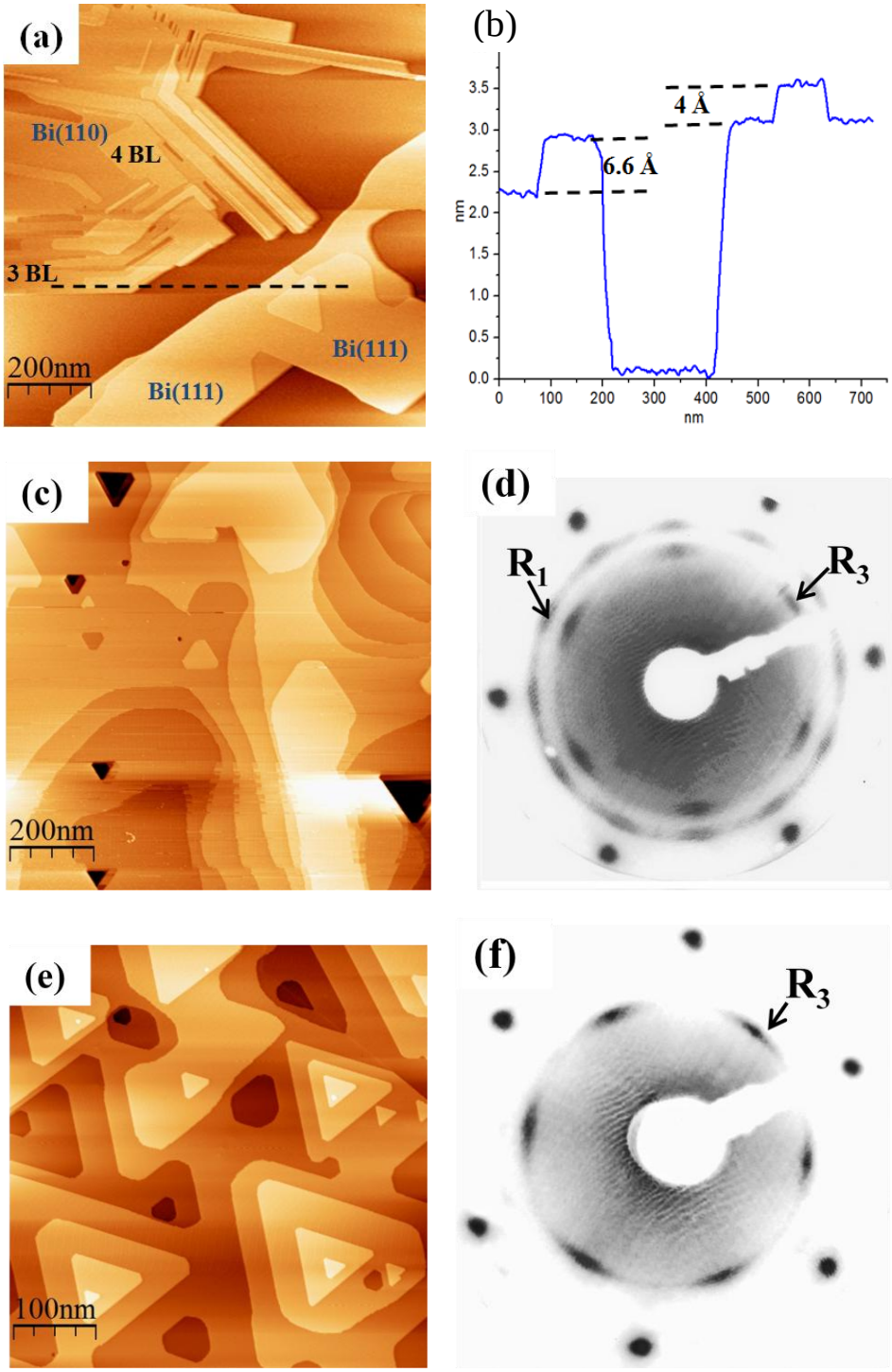

Fig. 3.7 (a) Coexistence of two kind of Bi structures-Bi(110) and Bi(111), with 13 Å Bi deposited. (b) A line profile corresponding to the black dotted line in (a) showing two different kinds of steps. Bi(111) film when (c) 26 Å and (e) 45 Å Bi was deposited. (d) and (f) show the corresponding LEED pattern (37 eV).

condition, which showed a critical thickness of 8 ML (or 4 BL) of Bi(110).

Fig. 3.7 (c) shows that almost the whole surface was covered with Bi after a 26-Å Bi deposition. Atomic resolution STM images show that the top-most surface are all in Bi(111) orientation. Fig. 3.7 (d) displays the corresponding LEED pattern in which a new ring R_3, can be observed. The six arc-shape spots on R_3 indicate a hexagonal symmetry, and the radius of R_3 corresponds to a real-space period of 4.54 Å, exactly the lattice constant of Bi(111) surface. The R_1 ring remains visible, indicating that some Bi(110)-oriented components still exist. After 45-Å Bi is deposited, a well-ordered Bi(111) film is obtained, as illustrated by the STM image in Fig. 3.7 (e) and the corresponding LEED pattern in Fig. 3.7 (f) in which only the R_3 with six intense arcs is generated by the Bi film. The R_3 spots in both Fig. 3.7 (d) and 3.7 (f) show that the orientation of Bi(111) hexagonal lattice is rotated 30 ° from that of the substrate.

3. 4 STS Study of Bi LDOS on HOPG

The growth morpholgy of Bi on HOPG has been extensively studied [15, 18, 19], while the electronic structures of Bi thin film investigated by STS has been seldom reported [24]. Fig. 3.8 shows the morphology of Bi nanostructures on HOPG with increasing deposition amount. Similar to the morphology on MoS_2(0001) deposited at higher flux, Bi form multi-layer branched linear structures on HOPG before the

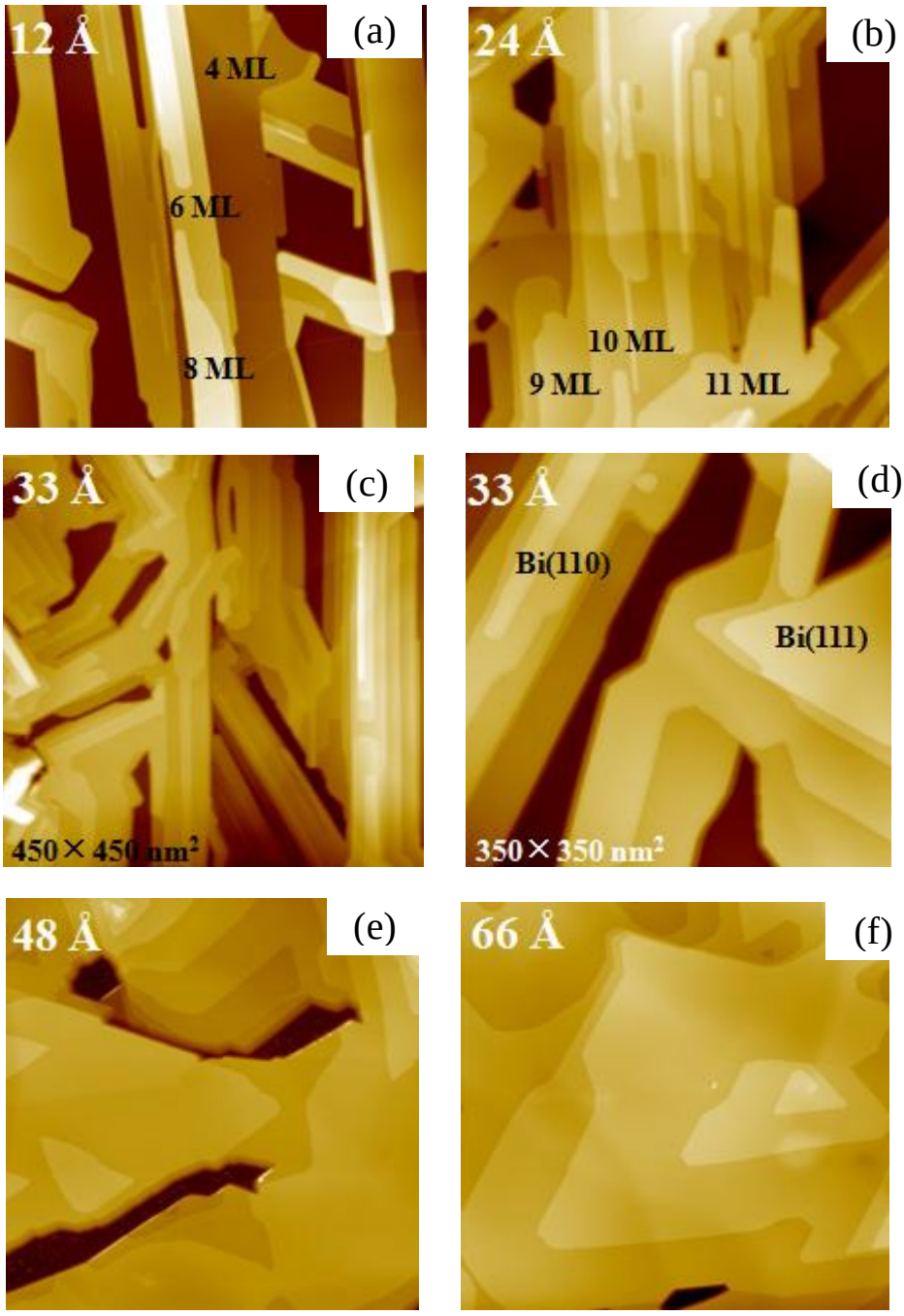

Fig. 3.8 STM images of Bi morphology on HOPG at different deposition amount as indicated at the upper-left corner of each image. (a)-(c) Branched multi-layer Bi(110) nanostructures with thickness labeled. (d) An area with co-existence of Bi(110) and Bi(111) structures. (e), (f) Bi(111) films. The image sizes are 500 × 500 nm^2 except (c) and (d), where the sizes are marked at the bottom-left corner.

structural transformation, as shown in Fig. 3.8 (a)-(c). The layer thickness, defined by the unit of monolayer of Bi(110), is marked on the corresponding Bi nanoribbons. Fig. 3.8 (d) displays one area where two kinds of Bi structures, Bi(110) and Bi(111), are observed, showing the phase transition to Bi(111) occurs. Based on our experiment, the phase transition critical thickness from Bi(110) to Bi(111) is 12 ML of Bi(110) at RT. This critical height is larger than that on MoS_2, which indicates the weaker interfacial effect between Bi and HOPG surface. Similar increase of critical thickness was also observed on Bi/$\sqrt{3} \times \sqrt{3}$-Bi/Si(111) surface [23].

Fig. 3.8 (e) shows the morphology of Bi(111) s layer at 48 Å Bi deposition. With more deposition, almost all the HOPG surface is covered with Bi(111) film with large terrace, as shown in Fig. 3.8 (f).

Fig. 3.9 displays the dI/dV spectra obtained on different height of Bi(110) stripes, showing thickness dependent LDOS near the Fermi level. On the area with thickness of 2 ML and 4 ML, as shown at the bottom of Fig. 3.9, the spectra reveal an evident gap on each spectrum, indicating that the surfaces of 2 ML and 4 ML are semiconducting. 0.45 eV and 0.76 eV gap was measured, respectively. The reason for the gap can be understood as that thin Bi(110) has the puckered relaxation from the bulk-like Bi(110) to black phosphorus-like Bi(110) [11] which open a gap near Fermi level. In this puckering model, two adjacent Bi(110) ML bond together, and the out-of-plane dangling bonds can be eliminated, which reduces the p_z obital in the energy band [25]. The larger gap observed on 4 ML Bi(110) than on the 2 ML probably can be explained as the double bi-layer Bi(110) have tiny in-plane movement to form

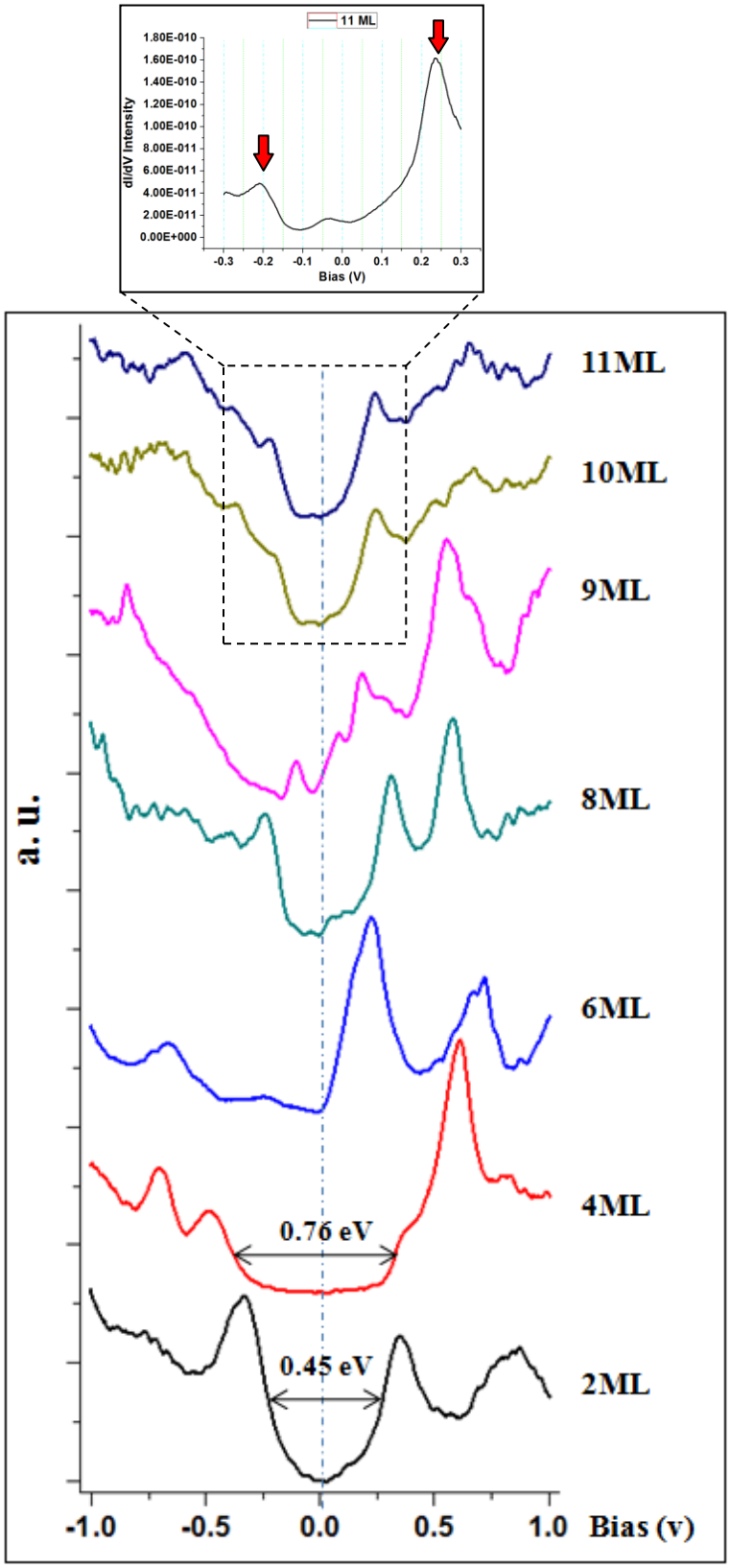

Fig. 3.9 STS of Bi(110) nanostructures at different layer thickness. The zoom-in spectrum for 11 ML is shown, with two red arrows indicating two surface states.

inter-bi-layer bond and couple into stable double bi-layer structure, which may show an even larger gap than single bi-layer.

On the 6-ML Bi(110) stripe, the dI/dV spectrum shows a strong surface state near the Fermi level. This feature is rather similar with the DOS on 6-ML Bi(110) thin film calculated by Koroteev *et. al.* [25], in which the layer with a thickness equal to and larger than 6 ML is considered to be bulk-like. This agreement also indicates that on HOPG, the Bi nanostructures are in a nearly free-standing environment as that assumed in the calculations. By STM investigation, we also observed the bulk-like growth behavior. At large deposition amount (>12-Å Bi deposition) , 7-ML Bi(110) can be found occasionally, and at even larger deposition (>18-Å Bi deposition), the chance to find 9 ML and 11 ML Bi(110) is the same with that of even layers. This growth behavior strongly supports the calculation results [25] and indicates that beyond 6-ML, the puckered relaxation is too weak to form even-layer-stable structures, and the thickness increase becomes single ML of Bi(110), showing bulk-like growth model. Bulk-like Bi(110) surface is considered to be a metallic surface because of the dangling bond pointing out of the plane. In the STS curves shown in Fig. 3.9, the bulk-like metallic feature can be seen in 8 ML and 9 ML spectra near the Fermi level. However, because the intensity of the surface state of thicker layer (10 ML and 11 ML) is too strong, the metallic feature on 10 ML and 11 ML is hard to be seen. The zoom-in spectrum is shown at the top of Fig. 3.9, with two red arrows indicating two surface states. The bulk-like metallic feature near the Fermi level can be resolved clearly. The position of these two surface states at -200 mV and +230 mV

agree fairly well with the major surface states investigated by angle resolved photoelectron spectroscopy (ARPES) experiment on cleaved bulk Bi(110) crystal [26] and first-principle calculation [27], indicating our thicker Bi(110) films (≥ 10 ML) are bulk-like. All the spectra of thickness larger than 6 ML have none-zero DOS at the Fermi level, which suggest the surfaces becoming metallic.

Fig. 3.10 displays the dI/dV mapping obtained at different bias voltage of adjacent Bi(110) layers. Topologically, the layers have increasing height from 2 ML to 8 ML, as shown in the inset line profile. However, at different energy cross-section (corresponding to different bias), the electronic states exhibit evidently different features. For example, at +500 mV, 4 ML Bi(110) have larger density of electronic states than any other layers which have higher topological profile. The dI/dV mapping agrees well with the STS curves shown in Fig. 3.9.

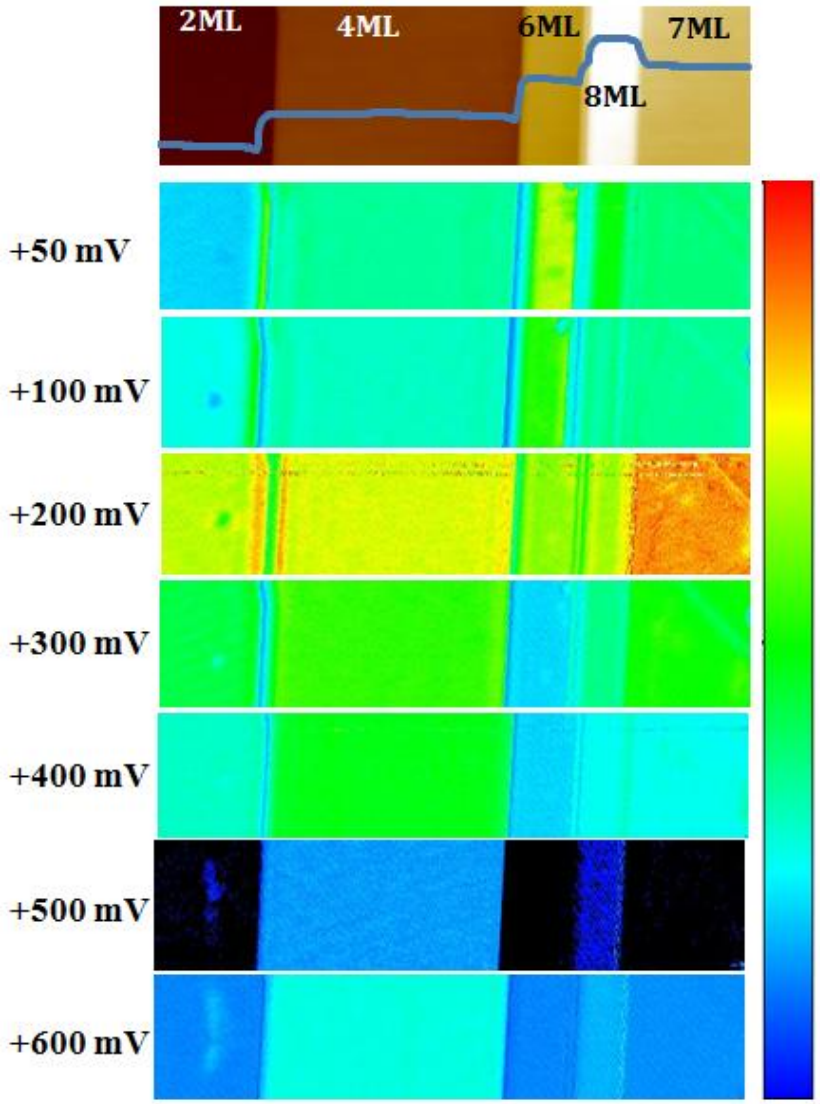

Fig. 3.10 dI/dV mapping of adjacent 2 ML, 4 ML, 6 ML, 8 ML and 7 ML Bi(110) stripes at unoccupied state with different bias voltage.

3.5 Conclusions

When Bi is deposited on MoS_2(0001), two kinds of nanostructures, namely nanobelts and thin film, were observed with STM, SEM and LEED. Bi nanobelts in (110) orientation can form at small deposition amount. SEM images and LEED patterns reveal that the growth directions of Bi nanobelts deviate by ~ 13 ° from the $\langle 11\bar{2}0 \rangle$ axes of the substrate. When the thickness of Bi nanobelts exceeds the critical thickness of 4 BL of Bi(110), Bi(111) islands form at the top layers. With further increase in deposition, a well ordered Bi(111) forms. This critical thickness value indicates that the bonding of both types of Bi structures with MoS_2(0001) is rather weak. Compared to Bi deposition on HOPG, the single-crystal MoS_2 substrate allowed us reveal the effect of substrate symmetry on the growth orientation of Bi nanobelts. Our STS experiment illustrates the thickness dependent LDOS of Bi(110) layer at different layer thickness. This result extends the understanding of electronic structures of Bi(110) thin-film and may lead to interesting application potential of Bi in electronic nanodevices.

References

[1] C. R. Ast and H. Höchst, Physical review letters **87**, 177602 (2001).

[2] T. Hirahara, T. Nagao, I. Matsuda, G. Bihlmayer, E. V. Chulkov, Y. M. Koroteev, P. M. Echenique, M. Saito, and S. Hasegawa, Physical review letters **97**, 146803 (2006).

[3] C. A. Hoffman, J. R. Meyer, F. J. Bartoli, A. Divenere, X. J. Yi, C. L. Hou, H. C. Wang, J. B. Ketterson, and G. K. Wong, Phys. Rev. B **48**, 11431 (1993).

[4] Z. B. Zhang, X. Z. Sun, M. S. Dresselhaus, J. Y. Ying, and J. Heremans, Phys. Rev. B **61**, 4850 (2000).

[5] T. E. Huber, A. Nikolaeva, D. Gitsu, L. Konopko, C. A. Foss, and M. J. Graf, Appl. Phys. Lett. **84**, 1326 (2004).

[6] S. L. Cho, Y. Kim, A. J. Freeman, G. K. L. Wong, J. B. Ketterson, L. J. Olafsen, I. Vurgaftman, J. R. Meyer, and C. A. Hoffman, Appl. Phys. Lett. **79**, 3651 (2001).

[7] Y. M. Lin, X. Z. Sun, and M. S. Dresselhaus, Phys. Rev. B **62**, 4610 (2000).

[8] S. Murakami, Phys. Rev. Lett. **97**, 236805 (2006).

[9] C. R. Ast and H. Hochst, Phys. Rev. B **67** (2003).

[10] S. S. K. X.-S. Wang, X.-J. Chu, H.-L Zhang, Z.-J. Yan, W.-D. Xiao, Handbook of Nanoscience and Nanotechnology pp. 572-597 (2010).

[11] T. Nagao, J. T. Sadowski, M. Saito, S. Yaginuma, Y. Fujikawa, T. Kogure, T. Ohno, Y. Hasegawa, S. Hasegawa, T. Sakurai, Phys. Rev. Lett. **93**, 105501 (2004).

[12] D. L. Partin, J. Heremans, D. T. Morelli, C. M. Thrush, C. H. Olk, and T. A. Perry, Phys. Rev. B **38**, 3818 (1988).

[13] J. C. Patrin, Y. Z. Li, and J. H. Weaver, Phys. Rev. B **46**, 10221 (1992).

[14] H. Wang, J. Jing, R. R. Mallik, H. T. Chu, and P. N. Henriksen, Journal of Crystal Growth **130**, 571 (1993).

[15] S. A. Scott, M. V. Kral, and S. A. Brown, Surf. Sci. **587**, 175 (2005).

[16] S. Yaginuma, T. Nagao, J. T. Sadowski, A. Pucci, Y. Fujikawa, and T. Sakurai, Surf. Sci. **547**, L877 (2003).

[17] C. Bobisch, A. Bannani, M. Matena, and R. Moller, Nanotechnology **18**, 055606 (2007).

[18] S. A. Scott, M. V. Kral, and S. A. Brown, Phys. Rev. B **73**, 205424 (2006).

[19] S. A. Scott, M. V. Kral, and S. A. Brown, Phys. Rev. B **72**, 205423 (2005).

[20] J. Petersen, R. Strohmaier, B. Gompf, and W. Eisenmenger, Surf. Sci. **389**, 329 (1997).

[21] D. E. Hooks, T. Fritz, and M. D. Ward, Advanced Materials **13**, 227 (2001).

[22] X. S. Wang, S. S. Kushvaha, Z. Yan, and W. Xiao, Appl. Phys. Lett. **88** (2006).

[23] S. Yaginuma, T. Nagao, J. T. Sadowski, M. Saito, K. Nagaoka, Y. Fujikawa, T. Sakurai, and T. Nakayama, Surf. Sci. **601**, 3593 (2007).

[24] S. Yaginuma, K. Nagaoka, T. Nagao, G. Bihlmayer, Y. M. Koroteev, E. V. Chulkov, and T. Nakayama, J. Phys, Soc. Japan **77**, 014701 (2008).

[25] Y. M. Koroteev, G. Bihlmayer, E. V. Chulkov, and S. Blügel, Phys. Rev. B **77**, 045428 (2008).

[26] P. Hofmann Prog. Surf. Sci. **81**, 191 (2006).

[27] Y. Liu, R. E. Allen, Phys. Rev. B **52**, 1566 (1995).

Chapter 4 Growth of Bismuth Nanowires with Large L/W Ratio

4.1 Introduction

Linear or one-dimensional (1D) nanostructures, including nanowires (NWs), nanotubes, nanorods and nanoribbons, have attracted much attention because of their superior properties and unique applications in mesoscopic physics and fabrication of nanoscale devices [1-3]. Due to reduced dimensionality, the physical properties of 1D nanostructures result in novel and/or superior functionalities in electronic, optoelectronic, chemical, magnetic and spintronic applications [4-6]. For example, metal-oxide NWs can function as sensitive and selective chemical or biological sensors, which could potentially be massively multiplexed in devices of small size [7]. In particular, Bi 1D nanostructures are expected to exhibit more interesting physical properties, such as surface superconductivity [8], extremely large magnetoresistance [9], and high thermoelectric efficiency [10].

Now, 1D nanostructures of various metallic, semi-metallic, semiconducting and insulating materials can be produced in different procedures. Among these procedures, the traditional lithography techniques, such as electron-beam (E-beam) or focused-ion-beam (FIB) writing [11], proximal-probe patterning [12, 13], and X-ray or extreme-UV lithography [14, 15], can fabricate 1D nanostructure productively. However, these processes are limited in minimum feature size due to the diffraction effect, especially when the UV light is used [16]. In contrast, unconventional methods based on chemical synthesis or self-assembly have provided an alternative and intriguing strategy for generating 1D nanostructures in terms of material diversity and

the potential for mass production [17]. For example, the vapor-liquid-solid (VLS) method [18] has been widely used to grow semiconductor and oxide NWs [19, 20]. Fig. 4.1 (a) shows a series of examples of InP NWs fabricated by using VLS method [21]. Moreover, a great number of linear nanostructures have been synthesized in solution-based self-assembly processes [22]. A good example was demonstrated by Gates *et al*., who have successfully synthesized t-Se NWs with uniform shape using such method [23]. In some solution-based NW and nanorods synthesis processes, surfactants are utilized to preferentially cap the side surfaces so that highly anisotropic growth takes place [24]. A TEM image is shown in Fig. 4.1 (b) as an example for growth of CdSe nanorods by using this capping method [24]. In addition, intensive efforts have been devoted to the fabrication of 1D Bi nanostructures with controlled size and crystalline structures by taking advantage of templates [25]. For example, branches of Bi NWs have been synthesized by using anodic alumina membranes (AAM) as a template [25].

In this chapter, I demonstrate a new method of growing 1D Bi NWs using a molecular layer 3,4,5,10-perylene tetracarboxylic dianhydride (PTCDA) on MoS_2(0001) as a template. *In-situ* STM images show that Bi first grow into NWs with single atomic layer thickness and aligned orientation. With more Bi deposited, the ultra-thin NWs develop into NWs in Bi(110) orientation with 4- or 6-layer thickness. The NWs grow along three directions of the ordered molecular layer. Due to the side wall passivation by PTCDA, the growth of width of NWs is greatly depressed and hence NWs with large length to width ratio (LWR) can be obtained.

(a)

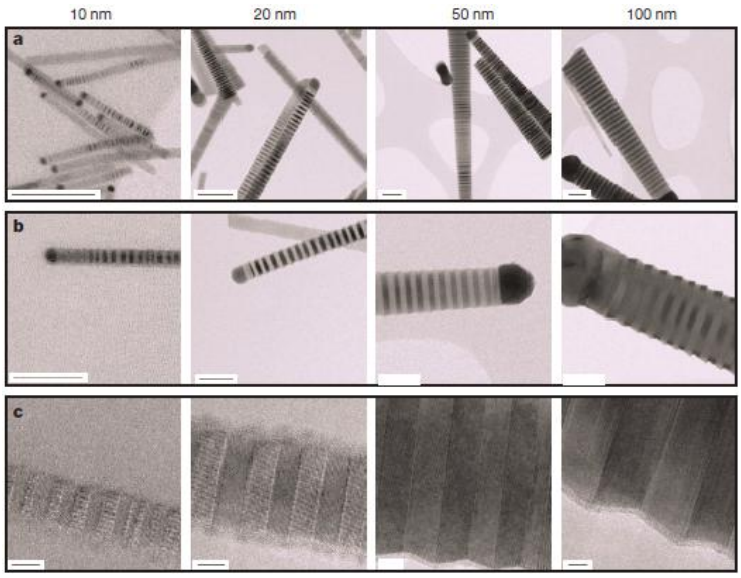

(b)

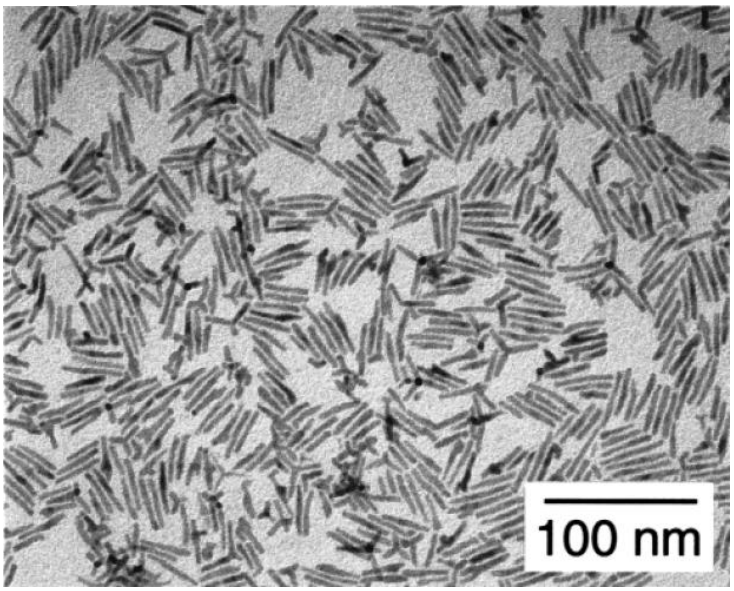

Fig. 4.1 (a) Series of TEM images showing the InP superlattice NWs grown by VLS method (reprinted from Ref. [21] by permission of the Nature Publishing Group); and (b) CdSe nanorods fabricated by using capping method (reprinted from Ref. [24] by permission of the American Chemical Society).

4.2 Experimental Method

The experiments were carried out in our Omicron UHV RT-STM system (base pressure less than 5×10^{-11} Torr) equipped with an AES and LEED [26]. Clean MoS_2(0001) substrate was prepared by cleaving in air and then quickly transferred into UHV system, followed by an overnight degassing at 400 ℃. PTCDA molecules (purified by Creaphys, Germany) [27] were deposited firstly onto the clean substrate at RT from a Ta crucible, followed by annealing at 380K for 30 minutes to form flat, uniform and in-plane-compact overlayer. At the first part of the experiment, only half monolayer PTCDA was deposited with half of the substrate surface uncovered. The aim is to compare the difference of growth behavior of Bi on bare MoS_2(0001) and PTCDA/MoS_2(0001). In the part of investigating the orientation distribution of Bi NWs, we used full-monolayer PTCDA overlayer on MoS_2(0001).

After molecular layer deposition, high purity (99.999%) Bi was evaporated from a Ta crucible and deposited onto the PTCDA/MoS_2 surface subsequently at RT. Before deposition, Bi source was degassed at appropriate temperatures for a few hours in order to remove contamination. The flux was calibrated using AES and STM. All the atomic scale images were carefully calibrated to eliminate scanner drift.

4.3 Preparation of PTCDA Overlayer

PTCDA is a model molecule within its class of organic semiconductors. Fig. 4.2 (a) shows the structural formula of PTCDA. It belongs to a class of intensive dye molecules suitable for optoelectronic applications [28]. The planar stacking provides good prospects for molecular ordering on flat surfaces. Thus it is good candidate to act as a surfactant layer. Fig. 4.2 (b) displays the STM image of a full monolayer of PTCDA on MoS_2. Fig. 4.2 (c) and (d) show the occupied-state STM images of the molecular configuration in detail at different bias voltages. One unit cell in real space is marked in the image. The STM images show the formation of well-ordered PTCDA monolayer with in-plane herringbone arrangement due to the multiple intermolecular hydrogen bonding. Fig. 4.2 (e) is the LEED pattern taken at 17.6 eV showing that the molecular film has good crystalline properties with three equivalent domains. The pattern is similar with that of 0.5 ML PTCDA on Au(111) [29], showing six equivalent domains. One set of unit cell of PTCDA is marked in the LEED pattern, corresponding to the real space unit-cell size of 12 Å × 20 Å.

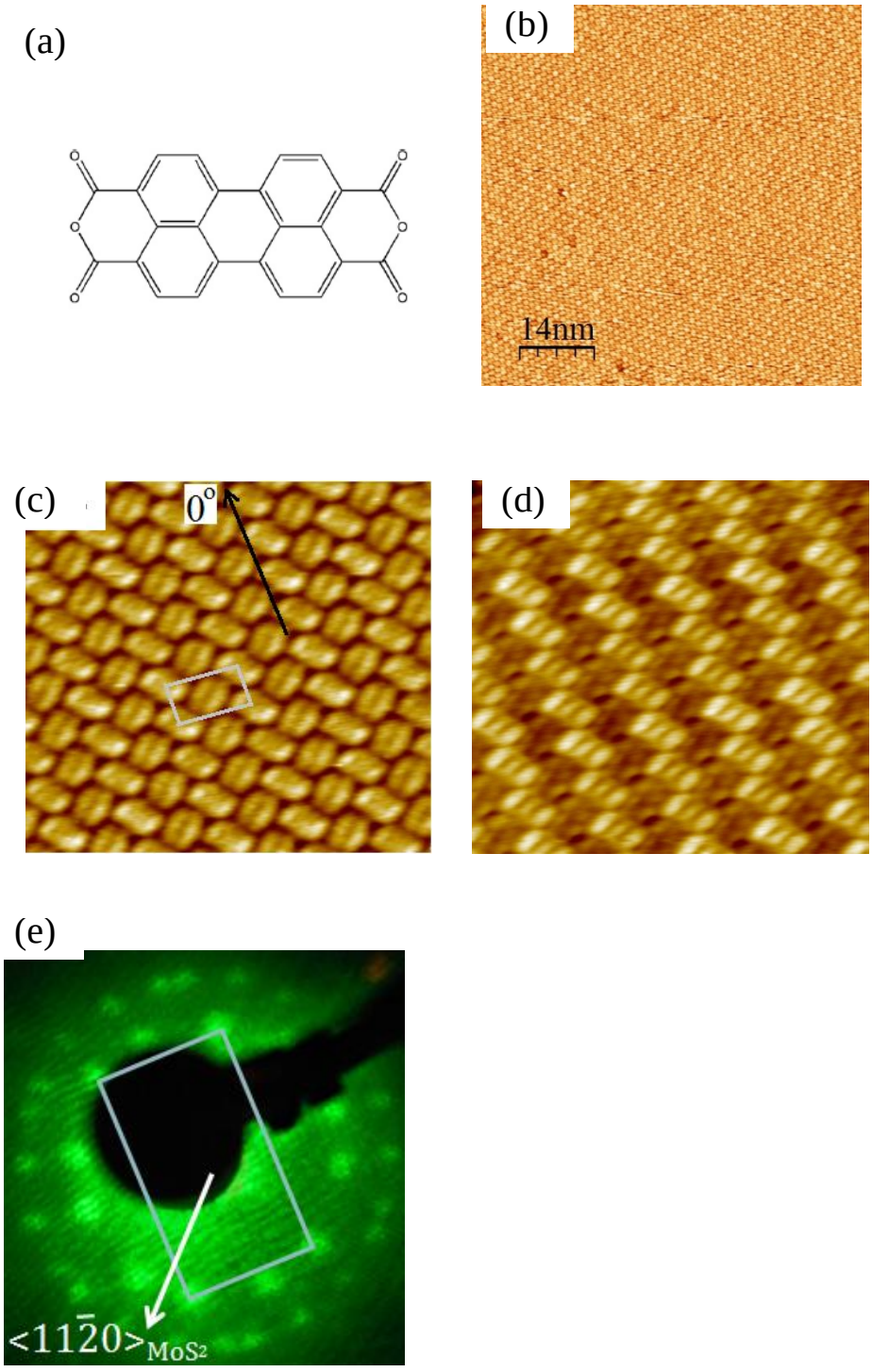

Fig. 4.2 (a) Structural formula of PTCDA. (b) 70 nm × 70 nm STM image PTCDA monolayer on MoS_2. 9 nm × 10 nm occupied state STM image of PTCDA at sample bias of (c) -1.5V and (d) -0.8V. (e) LEED pattern (17.6 eV) of PTCDA monolayer. (f) Schematic model of PTCDA stacking on MoS_2(0001).

4.4 Results and Discussion

4.4.1 Formation of Bi NWs with Large L/W ratio on PTCDA/MoS_2

To compare the different morphology of Bi nanostructures with and without PTCDA, 0.5 ML PTCDA was deposited on the MoS_2 surface and leave half the substrate uncovered before Bi deposition. Fig. 4.3 (a) shows the sample of 0.5 Å Bi deposited at the initial stage. The left part is an area without PTCDA while the right part corresponds to the molecules covered area. It is obvious that Bi hardly nucleate on the PTCDA covered area because of its well-ordered in-plan bonding. While on the bare MoS_2 surface, Bi nanoribbons with height of 2 Bi(110) ML formed which is the same as described in ***Chapter 3***. Fig. 4.3 (b) displays a zoom-in image of the PTCDA molecular overlayer with a visible boundary. Besides the small Bi clusters at the right part of this image, short linear Bi NWs appears at the edge of molecular film, shown in the lower-left part of Fig. 4.3 (b).

As shown in Fig. 4.3 (c), with 1 Å Bi deposited, aligned ultra-thin Bi NWs with much longer length appear in the PTCDA covered area. These aligned NWs are longer than 100 nm but only have a width of 2.35±0.2 nm which is the width of two PTCDA molecules in the herringbone bonding (i.e., 0.92 nm + 1.42 nm, as used in [30]). On the other hand, the two much broader nanoribbons at the upper-left part are neither parallel to each other nor to the ultra-thin Bi NWs. This difference illustrates that the orientation of Bi NWs is strongly modified by the PTCDA overlayer and

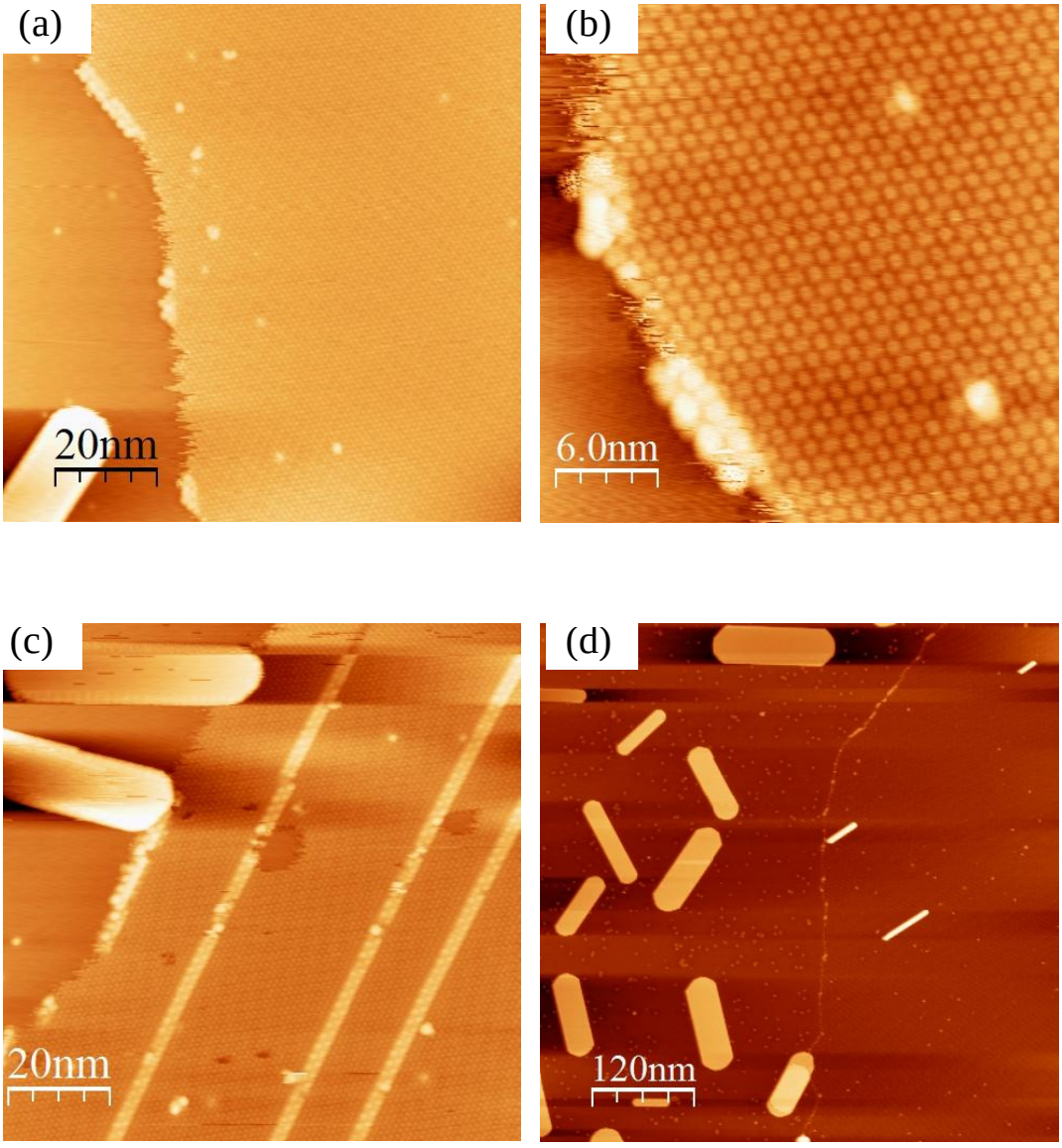

Fig. 4.3 STM image of (a) Initial morphological difference with 0.5 Å Bi deposited. (b) Zoom-in view of small amount of linear Bi nanostructures nucleated at the boundary of PTCDA overlayer. (c) Formation of aligned ultra-thin Bi NWs with 1 Å Bi deposited. (d) Formation of aligned shorter Bi nanorods after 2 Å Bi deposited.

will be discussed in detail in section 4.4.2. After 2 Å Bi deposition, as displayed in Fig. 4.3 (d), the ultra-thin Bi NWs changed into thicker NWs (right part). However, the length of these newly formed NWs (40~60 nm) becomes shorter than the ultra-thin NWs formed at the initial stage. The width of these new NWs is around 5 nm. The reason of this change will also be discussed in section 4.4.2.

Fig. 4.4 (a) shows a small area STM image with three Bi NWs in parallel, obtained after 3 Å Bi was deposited. The length of the NWs increased except the newly formed shortest one, while the width changed little, which indicates that the growth of Bi on PTCDA/MoS_2 surface is much more anisotropic than that on a bare MoS_2 surface. When the deposition amount is increased to 4 Å, as shown in Fig. 4.4 (b), NWs with new orientations appear. It is evident that most NWs are in three orientations. The reason will be discussed later in section 4.4.3. Some of the NWs are longer than 200 nm but their width remains under 8 nm. The length-to-width (L/W) ratio for the long NWs is much larger than that of the nanoribbons at the upper part of the image (also described in Chapter 3). The boundary of PTCDA molecular layer is marked by a dash line. Fig. 4.4 (c) shows the area full of large L/W ratio NWs at the same Bi deposition amount as Fig. 4.4 (b). The maximal L/W ratio is larger than 80.

With 10 Å Bi deposited, as shown in Fig. 4.4 (d) which is an area fully covered with PTCDA molecules, most of the NWs are intersected and 2-D islands appear. It is obvious that the intersection parts of the NWs provide the nucleation sites for newly-arriving Bi atoms to form these 2-D islands. Two examples are marked with dash-line circles in Fig. 4.4 (d). Moreover, due to the growth anisotropy properties of Bi(110)

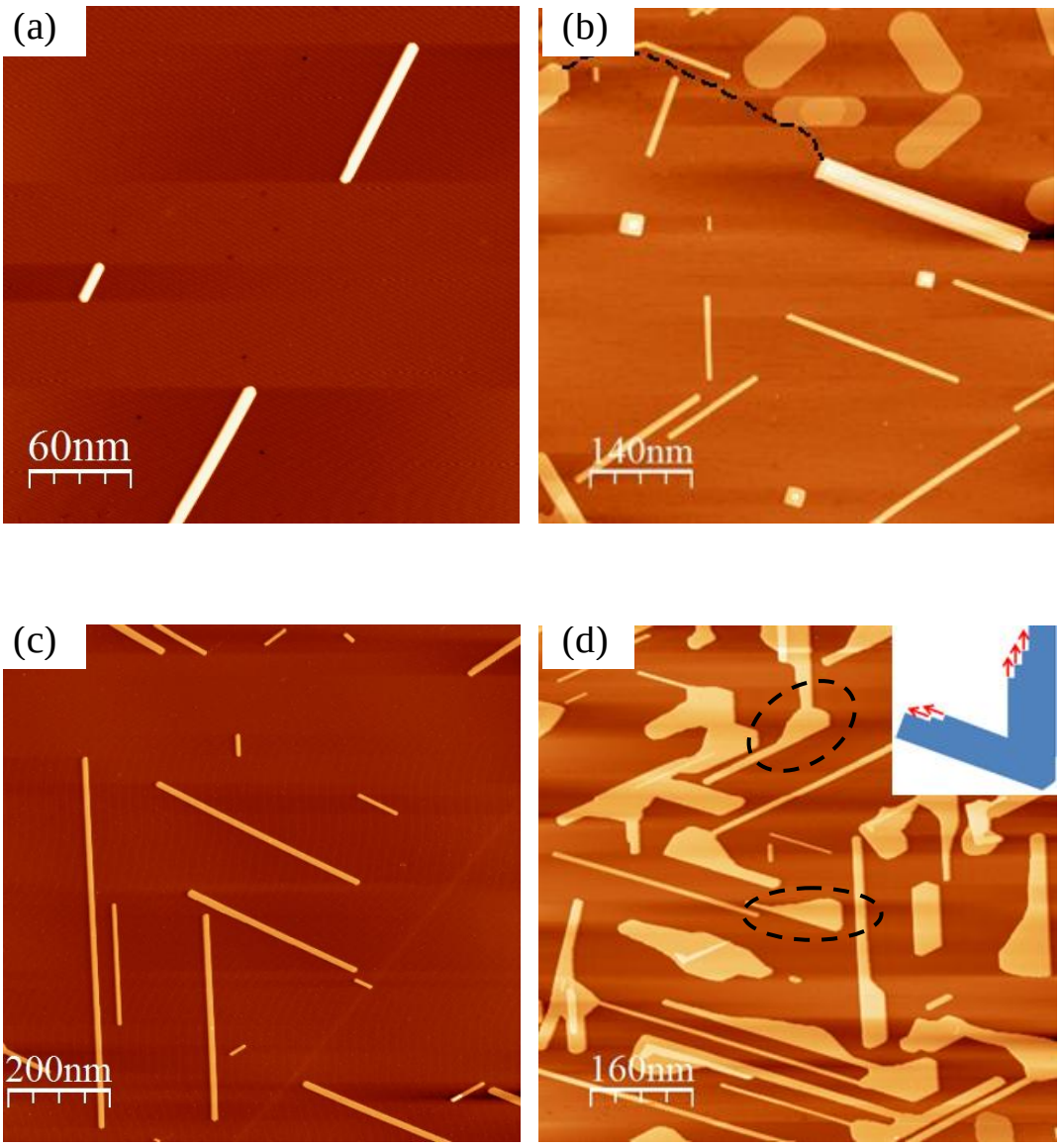

Fig. 4.4 STM images of (a) Aligned thicker NWs with 3 Å Bi deposited. (b) Large L/W ratio NWs with other orientations appear at 4 Å Bi deposition. (c) Large area full of NWs in which some of them have extreme large L/W ratio. (d) Formation of 2-D islands with 10 Å Bi deposited and inset shows the growth model of broader ribbon-like Bi nanostructures.

surface, the junctions of NWs can initiate new atomic lines adjacent to the existing Bi NWs and thus form broader ribbon-like nanostructures. The inset of Fig. 4.4 (d) shows the schematic drawing of this model.

4.4.2 Model for Template Growth of Bi NWs with Large L/W Ratio

Fig. 4.5 (a) displays a high-resolution STM image showing the morphology of an ultra-thin Bi NW at the initial stage in detail. The red color indicates a higher profile while the blue color represents the lower profile. The image indicates that all the PTCDA molecules are still in the herringbone arrangement including the higher ones above the Bi NW. A 3-D view of part of this NW is shown in the inset of Fig. 4.5 (a), illustrating that the molecules has been lifted. Fig. 4.5 (b) displays the schematic model of the anisotropic growth of Bi(110) NW along the zigzag direction. Because the side wall of the NW do not have in-plane unsaturated bond, the newly arriving Bi atoms move fast to the two ends of the zigzag chains and saturate the dangling bonds. Furthermore, the PTCDA molecules also can direct the NW to grow along its herringbone direction which is more stable than other directions.

A STM line profile across the Bi NW (indicated by a white dotted line in Fig. 4.5 (a)) is shown in Fig. 4.5 (c), indicating that the PTCDA on top of Bi NW is only 1.2 ± 0.2 Å higher than the molecules on the substrate (thickness of monolayer PTCDA on MoS_2 is considered to be 2.5 Å). This height difference suggests that the Bi NW underneath the PTCDA is only one Bi(110) atomic layer thick. As described in

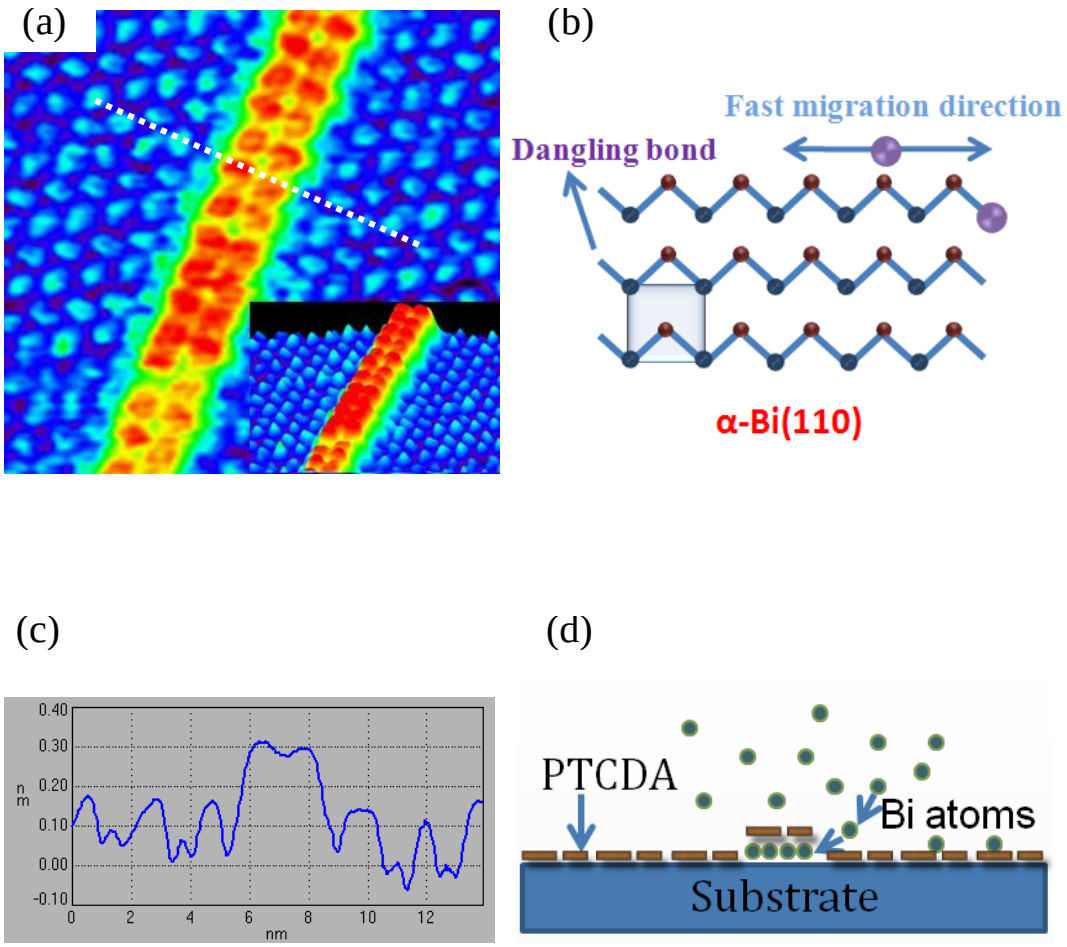

Fig. 4.5 (a) High-resolution STM image (16 nm×16 nm) of an ultra-thin Bi NW with PTCDA molecules on top. The inset shows a 3-D view of part of this NW. (b) Schematic diagram of growth of Bi(110) NWs. (c) A STM line profile of the dotted line in (a). (d) Schematic drawing of growth of ultra-thin Bi NWs with single-Bi(110)-layer thickness.

Chapter 3, single-layer Bi(110) has dangling bonds pointing out of the plane. In our situation, the on-top molecules apparently could saturate these dangling bonds, so even the mono-layer Bi(110) NW can be stable (or more likely meta-stable) at the initial growth stage. Being tightly bonded with the top PTCDA molecules, the single-layer Bi(110) NWs appear much thinner than the bulk thickness (3.28 Å). Based on the STM images, we draw a growth schematic image of ultra-thin Bi NWs as sketched in cross section view in Fig. 4.5 (d). Compared to inorganic surfaces, organic molecular layer is incompact, so there are big probabilities for Bi atoms to diffuse into the inter-molecular gap. With the passivation of the top facet, mono-atomic-layer NWs form. Furthermore, the herringbone bonded PTCDA pairs also provide a long-range path (molecular axis) for the anisotropic growth of Bi(110) NWs. Hence, stable mono-atomic-thin Bi NWs can grow and develop longer than 100 nm.

With a little more Bi deposition, mono-layer NWs developed into thicker but shorter NWs which are 4- or 6-atomic-layer thick. Fig. 4.6 (a) shows a high-resolution STM image of a thicker NW with well-ordered PTCDA molecular rows nearby. The orientation of this NW is aligned with the herringbone row axis of PTCDA. The line profile across the NW is shown in Fig. 4.6 (b), indicating it is a 4 atomic-layer-thick Bi NW.

This thickness change can be explained by the even layer growth model of Bi which is well established by Nagao *et al.* [31]. In this model, the neighboring two Bi(110) atomic layers reconstruct into puckered bi-layer structure to reduce the dangling bonds. However, 2-atomic-layer thick NWs cannot be found in our

experiment which indicates that the lowest thickness for stable NWs is 4-ML. By computing the volume (length × width × height) of the short 4-ML-thick NWs (e.g., the ones shown in Fig. 4.3 (d)), the volume increase is consistent with the increase of deposition amount. Hence, we propose that these 4-ML-thick NWs are developed from the single-layer ultra-thin NWs (as shown in Fig. 4.3 (c)). With more Bi atoms arriving, the chances for nucleation of second layer are increased and the ultra-thin NWs may break into several segments. With migration of existing and new arriving Bi atoms, these segments can grow into thicker but shorter rod-like NWs as shown in the STM image.

Additionally, our STM result shown in Fig. 4.6 (a) indicates that there are no PTCDA molecules on top of the NWs. This is also consistent with the even layer growth model in which there are no dangling bonds on the bi-layer surface. As shown in Fig. 4.6 (c), the molecules originally staying on top of the ultra thin NWs move to the side walls of the thicker NWs, indicated by the white arrows. Hence the side wall of the NWs becomes more inert and it is harder for the NWs to grow in width. Therefore, NWs with large L/W ratio can form. Based on the analysis, we draw the schematic model for the formation of thicker NWs, as shown in Fig. 4.6 (d).

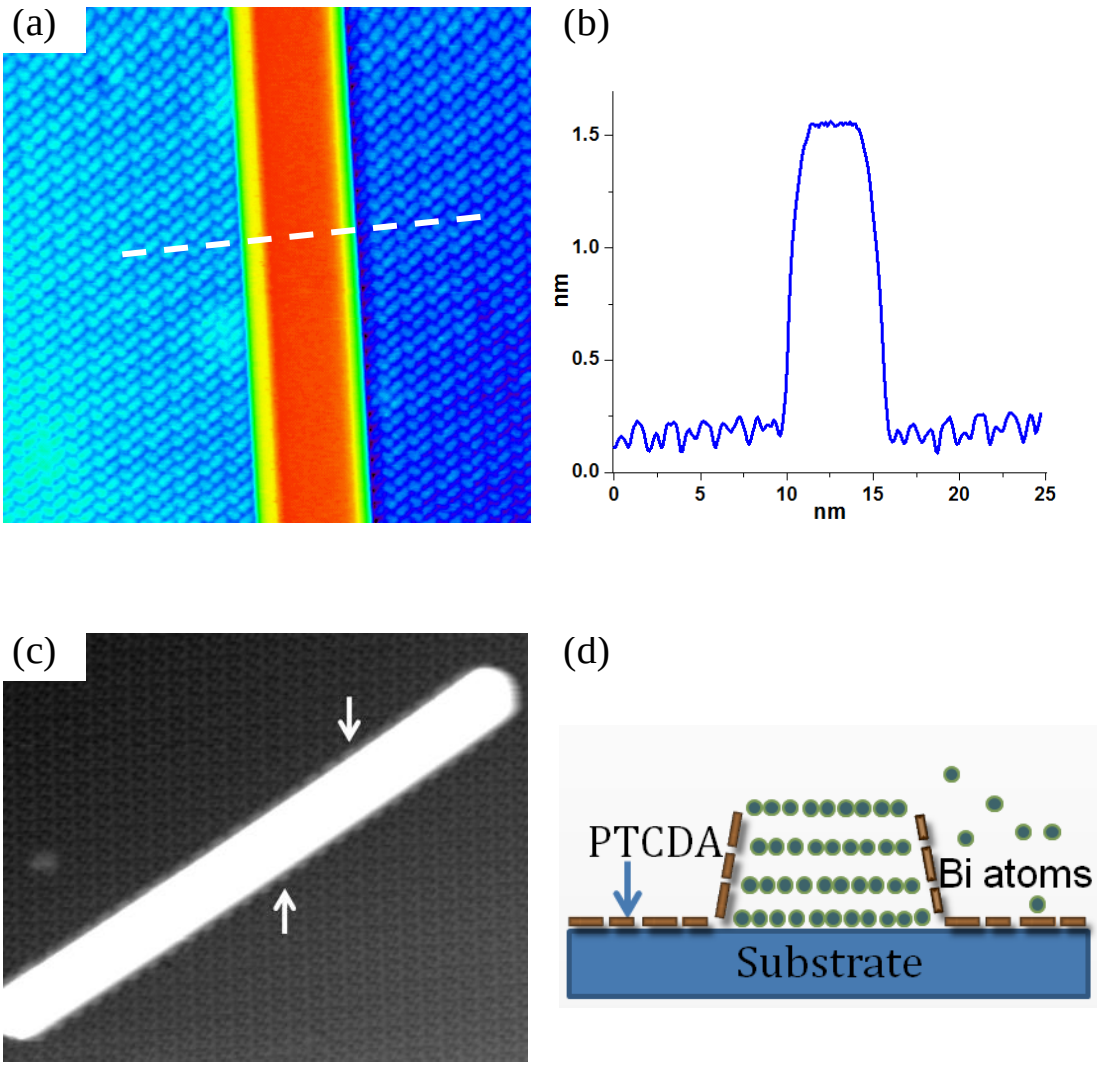

Fig. 4.6 (a) High-resolution STM image (40 nm×40 nm) of a 4-ML-thick Bi NW with PTCDA molecules nearby. (b) STM line profile across the thicker NW indicated by a dash line in (a). (c) A STM image (55 nm×45 nm) showing molecules attaching on the side wall of the thicker NW. (d) Schematic drawing of growth of 4-ML-Bi(110) NWs.

4.4.3 Orientation Distribution

Fig. 4.7 shows the orientation statistics of the large-LWR NWs in which $0°$ is defined as the direction in parallel to the herringbone axis as schematically drawn in Fig. 4.7. Besides the $0°$ peak, two sharp peaks at $49°$ and $-48°$ are consistent with the two molecular axes as drawn in Fig. 4.7. Notice that a small number of NWs are in other orientations. This is mainly due to the defect of MoS_2 substrate or boundaries of PTCDA domains. Compared to our previous work described in ***Chapter 3*** in which the Bi nanoribbons grow along six equivalent directions on the MoS_2 substrate, the sharp distribution of the orientations of the NWs shows a strong template effect of the PTCDA molecular layer on the growth kinetics of Bi NWs.

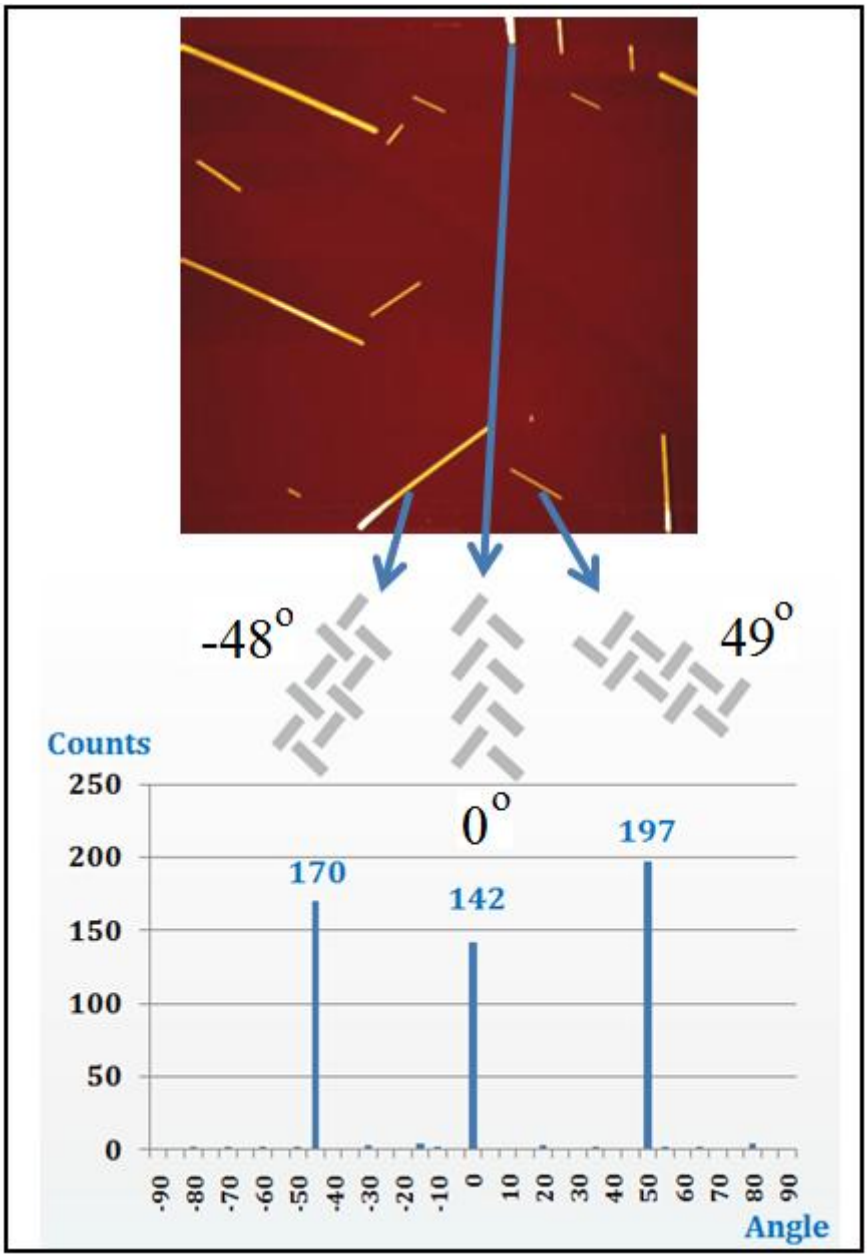

Fig. 4.7 Orientation distribution of Bi NWs with large L/W ratio. The three peak directions of Bi NWs with respect to the molecular lattice are illustrated in the STM image and molecular patterns above.

4.5 Conclusion

In conclusion, *in situ* STM is used to investigate the effect of PTCDA template layer on the growth of ultra thin Bi NWs and large-LWR Bi NWs on MoS_2. Because of the bonding between the Bi atoms and the PTCDA, aligned single-layer Bi NWs firstly form due to the top passivation and directional effect of the molecules. These ultra thin NWs then develop into thicker and much longer NWs when more Bi was deposited. Due to the side wall passivation by PTCDA, the NWs grow in length extensively but little in width, leading to the formation of large-LWR NWs. The surfactant and directional effects observed in our study may be extended to other molecule-nanowire-substrate systems for better control in nanowire self-assembly. It is also helpful to the fabrication of functional molecule-nanowire hybrid nanostructures.

References

[1] Y. Cui and C. M. Lieber, Science **291**, 851 (2001).

[2] Y. Li, F. Qian, J. Xiang, and C. M. Lieber, Mater. Today **9**, 18 (2006).

[3] Y. Xia, P. Yang, Y. Sun, Y. Wu, B. Mayers, B. Gates, Y. Yin, F. Kim, and H. Yan, Adv. Mater. **15**, 353 (2003).

[4] J.-M. Bonard, H. Kind, T. Stockli, and L.-O. Nilsson, Solid-State Electronics **45**, 893 (2001).

[5] W. U. Huynh, J. J. Dittmer, and A. P. Alivisatos, Science **295**,2425 (2002).

[6] X. Duan, C. Niu, V. Sahi, J. Chen, J. W. Parce, S. Empedocles, and J. L. Goldman, Nature **425**, 274 (2003).

[7] A. Kolmakov, and M. Moskovits, Annu. Rev. Mater. Res. **34**, 151 (2004).

[8] B. Weitzel and H. Micklitz, Phys. Rev. Lett. **66**, 385 (1991).

[9] S. Cho, Y. Kim, A. Freeman, G. Wong, J. Ketterson, L. Olafsen, I. Vurgaftman, J. Meyer, and C. Hoffman, Appl. Phys. Lett. **79**, 3651 (2001).

[10] L. Hicks, T. Harman, and M. Dresselhaus, Appl. Phys. Lett. **63**, 3230 (1993).

[11] S. Matsui, and Y. Ochiai, Nanotechnology **7**, 247 (1996).

[12] S. H. Hong, J. Zhu, and C. A. Mirkin, Science, **286**, 523 (1999).

[13] J. A. Dagata, Science **270**, 1625 (1995).

[14] M. D. Levenson, Solid State Technol. **September**, 81 (1995).

[15] P. N. Dunn, Solid State Technol. **June**, 49 (1994).

[16] X.-S. Wang, S.S. Kushvaha, X. Chu, H. Zhang, Z. Yan, and W. Xiao, The Oxford

Handbook of Nanoscience and Technology, pp. 572-597.

[17] Y. Xia, J. A. Rogers, K. E. Paul, and G. M. Whitesides, Chem. Rev. **99**, 1823 (1999).

[18] R. S. Wagner, and W. C. Ellis, Appl. Phys. Lett. **4**, 89 (1964).

[19] X. Duan, and C. M. Lieber, Adv. Mater. **12**, 298 (2000).

[20] S. Han, C. Li, Z. Liu, B. Lei, D. Zhang, W. Jin, X. Liu, T. Tang, and C. Zhou, Nano Lett. **4**, 1241 (2004).

[21] R. E. Algra, M. A. Verheijen, M. T. Borgstrom, L.-F. Feiner, G. Immink, W.J.P.V. Enckevort, E. Vlieg, and E.P.A.M. Bakkers, Nature, **456**, 369 (2008).

[22] C.N.R. Rao, F. L. Deepak, G. Gundiah, A. Govindaraj, Prog. Solid State Chem. **31**, 5 (2003).

[23] B. Gates, Y. Yin, and Y. Xia, J. Am. Chem. Soc. **122**, 12582 (2000).

[24] L. Manna, E. C. Scher, and A. P. Alivisatos, J. Am. Chem. Soc. **122**, 12700 (2000).

[25] L. Liang, Y. Zhang, G. Li, X. Wang, and L. Zhang, Mater. Lett. **59**, 1223 (2005).

[26] X.-S Wang, S. S. Kushvaha, Z. Yan, and W. Xiao, Appl. Phys. Lett. 88, 233105 (2006).

[27] W. Chen, H. Huang, S. Chen, L. Chen, H. L. Zhang, X. Y. Gao, and A. T. S. Wee, Appl. Phys. Lett. **91**, 114102 (2007).

[28] F. S. Tautz, Prog. in Surf. Sci. **82**, 479 (2007).

[29] S. Mannsfeld, M. Toerker, T. S. Hubsch, F. Sellam, T. Fritz, and K. Leo, Org. Elec. 2, 121 (2001).

[30] J. M. Mativetsky, S. A. Burke, S. Fostner, and P. Grutter, Nanotech. **18**, 105303 (2007).

[31] T. Nagao, J. T. Sadowski, M. Saito, S. Yaginuma, Y. Fujikawa, T. Kogure, T. Ohno, Y. Hasegawa, S. Hasegawa, T. Sakurai, Phys. Rev. Lett. **93**, 105501 (2004).

Chapter 5 LEED and STM Investigations of Bi on Ru(0001)

5.1 Introduction

For a long time, there has been a substantial effort to investigate the nucleation and growth of metal on metal (bimetallic system). On the one hand, it is because of the scientific interest in the fundamental understanding of the growth process from an atomistic view [1-3]. Many works, such as Ru/Pt(111) [4], Co/Cu(100) [5-7], Co/Cu(111) [8-11], Co/Pd(111) [12, 13], Co/Au(111) [14, 15], and Co/Ag(111) [15], have been done to investigate the growth behavior of metal-on-metal systems, showing useful fundamental understanding of correlations between structural modification of metal overlayer and the electronic properties. On the other hand, much more importantly, the bimetallic surfaces can be used as typical systems for investigating the functional properties of bimetallic materials, such as for catalytic applications [16-19] or magnetic recording technology [20, 21]. For example, bimetallic catalysts, which often show electronic and chemical properties that are distinctly different from those of the parent metals, offer the opportunity to obtain new catalysts with enhanced selectivity, activity and stability [21].

Ruthenium is a rare transition metal of the platinum group in the periodic table. It is a good catalyst for reactions with H_2 and CO and for reactions involving organic synthesis [22, 23]. Numerous studies have been devoted to determine the structures formed by hydrogen on Ru, particularly on its closed-packed hexagonal face, Ru(0001) [24]. In addition, Ru(0001) as a prototype surface for investigating the growth of bimetallic systems and epitaxial growth systems (such as Au [25], Ag [26,

27], Cu [26], Co-Ag [28], Pd [29], Ge [30] and perylene [31]), has attracted much attention in SPM experiments.

As the heaviest element in group V, bismuth (Bi) has attracted much attention in extensive investigation of growth behavior on various surfaces, such as Bi/Si(111) [32, 33], Bi/Si(100) [34], Bi/Si(001) [35], Bi/Ge(111) [36], Bi/HOPG [37-39], Bi/MoS_2 [40], Bi/Ag(111) [41], Bi/Au(111) [42], and Bi/Cu(001) [43]. However, investigation of nucleation and growth of Bi on Ru(0001) has been lacking. Moreover, because Bi has unique electronic properties [44-48], growth of Bi on Ru(0001) may show unexpected electronic and chemical characteristics as a bimetallic system. For one reason, the geometry of the Bi-Ru structure is typically different from that of the parent metals, e.g. the average metal-metal bond lengths changes. This gives rise to the strain effect that is known to modify the electronic structure of the metal through changes in orbital overlap [13]. For another reason, Bi deposited on Ru may show large Rashba-type spin-orbital splitting, such as Bi/Ag(111) [49-51] and Bi/Cu(111) [52].

In this chapter, I show the LEED and STM investigation of Bi deposition on Ru(0001). Three structural phases were revealed by using LEED and STM, when the Bi coverage ranged from sub-monolayer (sub-ML) to a few ML. We observed a loosely rectangular superlattice when a small amount of Bi was deposited. STM image shows a supercell of size 5.4 Å × 4.7 Å. With LEED, three equivalent domains which rotated 120° from each other were observed and the periodicity can be assigned as $2 \times \sqrt{3}$ with respect to Ru(0001). After more Bi was deposited, a compact

superstructure was observed. LEED pattern reveals that this is a hexagonal ($\sqrt{7} \times \sqrt{7}$)R19.1° superlattice. STM images show that every unit cell includes four atoms. When Ru(0001) was saturated with this ($\sqrt{7} \times \sqrt{7}$)R19.1°-Bi, it acts as a buffer layer and the surface becomes rather inert. With additional Bi deposited, Bi(110) thin film is formed on this inert substrate. LEED pattern reveals that the Bi(110) lattice constant is 4.6 Å × 4.8 Å. Schematic drawings of unit cell periods and orientations for these three kinds of Bi layers are proposed.

5.2 Experimental Method

The experiments were carried out in an Omicron UHV LT-STM system [53]. The base pressure is better than 1×10^{-10} Torr. Clean Ru(0001) surface with large terraces was obtained after a few cycles of Ar^+ ion bombardment and subsequent annealing at 1000 K. High purity (99.999%) Bi was evaporated from a Knudsen cell (MBE Komponenten, Germany) onto Ru(0001) at room temperature. Prior to the deposition, Bi was degassed at appropriate temperatures for a few hours in order to remove contaminations. The Bi flux was calibrated by depositing Bi on Si(111)-7×7 surface and counting the phase transition deposition amount as 6-ML of Bi(110), where 3.3 Å deposition represents 1 ML of Bi(110) (9.27×10^{14} atoms/cm^2) [32]. LEED pattern was obtained at the electron beam energy range of 65-75 eV. Once the sample was annealed, sufficient time was used to wait for sample cooling to take LEED pattern. All STM images were acquired at 77 K. The atomic resolution STM

images were carefully calibrated and the scanner drift was corrected [54].

5.3 Results and Discussions

5.3.1 LEED Observation of Three Structural Phases

LEED is a useful technique to determine the epitaxial growth and the overlayer structure in bimetallic surfaces, especially in identifying the periodicity of the metal overlayer with respect to the single crystal substrate. Fig. 5.1 shows the LEED patterns of structural evolution as Bi deposition was increased. Fig. 5.1 (a) displays the initial diffraction pattern when 0.4 Å Bi was deposited. The six sharp dots in the outer side represent the diffraction pattern from the Ru(0001) substrate, while the inner faint pattern corresponds to the Bi super-structure on top. This pattern is almost the same as that shown in Fig. 5.1 (b) obtained after ~1.4 Å Bi was deposited, except the faintness of the inner dots. The faintness is mainly because of the small coverage of super structure and the quasi-periodic lattice at the boundaries of the Bi-induced structure. This structural phase is called ***Phase I*** here and will be analyzed and discussed in detail in the following sub-sections.

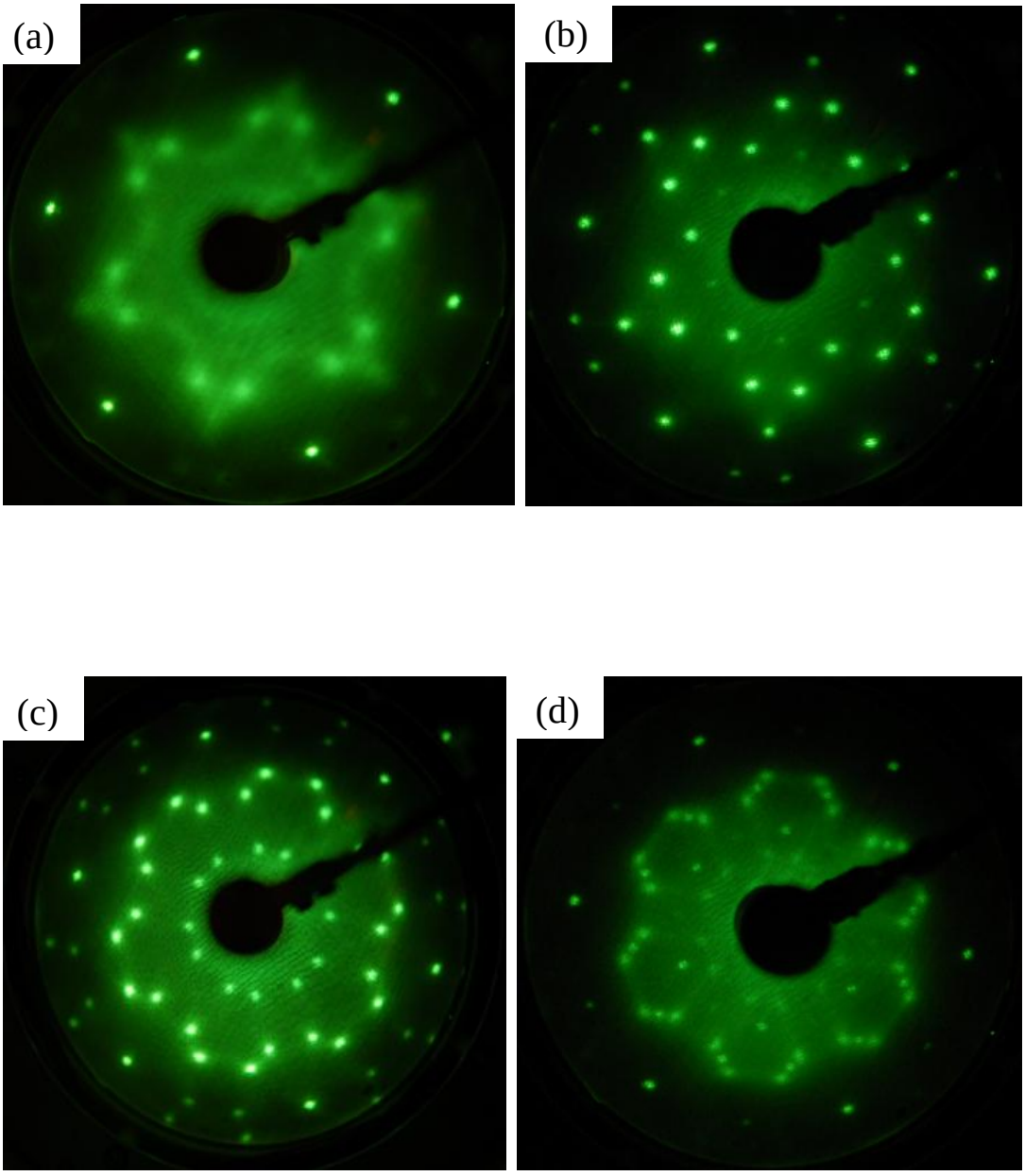

Fig. 5.1 LEED patterns evolution from ***Phase I*** to ***Phase III*** at different Bi deposition: (a) 0.4 Å, (b) 1.4 Å, (c) 3.4 Å, and (d) 8 Å, respectively. The electron beam energy is (a) 70.4 eV, (b) 68.5 eV, (c) 70.8 eV, and (d) 71.8 eV, respectively.

Fig. 5.1 (c) displays the LEED pattern of ***Phase II*** when 3.4 Å Bi was deposited. One can notice that the integer spots of Ru(0001) are surrounded by 12 dots, which represents two sets of relatively large hexagonal lattice in real space. Fig. 5.1 (d) shows the LEED pattern of mixed ***Phase II*** and ***Phase III*** after 8 Å Bi deposition. The dots from ***Phase II*** are relatively weak compared to that displayed in Fig. 5.1 (c), because of the attenuation effect from the Bi overlayer in ***Phase III***. The STM investigations of each phase will reveal more details in the subsequent sections.

5.3.2 Phase I: 2 × √3 lattice

When the Bi deposition is less than ~1.4 Å, Bi forms a rectangle $\begin{pmatrix} 2 & -2 \\ 1 & 1 \end{pmatrix}$ superstructure (which will be noted simply as 2 × √3 below) with three equivalent domains on Ru(0001). Fig. 5.2 (a) shows the LEED pattern at the initial growth stage, with 0.4 Å Bi deposited. We use vectors $\boldsymbol{a_1}^*/\boldsymbol{a_2}^*$ and $\boldsymbol{b_1}^*/\boldsymbol{b_2}^*$, respectively, to indicate Ru(0001) and one set of Bi lattice in reciprocal space. Using Eq. (2.16), the corresponding real space vectors $\boldsymbol{a_1}/\boldsymbol{a_2}$ and $\boldsymbol{b_1}/\boldsymbol{b_2}$ can be derived, as shown in Fig. 5.2 (b), where the black dots and red circles represent Ru and Bi unit cells, respectively. However, the nucleation site of every Bi atom is unknown, and Fig. 5.2 (b) only shows one possibility. With STM, one can see that the Bi-induced superstructure Bi islands formed on Ru terrace. Fig. 5.2 (c) displays an atomic resolution STM image at this initial growth stage. After correcting the scanner error (14.8% larger along horizontal scanning axis and 4.7% larger along vertical axis), the real size of STM

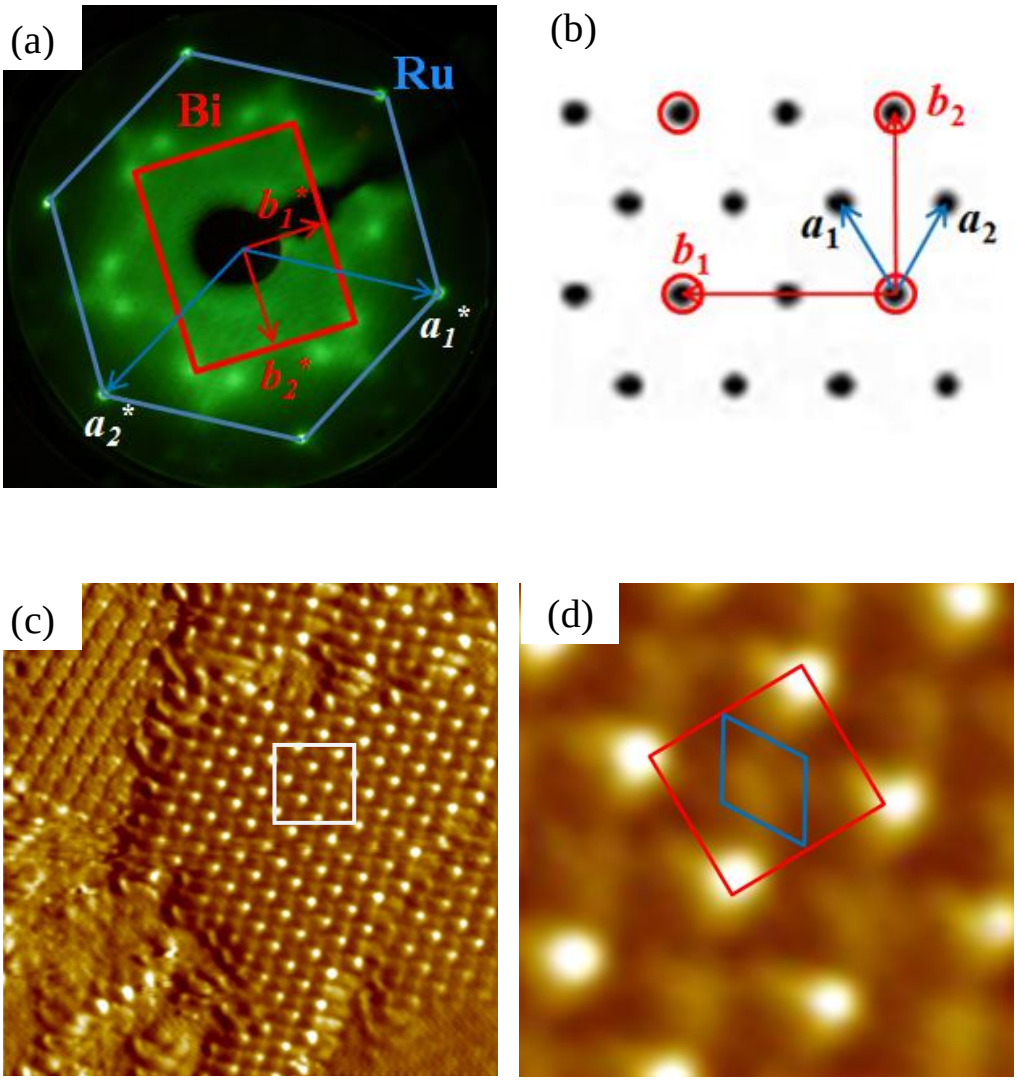

Fig. 5.2 (a) One set of Bi superlattice (shown in red rectangle) with respect to Ru(0001) substrate (shown in blue hexagon), with relative reciprocal vectors marked. (b) Unit cells in real space corresponding to the pattern shown in (a), with primitive vectors marked. (c) STM image (8.7 × 9.6 nm^2, -100 mV) of submonolayer Bi superlattice on Ru. (d) High resolution STM image (1.5×1.7 nm^2, V_s=-100 mV) showing the Bi superlattice in detail.

image of Fig. 5.2 (c) is 8.7 × 9.6 nm^2. Fig. 5.2 (d) shows the zoom-in image in the area indicated by a white rectangle in Fig. 5.2 (c). One superstructure unit cell is marked by a red rectangle. With careful calibration, the size of unit cell is measured to be 5.4 Å × 4.7 Å. This periodicity is exactly same as the 2 × √3 superlattice with respect to Ru(0001) measured from LEED pattern. The orientation of the underneath Ru(0001) lattice is indicated by a blue rhombus in Fig. 5.2 (d).

Fig. 5.3 (a) shows one set of the 2 × √3 superlattice LEED pattern (marked with red circles), decomposing from the three equivalent superlattice domains in the LEED pattern, obtained after ~1.4 Å Bi deposition. The spots shown in Fig. 5.3 (a) are much sharper than that in Fig. 5.2 (a), resulting from a well-established 2 × √3 superlattice overlayer. The other two sets of reciprocal base-vectors are shown in Fig. 5.2 (b), with corresponding dots marked with blue and yellow circles. Fig. 5.3 (c) displays the atomic resolution STM image of 2 × √3 superlattice which covers most of the samle surface now. The measured superlattice period, agrees fairly well with the 2 × √3 reconstruction on Ru(0001). Fig. 5.3 (d) shows the zoom-in image on the surface, with a unit cell marked.

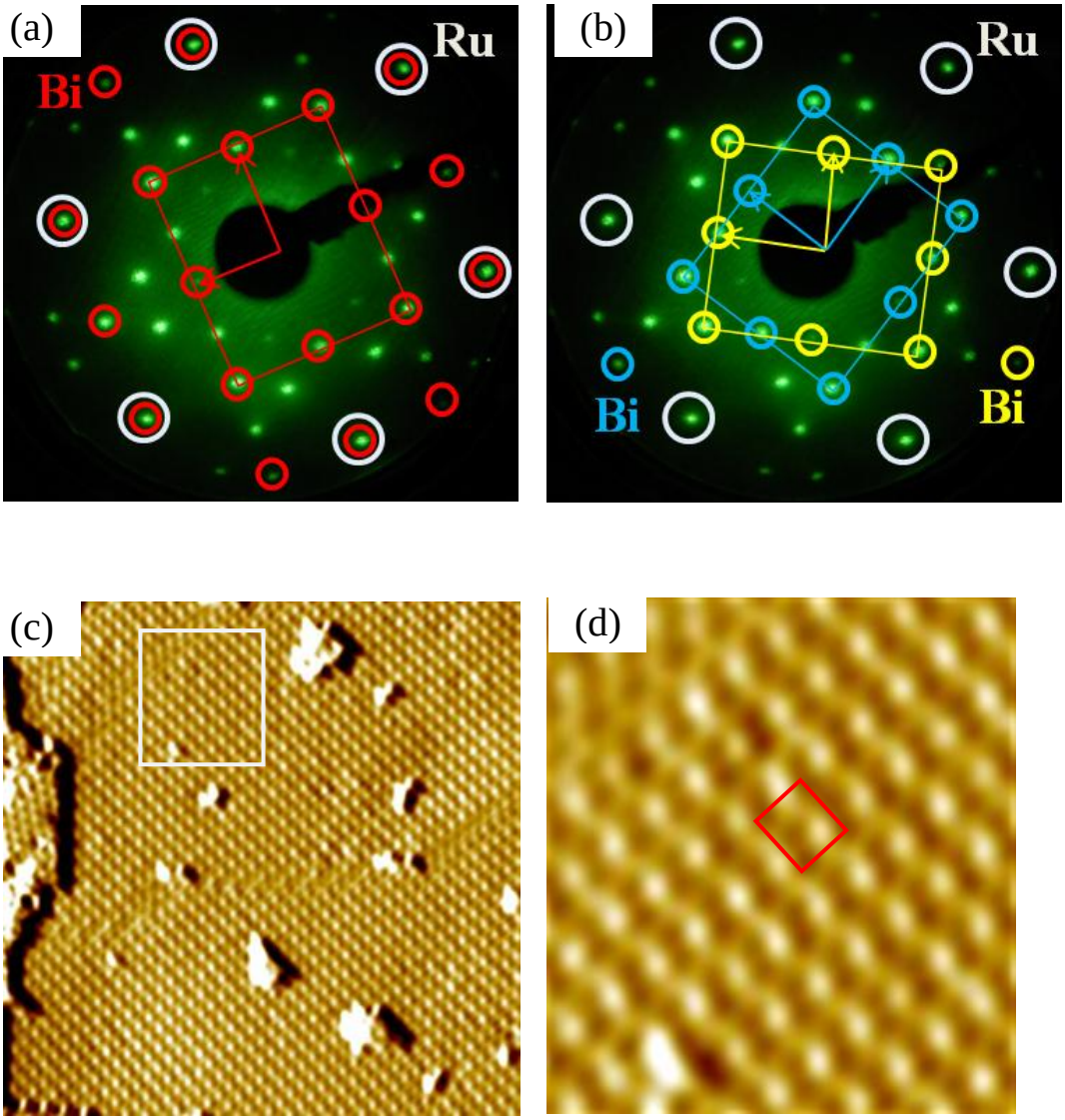

Fig. 5.3 (a) One set of decomposed LEED dots of ***Phase I***, represented by red circles. (b) The other two sets of 2 × √3 dots, shown by blue and yellow circles. (c) STM image (17.4×19.2nm^2, V_s=-100 mV) of 2 × √3 superlattice with ~1.4 Å Bi deposition. (d) High resolution STM image (4.6×4.6 nm^2, V_s=-100 mV) with a superlattice unit cell marked.

5.3.3 Phase II: $\sqrt{7} \times \sqrt{7}$ Super-lattice

With more Bi deposited (>3.4 Å deposition), The surface changed completely to another structural phase: ($\sqrt{7} \times \sqrt{7}$)R19.1 °lattice. Fig. 5.4 (a) shows the LEED pattern of this phase with sharp spots imaged. Using base vectors $\boldsymbol{a_1}^*/\boldsymbol{a_2}^*$, $\boldsymbol{b_1}^*/\boldsymbol{b_2}^*$ and $\boldsymbol{c_1}^*/\boldsymbol{c_2}^*$ for the unreconstructed Ru and the two sets of reconstructed lattices in reciprocal space (Fig. 5.4 (a) and (c)), the LEED pattern can be decomposed into two sets of hexagonal supercells, which tilt ±19.1 ° from the substrate lattice in real space. By using Eq. (2.16), the real space periods and orientations of the supercells can be drawn in Fig. 5.4 (b) and (d) with different rotation angle, respectively. Calculation from the reciprocal vectors gives the period of this hexagonal cell to be ~7.2 Å.

The real-space atomic structure of this phase is revealed partially by STM measurements. Fig. 5.5 (a) displays an unoccupied-state STM image obtained at +100 mV of the $\sqrt{7} \times \sqrt{7}$ superlattice. A red rhombus marks one unit cell with a ~7.3 Å periodicity. This number agrees well with that measured from the LEED pattern. One should notice that every spot in the image is evidently larger than normal atoms imaged by STM. This indicates that every spot is not simply comprised of just one atom. Scanned at occupied state (-100 mV), a more sophisticated atomic structure appears in the image, as shown in Fig. 5.5 (b). The period of the brightest spots is ~7.3 Å, corresponding to the size of $\sqrt{7} \times \sqrt{7}$ superlattice. Fig. 5.5 (c) shows one unit cell in high resolution, indicating that every unit cell is comprised of 4 atoms.

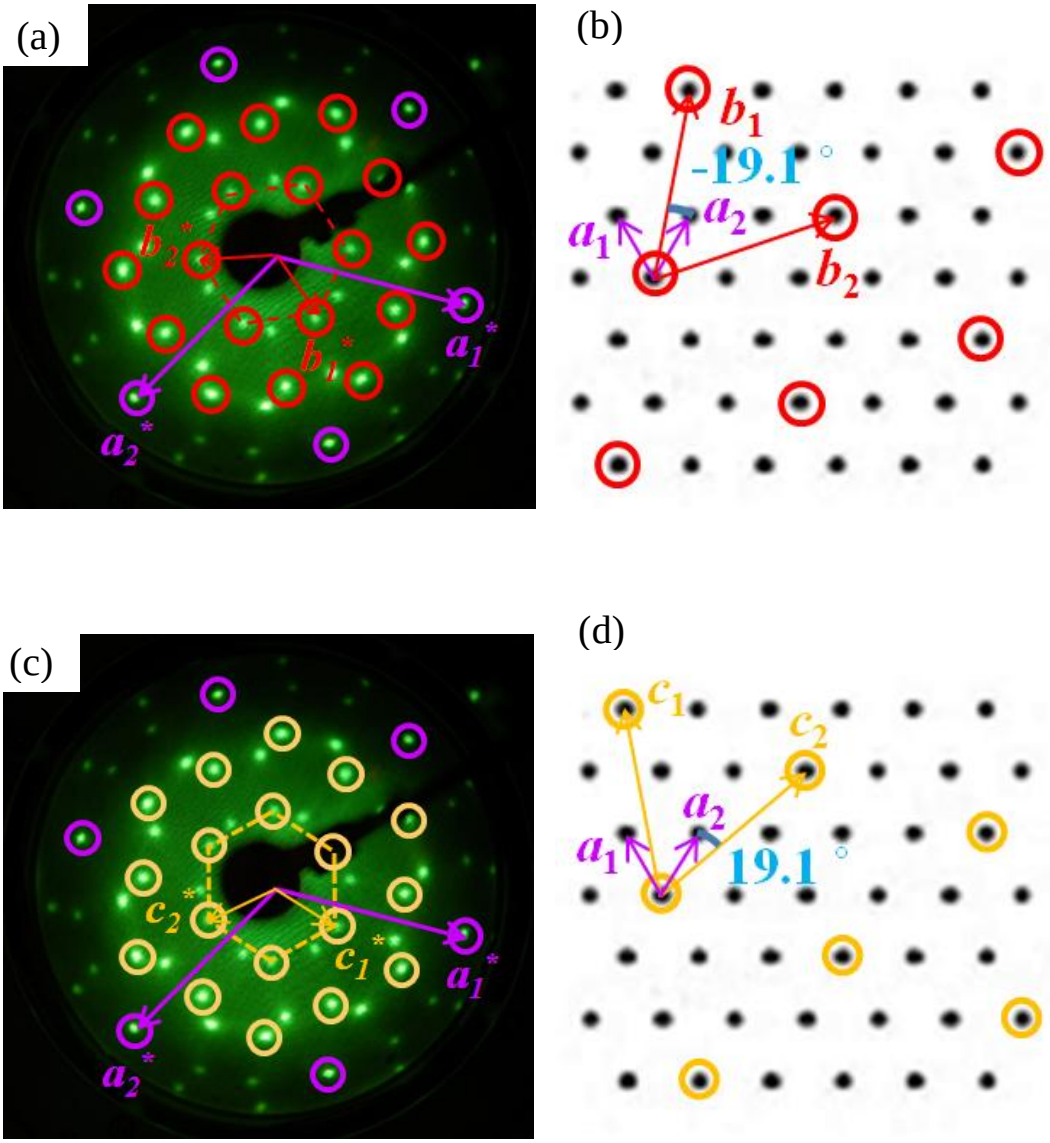

Fig. 5.4 (a) Decomposing of one set of lattice in ***Phase II*** in reciprocal space, displayed in red circles, and (b) the corresponding real space (√7 × √7)R(-19.1 °) unit cell with respect to Ru(0001). The other set of (√7 × √7)R19.1 °lattice is shown in (c) reciprocal space and (d) real space with yellow circles.

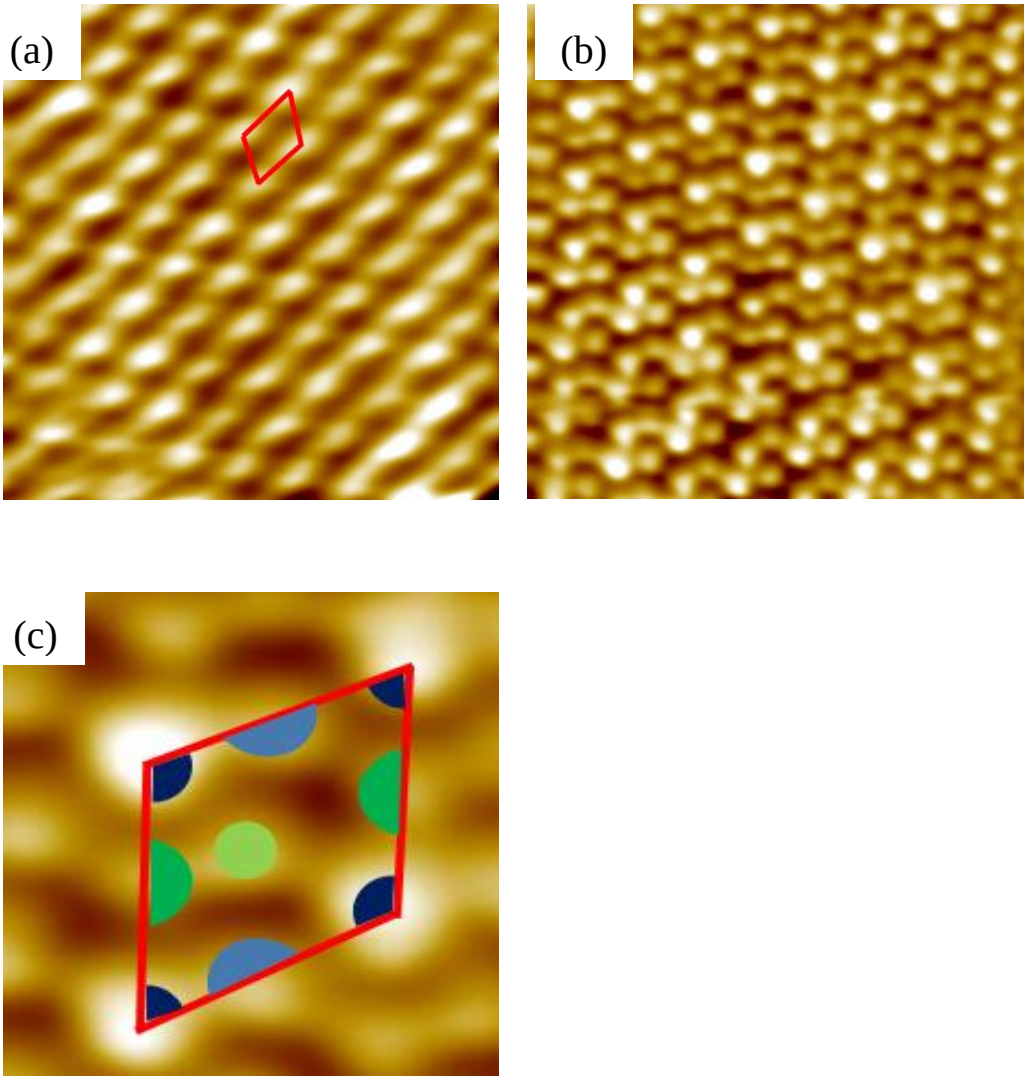

Fig. 5.5 Atomic resolution STM images of ***Phase II***: (a) unoccupied state image (+100 mV, 6.1×6.7 nm^2), with a √7 unit-cell marked with a red rhombus, and (b) occupied state image (-100 mV, 5.2×5.7 nm^2) showing the unit cell in detail. (c) High resolution STM image (1.3×1.6 nm^2) indicating 4 atoms/unit-cell.

However, based only on STM image, we still can not identify that if the four atoms in a unit cell are all Bi atoms. By comparing the Bi deposition amount, we can only confirm that the formation of √7 surface needs more Bi atoms than 2 × √3 surface. Because the sticking possibility of Bi atoms on the two surfaces may be rather different, without an accurate coverage monitoring method, the number of Bi atoms in one unit cell can not be accurately determined.

5.3.4 Phase III: Bi (110) Lattice

After the surface of Ru(0001) is completely covered with the compact √7 × √7 superlattice, it becomes saturated and rather inert. With more Bi deposited, besides the √7 spots, new spots appear, as shown in Fig. 5.6 (a). The new spots can be decomposed into three equivalent orientations with rectangular lattice. Fig. 5.6 (a) illustrates one set of new lattice with a red rectangle. The reciprocal base vectors for Ru and Bi are assigned as $\boldsymbol{a_1}^*/\boldsymbol{a_2}^*$ and $\boldsymbol{b_1}^*/\boldsymbol{b_2}^*$, respectively. By calculation, the size of the rectangular lattice is 4.6 Å × 4.8 Å, which agrees well with the Bi(110) lattice constants. Fig. 5.6 (b) shows the real space Bi(110) unit cell corresponding to the reciprocal lattice shown in Fig. 5.6 (a). Fig. 5.6 (c) reveals all the three equivalent Bi(110) domains which rotated 120 ° from one another. Besides the reciprocal base vectors shown in Fig. 5.6 (a), the other two sets of base vectors, $\boldsymbol{c_1}^*/\boldsymbol{c_2}^*$ and $\boldsymbol{d_1}^*/\boldsymbol{d_2}^*$, are drawn in blue and pink, respectively. The corresponding real space unit cells and orientations are drawn in Fig. 5.6 (d). Although the √7 × √7 Bi-Ru(0001) surface is

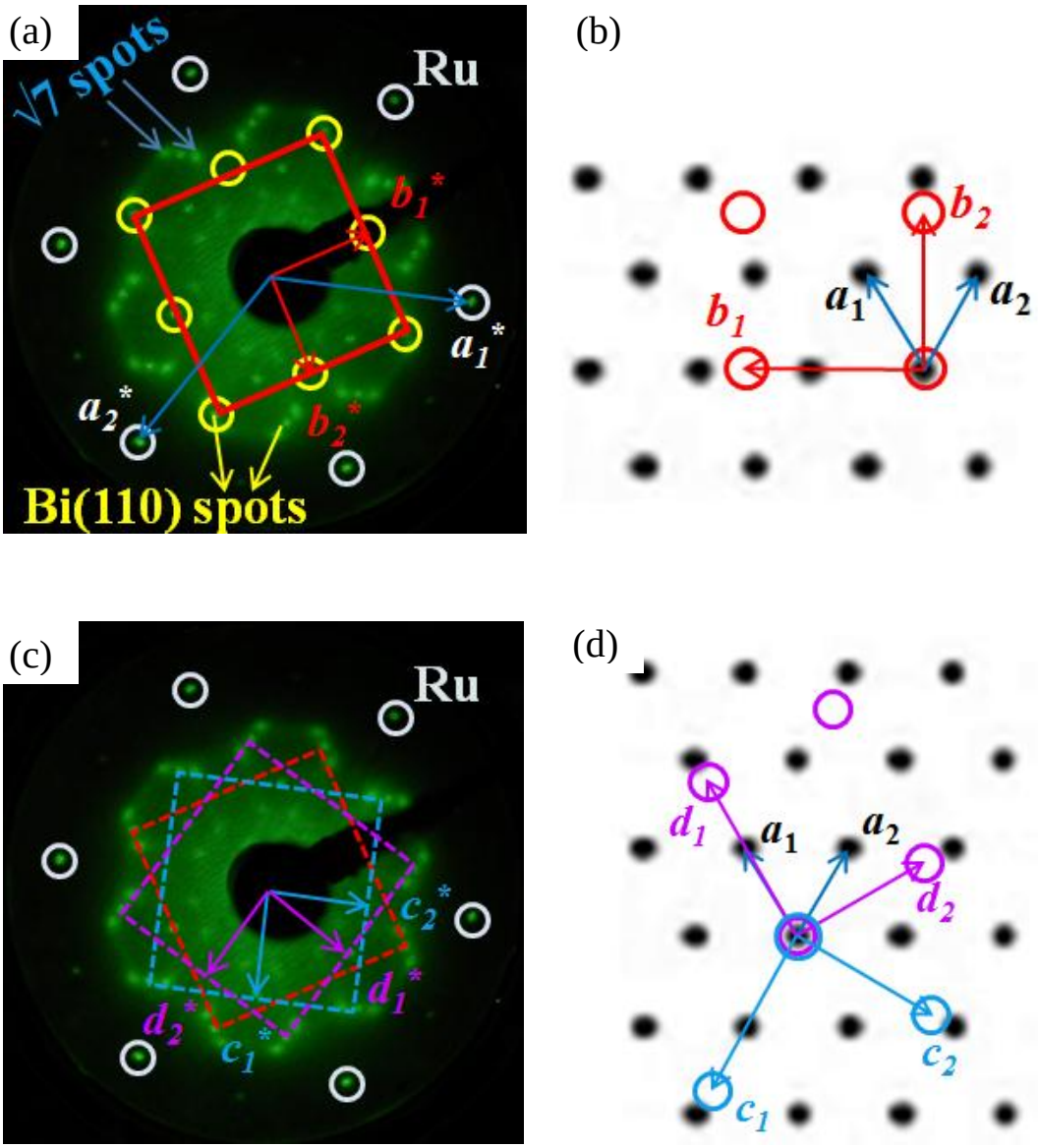

Fig. 5.6 (a) Decomposing of one set of lattice in ***Phase III*** in reciprocal space, displayed in red rectangle, and (b) the corresponding real space unit cell. (c) Three equivalent domains of Bi overlayer in ***Phase III***, shown by red, pink and blue rectangles in LEED pattern, and (d) the other two sets of Bi(110) unit cells shown in real space, besides the one shown in (b).

inert enough for the growth of Bi(110) overlayer, the orientation of Bi(110) lattice has fixed three orientations as indicated by the LEED pattern. It is different than the situation of Bi(110) nanoribbons on MoS_2(0001) (see ***Chapter 3***), which shows six broad-distributed orientation range. This suggests that the bonding of Bi(110) overlayer with $\sqrt{7} \times \sqrt{7}$ Bi-Ru(0001) surface is much stronger comparing to that with MoS_2(0001) surface.

Fig. 5.7 (a) displays the STM image of Bi(110) stripes on $\sqrt{7} \times \sqrt{7}$ Bi-Ru(0001) with 5 Å Bi deposited. The inset displays the LEED pattern of this sample, where the intensity of Bi(110) spots are much weaker than the $\sqrt{7}$ spots, obviously due to the low coverage of Bi(110) overlayer. Moreover, from the STM image, one can see that there are many small Bi clusters at the step edges and on the terraces. Some of them are rather mobile and can be dragged by the STM tip as shown Fig. 5.7 (a). This also indicates that the $\sqrt{7} \times \sqrt{7}$ surface is inert. Fig. 5.7 (b) shows one line profile across the Bi stripe, along the white line in Fig. 5.7 (a). The height of all Bi stripes is 7.8 Å, which suggests that the stripes are bi-layer of Bi(110). The height difference with the thickness of bulk Bi(110) bi-layer (6.6 Å) can be understand as the bonding between the strips and $\sqrt{7} \times \sqrt{7}$ Bi-Ru(0001) surface is relatively weak. Compared to the bi-layer-thick Bi nanoribbons grown on MoS_2(0001), which have uniform height of 8.6 Å at RT, the smaller height value of Bi(110) on $\sqrt{7}$ surface also indicates a stronger bonding between Bi(110) strips and this substrate than that on MoS_2.

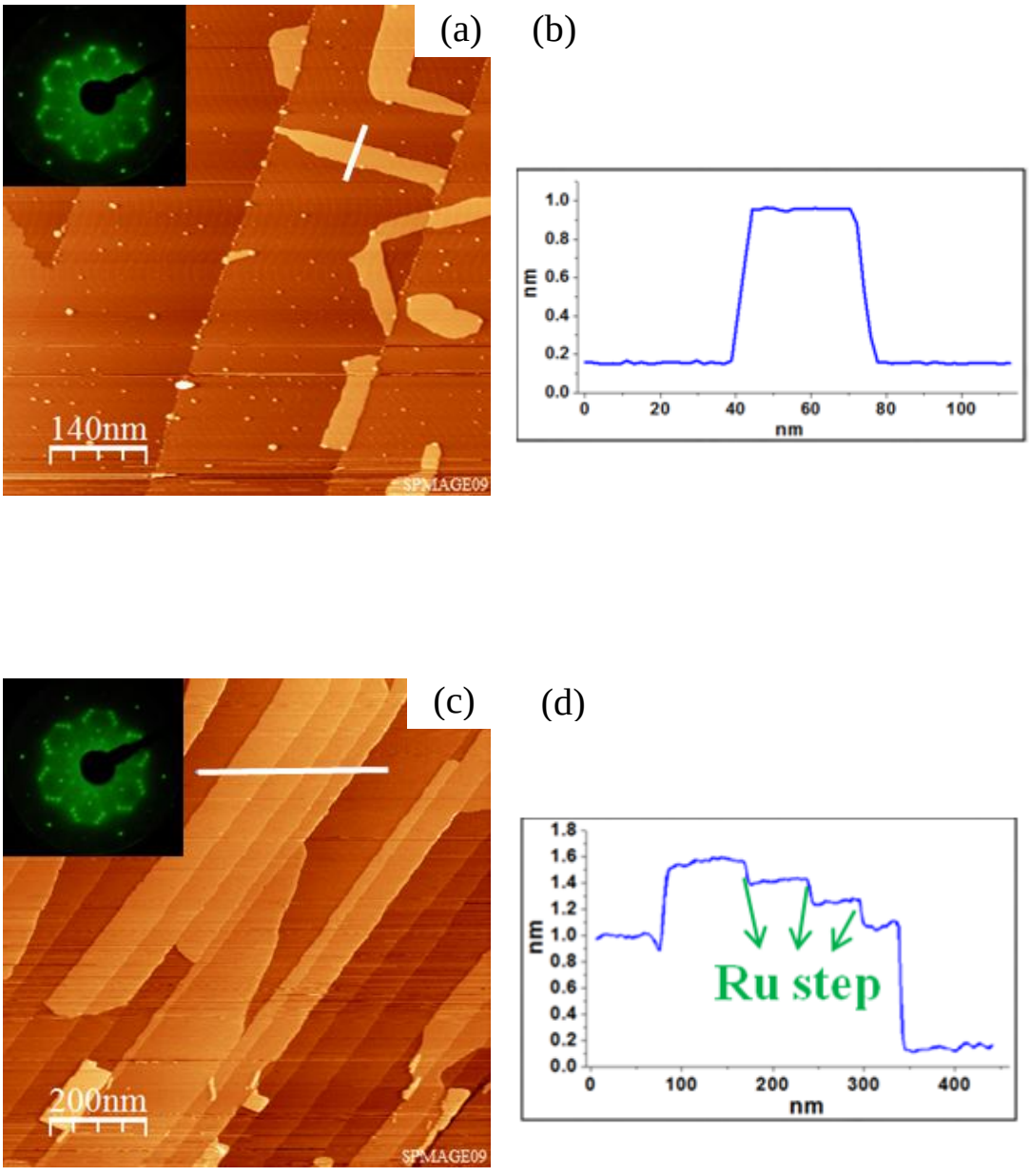

Fig. 5.7 (a) STM image of Bi(110) stripes on √7 × √7 Bi-Ru(0001) with 5 Å Bi deposited, and (b) a line profile showing the Bi(110) stripe has bi-layer thickness. (c) STM image of Bi(110) nanoribbons at 8 Å Bi deposition, and (d) a line profile across several Bi ribbons.

Fig. 5.7 (c) shows the STM image of Bi(110) ribbon-like structures with 8 Å Bi deposited. The inset LEED pattern shows that the intensity of Bi(110) spots become stronger than that in Fig. 5.7 (a), revealing the higher coverage of Bi(110) overlayer. 4-layer Bi(110) islands are found in a small fraction of surface area, as shown at the bottom part of Fig. 5.7 (c), resulting from new bi-layer Bi(110) nucleation on the existing Bi(110) bi-layer. Fig. 5.7 (d) shows the line profile across several Bi ribbons, as indicated by the white line in Fig. 5.7 (c). The steps at height of ~2 Å shown in the line profile indicates that these are Ru(0001) steps of height 2.14 Å [55] .

5.3.5 Reversible Phase Change by Sample Annealing

The above sub-sections introduced the surface structural evolution from ***Phase I*** to **Phase III** by increasing the Bi deposition amount. In the experiment, we found that the evolution can also be reversely obtained by annealing the sample at certain temperatures after sufficient Bi deposition. After we get the sample of mixed ***Phase II*** and ***Phase III***, as shown in Fig. 5.7 (c), by annealing it at ~120 ℃ for 20 minutes, the pattern of ***Phase III*** completely vanished, leaving pure $\sqrt{7} \times \sqrt{7}$ LEED pattern which is the same as that shown in Fig. 5.1 (c). STM images show that all the Bi(110) overlayer was desorbed, except several small Bi clusters (size < 3 nm) attaching to steps (STM image not shown). This situation is similar to Bi on HOPG and MoS_2, in which Bi can be desorbed by heating the sample at ~120 ℃.

In addition, once the $\sqrt{7} \times \sqrt{7}$ Bi-Ru(0001) surface was annealed at ~370 ℃ for

another 20min, the LEED pattern completely changed to $2 \times \sqrt{3}$, as shown in Fig. 5.1 (b). During the annealing process, the mixed pattern of ***Phase I*** and ***Phase II*** was also observed. The annealing experiment suggests that the structural phase transition is caused by the amount of Bi atoms. Further annealing the sample at 580 ℃, the LEED pattern changed to the initial blurred one as shown in Fig. 5.1 (a), which indicates that more Bi atoms in $2 \times \sqrt{3}$ structure desorbed by breaking the bonding with Ru atoms at higher temperature.

5. 4 Conclusions

In this chapter, I demonstrate the structural phase transition of Bi on Ru(0001) by using LEED and STM. Three structural phases, i.e. $2 \times \sqrt{3}$, $\sqrt{7} \times \sqrt{7}$ and Bi(110), were obtained by adding the Bi deposition amount. By decomposing the LEED pattern and calculating the lattice parameters, the real space lattice periods and orientations of each structural phase are resolved. STM images reveal the periodicity of the real space structures of each phase (Bi(110) atomic structure not shown) and are in good agreement with the LEED patterns. Annealing experiment proves that the phase transition from ***Phase I*** to ***Phase II*** is triggered by the amount of Bi atoms. The $\sqrt{7} \times \sqrt{7}$ phase is a more compact structure on Ru(0001) than the $2 \times \sqrt{3}$. The growth behavior of Bi(110) structures is similar to that on an inert substrate (HOPG or MoS_2). Our experiment extends the understanding of nucleation and thin film growth of Bi on Ru(0001). The stable superlattice surface ($2 \times \sqrt{3}$ and $\sqrt{7} \times \sqrt{7}$) can act as new type

of substrate for the growth of inorganic and organic nanostructures. The electronic structures of each phase may exhibit interesting features which do not exist on either pure Bi or Ru surface.

References

[1] E. Bauer In: D. A. King and D. P. Woodruff, Editors, *The chemical Physics of Solid Surfaces and Heterogeneous Catalysis* **Vol. 3**, Elsevier, Amsterdam (1983).

[2] J. A. Venables, Surf. Sci. **299/300**, 798 (1994).

[3] H. Brune, Surf. Sci. Rep. **31**, 121 (1998).

[4] A. Berkó, A. Bergbrelter, H. E. Hoster, and R. J. Behm, Surf. Sci. **603**, 2556 (2009)

[5] H. Li, and B. P. Tonner, Surf. Sci. 237, 141 (1990).

[6] A. K. Schmid, and J. Kirschner, Ultramicroscopy 42-44, 483 (1992)

[7] J. R. Cerda, P. L. D. Andres, A. Cebollada, R. Miranda, E. Navas, P. Schuster, C. M. Schneider, and J. Kirschner, J. Phys. C: Condens. Mat. 5, 2055 (1993).

[8] V. Scheuch, K. Potthast, B. Voigtländer, and H. P. Bonzel, Surf. Sci. 318, 115 (1994).

[9] J. de la Figuera, J. E. Prieto, C. Ocal, and R. Miranda, Surf. Sci. 307, 538 (1994).

[10] S. Speller, S. Degroote, J. Dekoster, G. Langouche, J. E. Ortega, and A. Närmann, Surf. Sci. 405, L542 (1998).

[11] J. E. Prieto, J. de la Figuera, and R. Miranda, Phys. Rev. B 62, 2126 (2000).

[12] M. Wasniowska, N. Janke-Gilman, W. Wulfhekel, M. Przybylski, and J. Kirschner, Surf. Sci. 601, 3073 (2007).

[13] M. Wasniowska, W. Wulfhekel, M. Przybylski, and J. Kirschner, Phys. Rev. B 78, 035405 (2008).

[14] B. Voigtländer, G. Meyer, and N. M. Amer, Phys. Rev. B 44, 10354 (1991).

[15] K. Morgenstern, J. Kibsgaard, J. V. Lauritsen, E. Laesgaard, and F. Besenbacher, Surf. Sci. 601, 1967 (2007).

[16] C. T. Campbell, Annu. Rev. Phys. Chem. **41**, 775 (1990).

[17] J. A. Rodriguez, Surf. Sci. Rep. **24**, 223 (1996)

[18] J. H. Sinfelt, Surf. Sci. **500**, 923 (2002).

[19] J. G. Chen, C. A. Menning and M. B. Zellner, Surf. Sci. Rep. **63**, 201 (2008)

[20] J. Shen, and J. Kirschner, Surf. Sci. **500**, 300 (2002).

[21] S. D. Bader, Surf. Sci. **500**, 172 (2002).

[22] Y. J. Bei, S. D. Zhang, J. C. He, J. C. Wu, Y. Yang, Platinum Metals Rev. **49**, 91 (2005).

[23] S.-I. Murahashi, H. Takaya, T. Naota, Pure Appl. Chem. **74**, 19 (2002).

[24] H. Shi, K. Jacobi, Surf. Sci. **313**, 289 (1994).

[25] R. Q. Hwang, J. Schröder, C. Günther, and R. J. Behm, Phys. Rev. B **67**, 3279 (1991).

[26] J. L. Stevens, and R. Q. Hwang, Phys. Rev. Lett. **74**, 2078 (1995).

[27] R. Q. Hwang, J. C. Hamilton, J. L. Stevens, and S. M. Foiles, Phys. Rev. Lett. **75**, 4242 (1995).

[28] R. Q. Hwang, Phys. Rev. Lett. **76**, 4757 (1996).

[29] N. Rougemaille, F. E. Gabaly, R. Stumpf, A. K. Schmid, K. Thürmer, N. C. Bartelt, and J. De la Figuera, Phys. Rev. Lett. **99**, 106101 (2007).

[30] H. J. Zhang, B. Lu, X.-S. Wang, F. Hu, H. Y. Li, S. N. Bao, and P. He, Phys, Rev. B **70**, 235415 (2004).

[31] Y.F. Xu, H.J. Zhang, Y.H. Lu, B. Song, Q. Chen, H.Y. Li, S.N. Bao, and P. He, Surf. Sci. **600**, 2002 (2006).

[32] T. Nagao, J. T. Sadowski, M. Saito, S. Yaginuma, Y. Fujikawa, T. Kogure, T. Ohno, Y. Hasegawa, S. Hasegawa, T. Sakurai, Phys. Rev. Lett. **93**, 105501 (2004).

[33] S. Yaginuma, T. Nagao, J. T. Sadowski, A. Pucci, Y. Fujikawa, and T. Sakurai, Surf. Sci. **547**, L877 (2003).

[34] C. Bobisch, A. Bannani, M. Matena, and R. Möller, Nanotechnology **18**, 055606 (2007).

[35] G. Jnawali, H. Hattab, C. A. Bobisch, A. Bernhart, E. Zubkov, R. Möller, and M. H.-V. Hoegen, Surf. Sci. **603**, 2057 (2009).

[36] S. Hatta, Y. Ohtsubo, S. Miyamoto, H. Okuyama, T. Aruga, App. Surf. Sci. **256**, 1252 (2009).

[37] S. A. Scott, M. V. Kral, and S. A. Brown, Surf. Sci. **587**, 175 (2005).

[38] S. A. Scott, M. V. Kral, and S. A. Brown, Phys. Rev. B **73**, 205424 (2006).

[39] S. A. Scott, M. V. Kral, and S. A. Brown, Phys. Rev. B **72**, 205423 (2005).

[40] X.-J. Chu, S. S. Kushvaha, H.-L. Zhang, X.-S. Wang, (Unpublished)

[41] C. R. Ast, G. Wittich, P. Wahl, R. Wogelgesang, D. Pacilé, M. C. Falub, L. Moreschini, M. Papagno, M. Grioni, and K. Kern. Phys. Rev. B **75**, 201401(R) (2007).

[42] J. H. Jeon, K. H. Chung, H. Kim, and S.-J. Kahng, Surf. Sci. **603**, 145 (2009).

[43] P. Wynblatt, D. Chatain, and A. Ranguis, Surf. Sci. **601**, 1623 (2007).

[44] C. R. Ast and H. Höchst, Phys. Rev. Lett. **87**, 177602 (2001).

[45] T. Hirahara, T. Nagao, I. Matsuda, G. Bihlmayer, E. V. Chulkov, Y. M. Koroteev, P. M. Echenique, M. Saito, and S. Hasegawa, Phys. Rev. Lett. **97**, 146803 (2006).

[46] C. A. Hoffman, J. R. Meyer, F. J. Bartoli, A. Divenere, X. J. Yi, C. L. Hou, H. C. Wang, J. B. Ketterson, and G. K. Wong, Phys. Rev. B **48**, 11431 (1993).

[47] Z. B. Zhang, X. Z. Sun, M. S. Dresselhaus, J. Y. Ying, and J. Heremans, Phys. Rev. B **61**, 4850 (2000).

[48] T. E. Huber, A. Nikolaeva, D. Gitsu, L. Konopko, C. A. Foss, and M. J. Graf, Appl. Phys. Lett. **84**, 1326 (2004).

[49] T. Hirahara, T. Nagao, I. Matsuda, G. Bihlmayer, E. V. Chulkov, Y. M. Koroteev, P. M. Echenique, M. Saito, and S. Hasegawa, Phys. Rev. Lett. **77**, 3419 (1996).

[50] C. R. Ast, J. Henk, A. Ernst, L. Moreschini, M. C. Falub, D. Pacile, P. Bruno, K. Kern, and M. Grioni, Phys. Rev. Lett. **98**, 186807 (2007).

[51] C. R. Ast *et al.* Phys. Rev. B **77**, 081407(R) (2008).

[52] H. Mirhosseini, J. Henk, A. Ernst, S. Ostanin, C.-T. Chiang, P. Yu, A. Winkelmann, and J. Kirschner Phys. Rev. Lett. **79**, 245428 (2009).

[53] W. Chen, H. Li, H. Huang, Y. Fu, H. L. Zhang, J. Ma, and A. T. S. Wee, J. Am. Chem. Soc. **130**, 12285 (2008).

[54] S. S. Kushivaha. X.-S. Wang, X.-J. Chu, H.-L Zhang, Z.-J. Yan, W.-D. Xiao, Handbook of Nanoscience and Nanotechnology, A. V. Narlikar and Y. Y. Fu Ed. New York: Oxford University Press, pp. 572-597 (2010).

[55] Z. Song, T. Cai, J. C. Hanson, J. A. Rodriguez, and J. Hrbek, J. Am. Chem. Soc. **126**, 8576 (2004).

Chapter 6 Size Tunable Au Nanoparticles on MoS_2

6.1 Introduction

When the size of a particle shrinks to nano-scale, it may show interesting size-dependent electronic, magnetic, optical, chemical (catalytic) and biological properties which are significantly different than their bulk counterpart. For example, bulk gold (Au) is one of the most chemically inert subjects [1]. However, since the discovery of active Au nanoparticles (NPs) for low temperature CO oxidation in the late 1980s [2], increasing number of experiments have been reported on the reactions catalyzed by nano-sized Au particles [3-7]. It has been shown by Haruta *et al.* that the size of Au cluster is a key factor to the catalytic activity [8]. Bond *et al.* demonstrated that the Au NP size must be less than 5 nm to obtain catalytic activity [9]. Hence, it is essential to explore high-yield synthesize approaches for Au NPs with well-controlled size, shape and location. To reveal the intrinsic properties of Au NPs, it is also important that such Au NPs being prepared on conducting substrates so the samples are suitable for characterization using scanning tunneling microscopy (STM), photoemission spectroscopy (PES) and electron energy loss spectroscopy (EELS).

Over past decades, researchers have conducted numerous methods to synthesize Au NPs. Among the conventional methods of synthesis of Au NPs, the most popular one for a long time has been that using citrate reduction of $HAuCl_4$ in water, introduced by Turkevitch in 1951 [10]. Using this method, the size of Au NPs could

be controlled by varying the stabilizer/gold ratio [11]. In 1994, a new method called "Brust-Schiffrin method" was reported and it had a considerable impact on the overall field. This method allowed the facile synthesis of thermally stable and air-stable Au NPs of reduced dispersity and controlled size for the first time. The diameter of Au NPs is ranged between 1.5 and 5.2 nm. Besides, people have tried many other methods for synthesizing size-controllable Au NPs by chemical and physical methods, such as two-phase synthesis and stabilization by thiols or other surfactants, seeding growth, chemical/physical vapor deposition [12].

Recently, self-assembly has been considered as a much favored bottom-up fabrication approach for its advantages of yielding nanostructures down to atomic scale and the potential for inexpensive mass fabrication [13]. Moreover, inert substrates such as HOPG and MoS_2 are widely used for investigating nearly free-standing nanoparticles and nanostructures due to their chemical inert surfaces that are easy to prepare [14, 15]. There have been literatures reporting self-assembly of Au NPs on HOPG and MoS_2 visualized with STM [16, 17], including controlling the size of Au NPs by organic solvent on graphite [13]. Nevertheless, the size of self-assemble Au NPs on MoS_2 remains above 10 nm because of coalescence of Au NPs, and there has been no report on size-tunable Au NPs synthesized on MoS_2.

In this chapter, I present the synthesis and characterization of size-tunable Au NPs on MoS_2 using PTCDA as a surfactant layer. PTCDA is a planar π-conjugated molecule and is of particular interest in organic and molecular electronics. It can form well-defined crystalline monolayer [18]. The structure and morphology of PTCDA on

MoS_2 is shown in Fig. 4.2 (***Chapter 4***). The surfactant effect of PTCDA for fabrication of Au NPs on MoS_2 and the morphology are investigated with STM which reveals that pre-deposited PTCDA overlayer can greatly increase the nucleation density of Au NPs and prevent fine NPs from aggregating into larger particles at room temperature (RT). Molecular scale images show that Au atoms nucleate and grow into NPs underneath the PTCDA layer and lift the molecules to the top of the NPs. Moreover, by annealing the sample, PTCDA molecules can desorb from the MoS_2 surface first and then desorb from the top of Au NPs at even higher temperature. By controlling the deposition amount of Au, the size of Au NPs can be tuned. In addition, interaction of Au NPs with PTCDA was investigated *in-situ* by XPS and charge transfer from Au NPs to PTCDA was observed, which indicates these Au NPs may have new chemical properties.

6.2 Experimental Method

The experiment was conducted in an ultrahigh vacuum (UHV) system (base pressure ~ 5×10^{-11} Torr) equipped with STM and Auger electron spectroscopy (AES). [15] Clean MoS_2 substrate was prepared by cleaving in air and then quickly transferred into UHV system, followed by an overnight degassing at 400 ℃. PTCDA molecules were deposited firstly onto the clean substrate at RT from a Ta crucible, and the sample is then annealed at ~100 ℃ for 30 min to form a flat, uniform PTCDA mono-layer. High purity (99.999%) Au wetted on a resistively heated tungsten wire

was deposited on the PTCDA/MoS_2 surface subsequently at RT. The Au source was kept at a sufficient distance away from the substrate to avoid activating chemical reaction or diffusion on the surface. Before deposition, Au source was degassed at appropriate temperature for a few hours to remove contaminations. The flux was calibrated using AES and STM. All the molecular scale images were carefully calibrated to eliminate scanner drift. The XPS experiment was performed at the SINS beamline of the Singapore Synchrotron Light Source in total electron yield mode with a photon energy resolution of 0.1 eV. PTCDA and Au were *in situ* deposited from a *K* cell and resistively heated Au source respectively in the main analysis chamber at RT. All the spectra measurements were performed at RT.

6.3 Results and Discussions

6.3.1 Morphology of Au NPs

The STM images shown in Fig. 6.1 reveal morphological difference of Au NPs on MoS_2 without and with PTCDA overlayer. In order to directly compare the difference and calibrate the Au flux rate, we deposited 1 Å Au on bare MoS_2 substrate first. As shown in Fig. 6.1 (a), Au form triangular crystalline islands in a Volmer-Weber growth mode on clean MoS_2 (i.e. without PTCDA). These Au islands, called "old" ones and acting as reference "landmark", have an average height of 4.8±0.5 nm and lateral size (referring to the side length of the triangles) of 21±2 nm as indicated

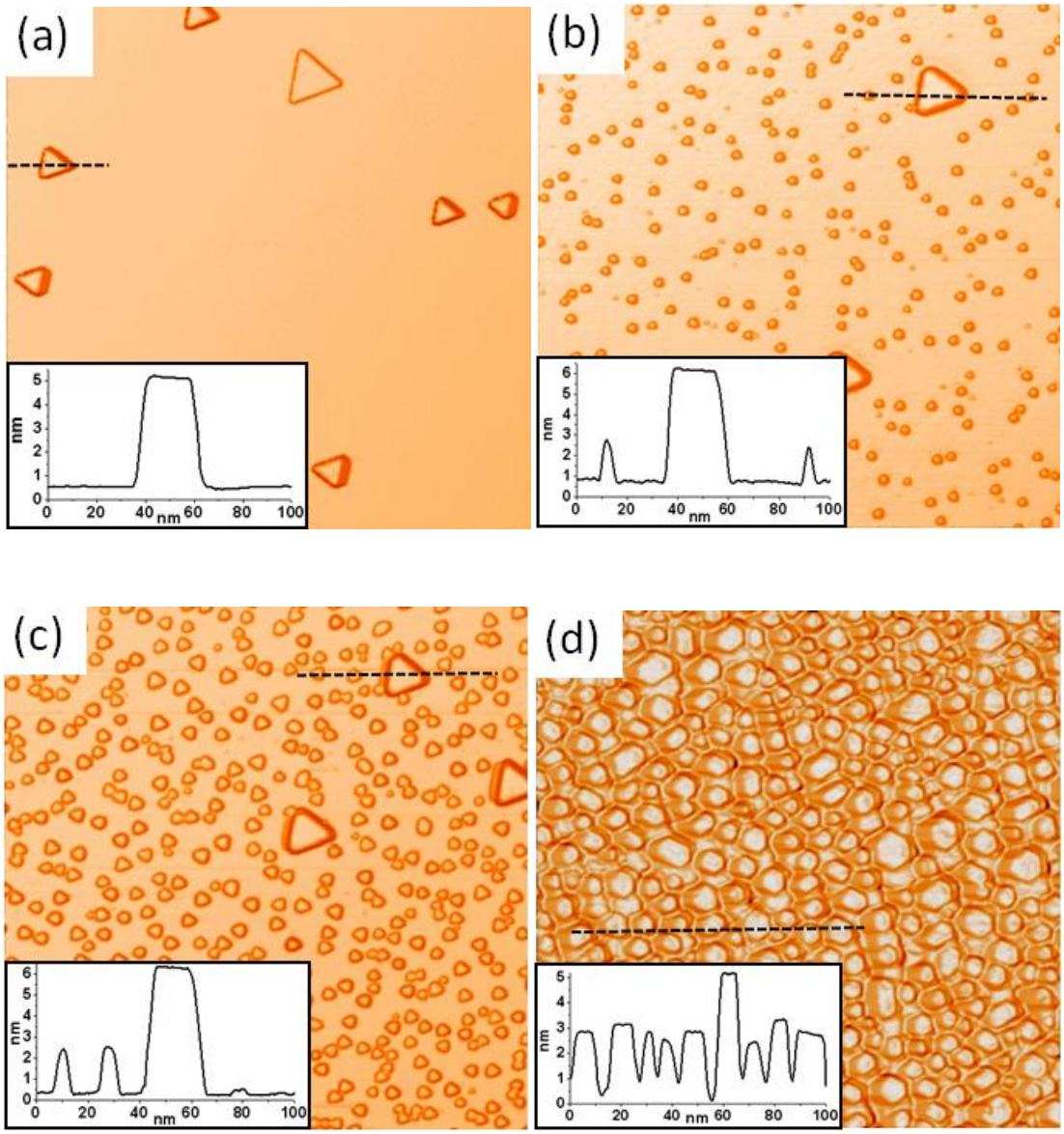

Fig. 6.1 STM images of (a) 3D Au islands on clean MoS_2 after 1 Å deposition as reference islands, and Au NPs on PTCDA covered MoS_2 (with reference islands) after (b) 0.16 Å, (c) 0.32 Å and (d) 8.8 Å additional Au deposition. The insets show the line profile of every image as indicated by black dash lines. The scanning area are: (a) 500×500 nm^2, (b) 300×300 nm^2, (c) 300×300 nm^2, and (d) 200×200 nm^2.

by the line profile in the inset of Fig. 6.1 (a). After overlaying 1 ML PTCDA on the sample in Fig. 6.1 (a), more Au was deposited and STM images taken after different amount of Au depositions are shown in Fig. 6.1 (b) - (d). Fig. 6.1 (b) shows the initial formation of smaller, denser and randomly dispersed "new" Au NPs when 0.16 Å Au was deposited. The "new" Au NPs are evidently much smaller than the "old" ones, indicating the surfactant and stabilizing effect of the PTCDA to prevent the NPs from coalescing together. The effect of PTCDA molecules will be discussed in detail later. The height and size of these NPs are relatively uniform, at values around 1.3 ±0.1 nm and 4.2 ±0.2 nm, respectively. If the bonding distance of PTCDA and Au is considered to be 0.33 nm [19], and the PTCDA monolayer thickness is 0.25 nm [20], the height and size of pure Au NPs are about 1 nm and 2.9 nm, respectively, at initial stage. Unlike the hemisphere-shaped NPs in Fig. 6.1 (b), Fig. 6.1 (c) shows the formation of quasi-triangle-shaped NPs after 0.32 Å Au was deposited. Instead of coalescing to form bigger islands, the NPs grow independently due to the side-passivation by PTCDA, although the side molecules are unable to be resolved by STM. The height of these NPs remains in the range of ~1 nm to ~1.5 nm, indicating the top of NPs is passivated by the molecules as well. The insets of Fig. 6.1 show the STM line profiles at each Au deposition stage and display obvious differences between the "new" Au NPs and the "old" islands. After 8.8 Å Au was deposited, as shown in Fig. 6.1 (d), the PTCDA/MoS_2 surface was mostly covered by much larger Au NPs with height similar to that of the "old" ones. But the lateral size distribution of these NPs is relatively broad. This is because some of the NPs were formed at the initial stage and

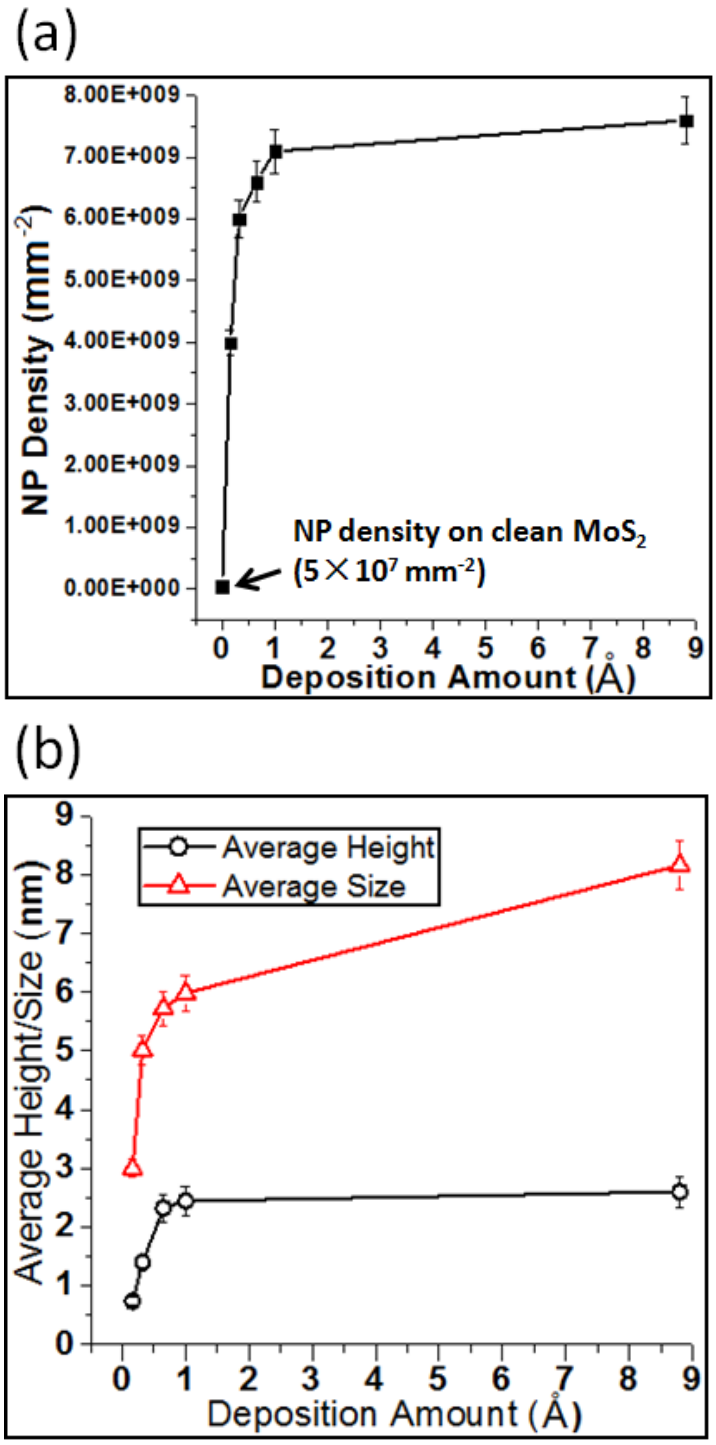

Fig. 6.2 Statistical (a) Au NP density, and (b) average height and lateral size of Au NPs as a function of deposition amount.

others were formed rather late. Therefore, different growing time and random coalescence resulted in the NPs with a broad size distribution.

Figure 6.2 shows the plots of the Au NP density, average height and lateral size as a function of deposition. As shown in Fig. 6.2 (a), the density of Au NPs at 1 Å deposition without PTCDA is only around 5×10^{7} mm^{-2}. However, when deposited on PTCDA overlayer, the density of Au NPs increased dramatically by a factor of 80 at 0.16 Å deposition and by 120 at 0.32 Å deposition. The increase of Au NP density can be ascribed to PTCDA molecular layer which reduces the diffusion length of Au atoms and clusters, and increase the cluster nucleation probability. The covering molecules also retard the coalescence of Au NPs, even they are close to one another, as shown in Fig. 6.1 (c) where many NPs are in contact. Fig. 6.2 (b) shows the average height and lateral size of the NPs as a function of Au deposition. At initial stage, the average NP height is less than 1 nm and lateral size is less than 3 nm. More Au deposition caused bigger and higher NPs formed as shown in Fig. 6.2 (b). Both diagrams show a tendency of saturation at the end stage, which means the surface was fully filled with NPs. There has been no void area for nucleation of new NPs, and the lateral growth of the NPs was limited as well. Before the NP density reaches saturation, the NP size can be tuned by controlling Au deposition amount with a PTCDA layer as surfactant.

6.3.2 Effect of PTCDA Molecular Layer

Figure 6.3 (a) and (b) show the molecular scale STM images of the Au NPs at different size. In Fig. 6.3 (a), the PTCDA molecules can be seen both on MoS_2 substrate and on the Au NPs as indicated by the 3-D view inset. However, the in-plane arrangement of PTCDA on top of small NPs (lateral size $\leq$ 16 nm) is not a regular herringbone pattern as that on the extended Au(111) [21], indicating that the bonding between PTCDA molecules is modified due to the limited top area of the small Au NPs. On the other hand, Fig. 6.3 (b) shows a larger NP with PTCDA in regular herringbone order on top except those near the edge. Since PTCDA molecules have been found on top of Au NPs, a possible growth schematic diagram for the Au NPs is drew in Fig. 6.3 (c) and 6.3 (d). It is well known that metal atoms defuse into organic materials [22]. S and Au atoms are also known to form a relatively strong bond easily. When Au atoms land on the PTCDA/MoS_2 surface, they can readily penetrate through the PTCDA layer and diffuse underneath the molecules and nucleate into clusters as sketched in Fig. 6.3 (c). With the effect of top-passivation by PTCDA, the height of Au NPs remains below 3 nm when Au deposition is less than 8.8 Å. Moreover, the Au NPs are protected by the PTCDA surfactant and the diffusion of Au atoms is retarded by PTCDA. These make the newly arriving Au atoms harder to be integrated into the existing NPs. This dramatically increases the possibility of nucleating new NPs at the vacant area.

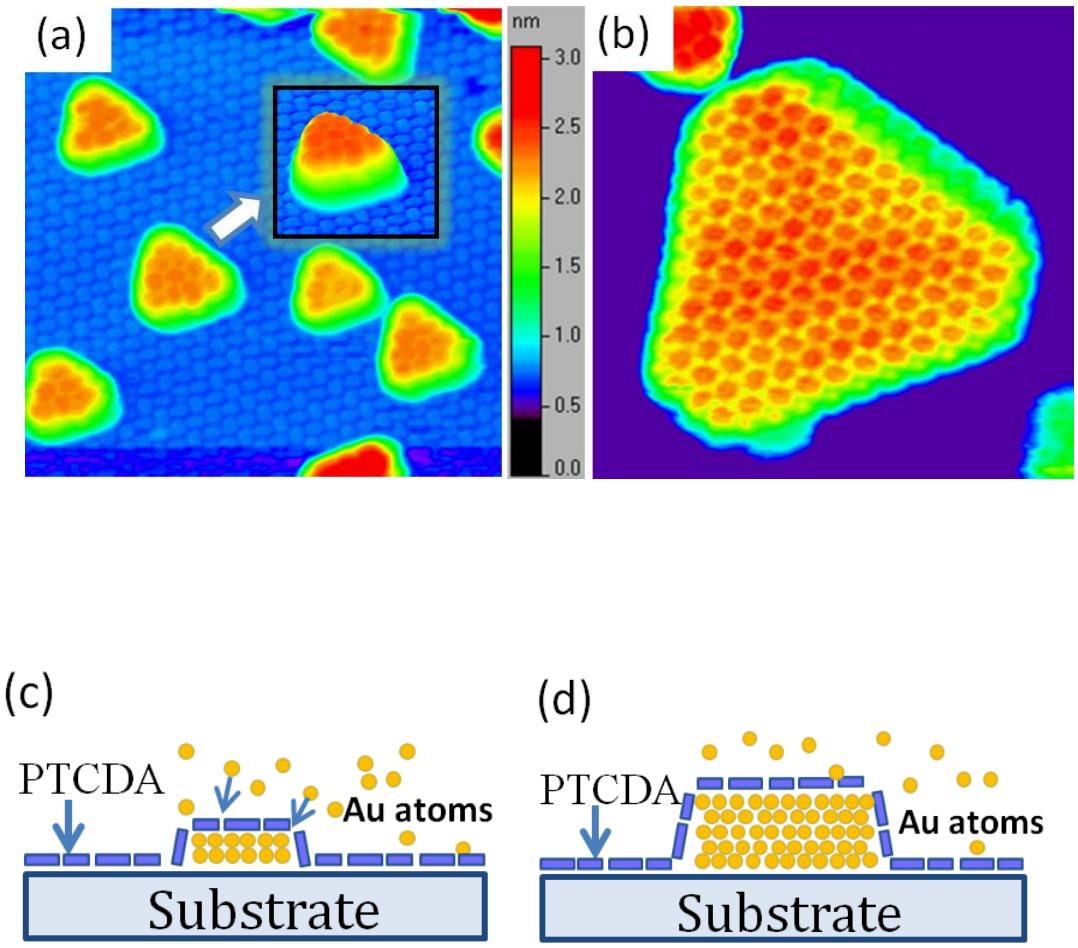

Fig. 6.3 Molecular scale STM images of (a) small crystal Au NPs with PTCDA molecules on top and substrate. The inset shows a 3D view of one NP. (b) A bigger Au island with herringbone bonded PTCDA on top. The scanning parameters are: (a) 20 × 20 nm^2, V_s=-2.6 V; (b) 20 × 20 nm^2, V_s=-1.9 V. Schematic drawing of possible growth models and configurations of PTCDA with (c) small and (d) big Au NPs.

6.3.3 Desorption of PTCDA

As PTCDA normally forms well-ordered organic film with herringbone-like inter-molecular bonding, desorption of crystalline PTCDA requires a higher temperature than other functional molecules, such as C_{60} and pentacene [23]. This temperature is also higher than that of Bi on MoS_2. So we can not get ultra-thin Bi NWs (shown in ***Chapter 4***) isolated from PTCDA molecules. However, Au has much better thermal stability on MoS_2 than PTCDA, so PTCDA molecules can be desorbed by annealing the sample. Fig. 6.4 (a) shows a 3-D view STM image of a sample with 0.32 Å Au deposited. Well-ordered PTCDA monolayer on MoS_2 and on Au NPs can be clearly imaged by STM. When the sample was annealed at 245 ℃ for 20 min, all the PTCDA molecules on the substrate surface were desorbed, as shown in Fig. 6.4 (b), while PTCDA on Au NPs remained. Once this sample was heated at 270 ℃ for another 20 minutes, STM image (Fig. 6.4 (c)) indicates that almost all the molecules on top of Au NPs were desorbed, whereas the morphology of most Au NPs changed little. Fig. 6.4 (d) displays the sample morphology in large scale, showing the dispersed small Au NPs and larger reference Au "old" islands. Now, we get bare Au NPs of size ~5 nm. Adsorption, desorption and reaction of gas molecules such as CO, O_2, CO_2 and NO on these bare Au NPs, in contrast to that on the larger Au islands, can be investigated in order to reveal their properties related to catalysis.

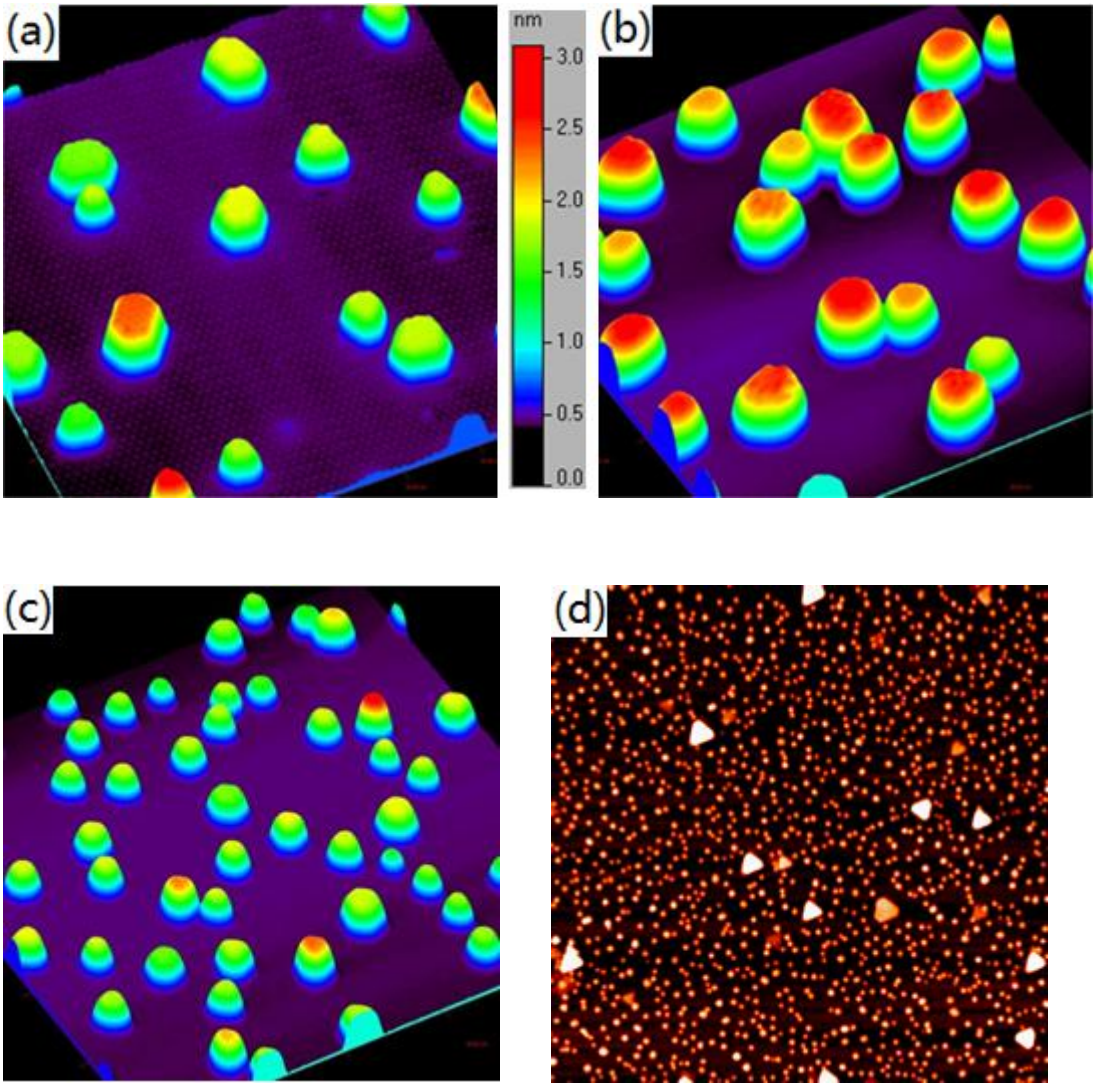

Fig. 6.4 3-D STM images showing desorption of PTCDA molecules and final sample morphology viewed in large scale. (a) A sample with 0.32 Å Au deposited, with PTCDA molecules clearly seen on MoS_2 and Au NPs. (b) STM image showing PTCDA only on top of Au NPs after annealing at 245 ℃. (c) STM image indicating most PTCDA have been desorbed after annealing at 270 ℃. (d) Final sample morphology with both dispersed small "new" Au NPs and large reference "old" Au islands. The image sizes are (a) 70×70 nm^2, (b) 60×60 nm^2, (c) 100×100 nm^2, and (d) 500×500 nm^2.

6.3.4 XPS Investigation of Interaction of Au NPs with PTCDA

In the XPS experiments, PTCDA was first deposited on clean MoS_2 surface at RT. The carbon 1s core level spectra were recorded at PTCDA deposition amount of 0.5 ML and 1 ML, as shown in Fig. 6.5. The spectra have two main peaks at binding energies of 284.8 eV and 288.4 eV. The one at 284.8 eV is assigned to carbon in the perylene core of the PTCDA molecule and the one at 288.4 eV to the carboxylic group [24, 25]. Our spectrum for 1 ML PTCDA is very similar to the one for thick PTCDA films on Ag(111) [26] and on Ag/Si(111)- $\sqrt{3} \times \sqrt{3}$ [25] where the components are related to the pure molecular film. This indicates that PTCDA deposited on MoS_2 has little interaction with the inert substrate. When 0.2 Å Au was added on the 1 ML PTCDA, new components appear. The peaks have an obvious broadening and a binding energy shift of ~0.2 eV, as shown in Fig. 6.5. Fitting of the components in the C 1s spectra has been done with the background reduced by an integrating Shirley function [25] and is shown in Fig. 6.6 (a) and (b) for PTCDA without and with Au, respectively.

As shown in Fig. 6.6 (a), the main peak at 284.8 eV is descomposed into two components labeled ***a*** and ***b***. Component ***a*** is assigned to the twelve carbon atoms with only C-C bonds and ***b*** to the eight atoms with a C-H bond [25]. This assignment is supported by calculations of the atomic charges in a PTCDA molecule which show that the latter C atoms are negatively charged, while the twelve C atoms with

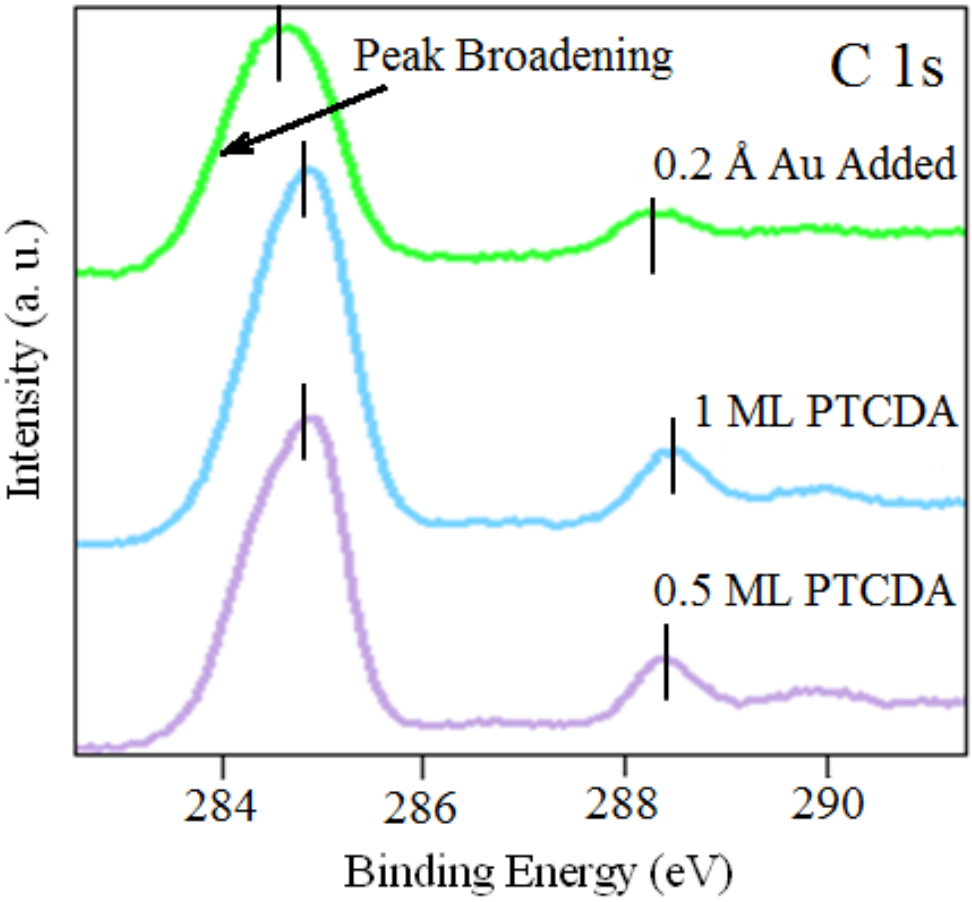

Fig. 6.5 Normalized C 1s XPS spectra for varying the thicknesses of PTCDA at 0.5 ML and 1 ML and 0.2 Å Au added.

only C-C bonds have no or very little net charge [27]. The smaller feature labeled ***c*** at 288.4 eV is from the C atoms in the carboxylic groups, since the higher electronegativity of the O atoms giving a higher binding energy to these electrons [24, 25, 27]. The other smaller peaks ***d***, ***e*** and ***f*** have previously been assigned to shake-up effects [26, 28, 29].

With 0.2 Å Au added subsequently on the 1 ML PTCDA, which corresponds to a sample similar to that shown in Fig. 6.1 (c), the spectrum shows obviously some new components. Based on the STM observations, we know that there are two kinds of PTCDA molecules once Au is added: unchanged PTCDA on MoS_2 substrate and those being lifted up by the Au NPs. Therefore, the components due to PTCDA on MoS_2 (***a***, ***b***, ***c***, ***d***, ***e***, and ***f***) should remain. A possible fitting for the new spectrum is shown in Fig. 6.6 (b), with new components ***g*** and ***h*** added. These two components are ~0.3 eV shifted from the two main peaks at 284.8 eV and 288.4 eV towards smaller binding energy, which indicates that both the perylene core and the carboxylic groups on the NPs are more negatively charged than those on MoS_2. This suggests an electron transfer from the Au NPs to the top PTCDA layers. This result is different than the previous work [30] showing that there is no charge transfer between PTCDA and bulk Au substrate ($\sqrt{3} \times 22$-Au(111), 5×20-Au(100) and 5×27-Au(100)). Thus, the XPS results indicate that our Au NPs have different chemical properties than that of bulk Au, and may exhibit desirable catalytic activities.

(a)

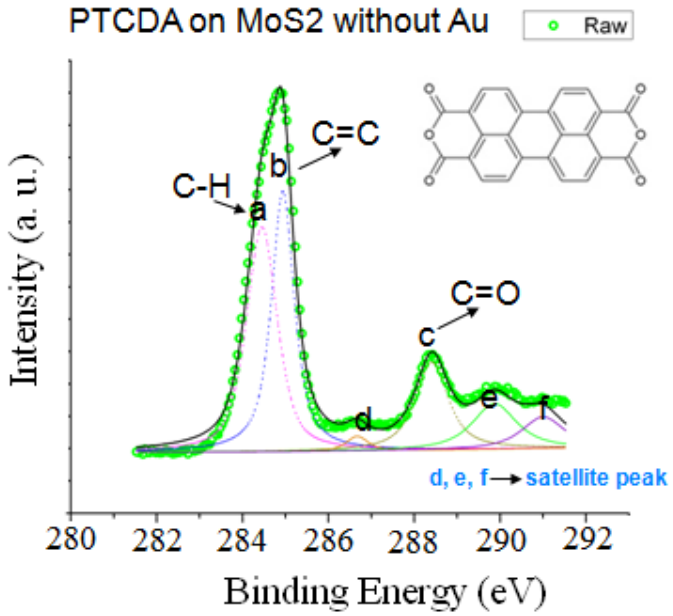

(b)

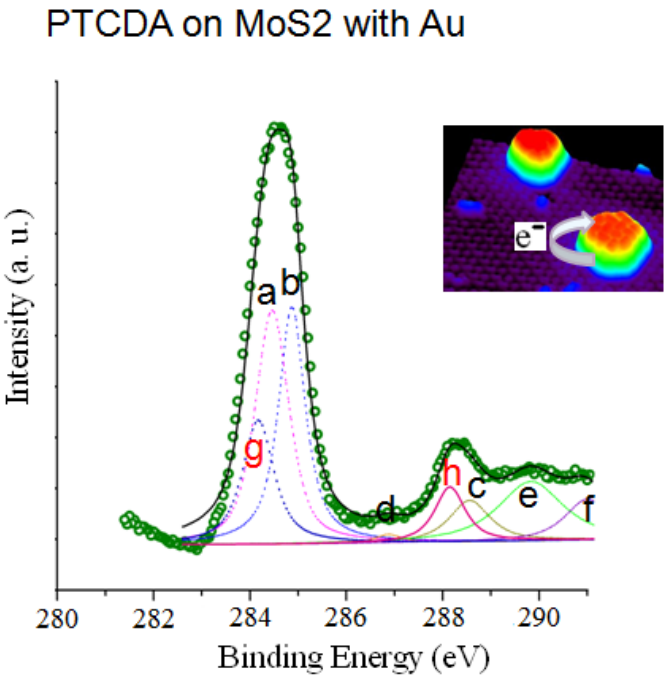

Fig. 6.6 (a) Fitting of C 1s core level spectrum for pure PTCDA monolayer into 6 components with an inset showing the chemical structure of PTCDA. (b) Fitting of C 1s spectrum for PTCDA with 0.2 Å Au deposited. The inset shows the electron transfer from Au NP to the PTCDA top layer.

6.4 Conclusion

In conclusion, we have fabricated size-tunable Au NPs on mono-layer PTCDA covered MoS_2 and investigated the morphology evolution as a function of Au deposition using STM. The PTCDA molecules acting as surfactant can help to form uniform and dispersed Au NPs. At initial deposition, ultra-small Au NPs with lateral size of < 3 nm and height ~1 nm can be synthesized. XPS results show that these Au NPs have different chemical properties than that of bulk Au and may have potential applications as the catalyst for oxidation of CO and NO, and CO_2 hydrogenation. Moreover, the Au NPs prepared in our way may facilitate fundamental studies and applications in connection with other molecular, inorganic and biological nano-material components.

References

[1] B. Hammer and J. K. Norskov, Nature **376**, 238 (1995).

[2] M. Haruta, T. Kobayashi, H. Sano, and N. Yamada, Chem. Lett. **2**, 405 (1987).

[3] M. Schubert, S. Hackenberg, A. van Veen, M. Muhler, V. Plzak, and R. Behm, J. Catal. **197**, 113 (2001).

[4] H. Boyen, G. Kastle, F. Weigl, B. Koslowski, C. Dietrich, P. Ziemann, J. Spatz, S. Riethmuller, C. Hartmann, and M. Moller, Science **297**, 1533 (2002).

[5] M. Chen and D. Goodman, Acc. Chem. Res. **39**, 739 (2006).

[6] J. Wang and B. Hammer, Topics in Catalysis **44**, 49 (2007).

[7] A. Herzing, C. Kiely, A. Carley, P. Landon, and G. Hutchings, Science **321**, 1331 (2008).

[8] A. Ueda, T. Oshima, and M. Haruta, App. Catal. B, Environmental **12**, 81 (1997).

[9] G. C. Bond, C. Louis, and D. T. Thompson edited, Catalysis by Gold; Vol. 6, edited by (Imperial College Press, London, 2006).

[10] J. Turkevitch, P. C. Stevenson, and J. Hillier, Discuss. Faraday Soc. **11**, 55-75 (1951).

[11] T. Yonezawa, T. Kunitake, Colloids Surf. A: Physicochem. Eng. Asp. **149**, 193 (1999).

[12] M. C. Daniel and D. Astruc, Chem. Rev. **104**, 293 (2004).

[13] M. Brust and C. Kiely, Colloids Surf. A: Physicochem. Eng. Asp. **202**, 175 (2002).

[14] S. Kushvaha, Z. Yan, W. Xiao, M. Xu, Q. Xue, and X. Wang, Nanotechnology **18**, 145501 (2007).

[15] X. Wang, S. Kushvaha, Z. Yan, and W. Xiao, App. Phys. Lett. **88**, 233105 (2006).

[16] H. Hövel and I. Barke, Prog. Surf. Sci. **81**, 53 (2006).

[17] C. Maurel, F. Ajustron, R. Pechou, G. Seine, and R. Coratger, Surf. Sci. **600**, 442 (2006).

[18] L. Kilian, A. Hauschild, R. Temirov, S. Soubatch, A. Scholl, A. Bendounan, F. Reinert, T. L. Lee, F. S. Tautz, M. Sokolowski, and E. Umbach, Phys. Rev. Lett. **100**, 136103 (2008).

[19] S. Henze, O. Bauer, T. Lee, M. Sokolowski, and F. Tautz, Surf. Sci. **601**, 1566 (2007).

[20] P. Lauffer, K. V. Emtsev, R. Graupner, T. Seyller, and L. Ley, Physica Status Solidi B **245**, 2064 (2008).

[21] N. Nicoara, E. Román, J. Gómez-Rodríguez, J. Martín-Gago, and J. Méndez, Organic Electronics **7**, 287 (2006).

[22] Y. Hirose, A. Kahn, V. Aristov, P. Soukiassian, V. Bulovic, and S. R. Forrest, Phys. Rev. B **54**, 13748 (1996).

[23] T. Wagner, H. Karacuban, A. Bannani, C. Bobisch, and R. Möller, J. Phys.: Conference Series **100**, 052068 (2008)

[24] Y. Hirose, A. Kahn, V. Aristov, P. Soukiassian, V. Bulovic, and S. R. Forrest, Phys. Rev. B **54**, 13748 (1996).

[25] J. B. Gustafsson, H. M. Zhang, E. Moons, and L. S. O. Johansson, Phys. Rev. B

75, 155413 (2007).

[26] A. Schöll, Z. Zou, M. Jung, T. Schmidt, R. Fink, and E. Umbach, J. Chem. Phys. **121**, 10260 (2004).

[27] Q. Chen, T. Rada, T. Bitzer, and N. Richardson, Surf. Sci. **547**, 385 (2003).

[28] P. J. Unwin, D. Onoufriou, J. J. Cox, C. P. A. Mulcahy, and T. S. Jones, SUrf. Sci. **482-485**, 1210 (2001).

[29] T. Soubiron, V. Vaurette, J. P. Nys, B. Grandidier, X. Wallart, and S. Stiévenard, SUrf. Sci. **581**, 178 (2005).

[30] F. S. Tautz, Prog. Surf. Sci. **82**, 479 (2007).

Chapter 7 Conclusions

Motivated by the unique electronic properties of Bi and its fascinating potential in many applications, this Ph. D project mainly addresses the investigation of self-assembled Bi nanostructures on inert substrates (MoS_2 and HOPG) and a transition metal substrate: Ru(0001). Prompted from the template growth of Bi NWs using PTCDA, I also illustrate an UHV-method for fabricating size tunable ultra-fine Au NPs on MoS_2 using PTCDA as a surfactant. This chapter will give conclusions and outlooks on these experiments.

When Bi is deposited on MoS_2(0001), two kinds of nanostructures, namely nanobelts and thin film, were observed with STM, SEM and LEED. Straight Bi nanobelts in (110) orientation can form at small deposition amount and low flux. Multi-layer branched Bi(110) nanostructures form at larger deposition amount and high flux. SEM images and LEED patterns reveal that the growth directions of Bi nanobelts deviate by ~ 13 ° from the $\langle 11\bar{2}0 \rangle$ axes of the substrate. When the thickness of Bi nanobelts exceeds the critical thickness of 4 BL (8 ML) of Bi(110), Bi(111) islands form at the top layers. With further increase deposition, a well ordered Bi(111) form. This critical thickness value indicates that the bonding of both types of Bi structures with MoS_2(0001) is rather weak. The results extend the understanding of self-assembly behavior of Bi on inert substrates and help to improve the synthesis method to get the desirable nanostructures. Also, branched linear nanostructures can provide us with building blocks for making more sophisticated devices and systems.

Additionally, our STS experiment illustrates the thickness dependent LDOS of Bi(110) layers at different thickness. A structural transition induced electronic structure change, i.e., from a semiconducting surface at 2- and 4-ML of Bi(110) to a metallic surface at thickness larger than 6 ML, is observed. This result extends the understanding of electronic structures of Bi(110) thin-film and may show interesting application potential of Bi in electronic nanodevices. Our experiments also show great potential of self-assembly in the fabrication of nano-components.

To better understand the growth kinetics of near free-standing nanostructures on inert substrate, I investigated the effect of PTCDA template layer on the growth of ultra-thin and large-LWR Bi NWs on MoS_2 using STM. Aligned single-layer Bi NWs firstly form due to the top passivation and guide effect of the molecules. These ultra thin NWs then develop into thicker and much longer NWs when more Bi was deposited. Due to the side wall passivation by PTCDA, the NWs grow in length extensively but little in width, leading to the formation of large-LWR NWs. Our results show the lateral growth of the width of Bi NWs is dramatically suppressed by the PTCDA layer which can also be considered as a surfactant layer. Moreover, this result may be very useful for revealing the nature of bonding between functional molecules and metal which is critical to the device performance in molecular and organic electronic applications.

To understand the effect of substrate in Bi NW self-assembly, the growth of Bi on Ru(0001) was investigated using LEED and STM. Three structural phases, i.e. $2 \times \sqrt{3}$, $\sqrt{7} \times \sqrt{7}$ and Bi(110), were obtained consecutively by adding the Bi deposition

amount. By decomposing the LEED pattern and calculating the lattice relations of the superstructure with respect to Ru, the real space lattice period and orientations of each structural phase are determined. STM images reveal the real space atomic structures on each phase (Bi(110) atomic structure not shown) and are in good agreement with the LEED pattern. Annealing experiment also proves that the phase transition from ***Phase I*** to ***Phase II*** is governed by the coverage of Bi atoms. The $\sqrt{7} \times \sqrt{7}$ surface is a more compact structure on Ru(0001) than $2 \times \sqrt{3}$ surface. The growth behavior of Bi(110) structures on saturated $\sqrt{7} \times \sqrt{7}$ surface is similar with that on inert substrate (HOPG and MoS_2) except the fixed orientation of Bi(110) lattice on the $\sqrt{7}$ lattice, indicating the stronger bonding between Bi(110) and $\sqrt{7}$ surface than that on MoS_2 and HOPG. Our experiment extends the understanding of nucleation and thin film growth of Bi on Ru(0001). The stable superlattice surface ($2 \times \sqrt{3}$ and $\sqrt{7} \times \sqrt{7}$) can act as new type of substrate for growth of inorganic and organic nanostructures. The electronic structures of each phase may exhibit interesting features which do not exist on either Bi or Ru.

Motivated by the experiment of template growth of Bi NWs, I used PTCDA as a surfactant to fabricated size-tunable Au NPs on MoS_2. PTCDA molecules can help to form uniform and dispersed Au NPs before the surface is saturated with NPs. At initial deposition, ultra-small Au NPs with lateral size < 3 nm and height ~1 nm can be synthesized. By controlling the deposition amount of Au, the size of Au NPs can be tuned. XPS results show that these Au NPs have different chemical properties than that of bulk Au, which may be important for the potential applications as the catalyst

for oxidation of CO and NO, and CO_2 hydrogenation. Moreover, the Au NPs may motivate fundamental studies and applications in connection with other molecular, inorganic and biological nano-material components.

All the above results provide examples to show the important roles of surface energetic, kinetic and mechanical properties played in the synthesis and the characteristics of nanostructures. By understanding the growth mechanics, certain topologic control of self-assembled nanostructures on inert substrates can be prompted. These mechanisms also can help to improve the fabrication of self-assembled Bi nanostructures on Si-based inert substrates, such as silicon nitrides and oxides, as they are the most reliable substrates for nano-devices and nano-circuits nowadays.